



THE HONG KONG
POLYTECHNIC UNIVERSITY

香港理工大學

Pao Yue-kong Library

包玉剛圖書館

Copyright Undertaking

This thesis is protected by copyright, with all rights reserved.

By reading and using the thesis, the reader understands and agrees to the following terms:

1. The reader will abide by the rules and legal ordinances governing copyright regarding the use of the thesis.
2. The reader will use the thesis for the purpose of research or private study only and not for distribution or further reproduction or any other purpose.
3. The reader agrees to indemnify and hold the University harmless from and against any loss, damage, cost, liability or expenses arising from copyright infringement or unauthorized usage.

IMPORTANT

If you have reasons to believe that any materials in this thesis are deemed not suitable to be distributed in this form, or a copyright owner having difficulty with the material being included in our database, please contact lbsys@polyu.edu.hk providing details. The Library will look into your claim and consider taking remedial action upon receipt of the written requests.

**DESIGN AND REALIZATION OF
STRUCTURAL MATERIALS WITH
HIGH STRENGTH AND HIGH DUCTILITY**

LEUNG WING YAN

Ph.D

The Hong Kong Polytechnic University

2017

THE HONG KONG POLYTECHNIC UNIVERSITY
DEPARTMENT OF MECHANICAL ENGINEERING

DESIGN AND REALIZATION OF
STRUCTURAL MATERIALS WITH
HIGH STRENGTH AND HIGH DUCTILITY

LEUNG WING YAN

A thesis submitted in partial fulfilment of the requirements
for the degree of Doctor of Philosophy

October 2016

CERTIFICATE OF ORIGINALITY

I hereby declare that this thesis is my own work and that, to the best of my knowledge and belief, it reproduces no material previously published or written, nor material that has been accepted for the award of any other degree or diploma, except where due acknowledgement has been made in the text

LEUNG WING YAN

ABSTRACT

The SMAT has been widely studied through experimental approach in the past decades. After the process, the microstructure of metal can be scaled down to nano-scale mechanically by numerous balls striking to the metal. So, the strength of metal can be enhanced drastically. However, lots of parameters can affect the result in SMAT. Investigating the effects experimentally is not an effective approach. Through the understanding of the strengthening mechanism of SMAT, numerical computation can then facilitate the investigation.

A virtual SMAT chamber with numerous balls was designed and the number of ball impacts was counted in a given processing duration. The position of each ball at each time increment was checked to detect collision. If there was a ball-ball collision or ball-boundary collision, the velocity of ball would be updated. The impact positions and velocities of the balls in a predetermined processing duration were used for the simulation of SMAT.

Johnson-Cook (JC) model was widely used in the simulation of high-velocity-impact. However, the original JC model only considered the equivalent plastic strain, strain rate and homogenous temperature. As the microstructure of metal was continuously refined in SMAT, a new constitutive model was developed to include

the effect of grain and twin spacing refinements in SMAT. Both microstructure refinements were both influenced by the growth of dislocations, which was in turn determined by the equivalent plastic strain. By updating the equivalent plastic strain in each impact, the flow stress in SMAT was predicted by the micro and macro parameters.

Utilizing the information of impact positions and velocities of the balls in the virtual chamber and the new constitutive model, a simulation model was developed to predict the mechanical properties in SMAT. It was found that the original JC model would underestimate the stress in SMAT, while the stress predicted by the new constitutive model agreed well with the experimental results reported in the literature. In the new constitutive model, a varying yield stress was used as one of the input parameters. A 100-balls SMAT process lasting for 10 minutes was simulated. The simulated maximum tensile stress was 1.26 GPa while the measured tensile stress reported in the literature was 1.23 GPa, proving the effectiveness of the new constitutive model. Using the new computational model, different parameters can now be investigated first by simulation, which will provide valuable guidelines to the design of experiments.

PUBLICATIONS

Leung, W.Y., Shi, S.Q., Lu, J., Ruan, H.H., and Zhou, L.M. (September, 2016). A Constitutive Model on Flow Stress Prediction from the Contribution of Twin and Grain Refinement, Strain and Strain Rate during Surface Mechanical Attrition Treatment of Metals. *Journal of Chemical Engineering and Material Science*.

Leung, W.Y., Ruan, H.H., Lu, J., Shi, S.Q., and Zhou, L.M. The Computational Model of Surface Mechanical Attrition Treatment (SMAT). *Material and Design* (Submitted).

Leung, W.Y., Ruan, H.H., Lu, J., Shi, S.Q., and Zhou, L.M. (2015). Modeling on Flow Stress in Contribution of Twins and Grain Refinement. *Global Engineering & Applied Science Conference*. Tokyo, Japan: Higher Education Forum, (GEASC 1324). Available at

<http://geasc-conf.org/Upload/EditorFiles/201510/20151021145802472.pdf>

Leung, W.Y., Zhou, L.M., Shi, S.Q., and Lu, J. (2014). Investigation of Various Factors during Surface Attrition Mechanical Treatment (SMAT) by Simulation Approach. 3rd Conference on Nanomechanics and Nanocomposites (ICNN-3). Hong Kong, China. Available at <http://www.polymer.cn/ICNN-3/down/ICNN-3-Final%20Program.pdf/>

ACKNOWLEDGEMENTS

I would like to express my sincere gratitude to my supervisors, Prof. L.M. Zhou, Prof. S.Q. Shi and Dr. H.H. Ruan in the Department of Mechanical Engineering (ME) in the Hong Kong Polytechnic University (PolyU) and Prof. J. Lu in the Department of Mechanical and Biomedical Engineering (MBE) in the City University of Hong Kong (CityU) for their continuous support, guidance, patience, immense knowledge and encouragement throughout my research study. Without their support and guidance, I could not be able to complete this project with such a high degree of accomplishment.

I would like to give my great thanks to the laboratory technicians of ME and Industrial Center in PolyU for their assistance and advice.

I would like to acknowledge the financial support of the PolyU and a grant from Research Grants Council of Hong Kong (CityU7/CRF/08).

At last, I would like to thank once again to all who has given me advice, ideas and assistance in this project.

TABLE OF CONTENT

CERTIFICATE OF ORIGINALITY	II
ABSTRACT	III
PUBLICATIONS	V
ACKNOWLEDGEMENTS	VII
TABLE OF CONTENT	VIII
LIST OF FIGURES	XII
LIST OF TABLES	XVII
NOMENCLATURE.....	XVIII
CHAPTER 1 - INTRODUCTION	- 1 -
1.1 Background	- 1 -
1.2 Objectives.....	- 7 -
1.3 Engineering Significance	- 8 -
1.4 Scope of Work.....	- 9 -
1.5 Organization of this Report	- 10 -
CHAPTER 2 - LITERATURE REVIEW	- 13 -
2.1 Introduction	- 13 -
2.2 Nanocrystallization (NC) Process	- 14 -
2.2.1 Surface Mechanical Attrition Treatment	- 15 -
2.2.2 High Pressure Torsion (HPT).....	- 19 -
2.2.3 Equal Channel Angular Pressing (ECAP).....	- 21 -
2.2.4 Air Blast Shot Peening (ABSP).....	- 22 -

2.3	Experiments on Various Metals using SMAT.....	- 24 -
2.3.1	AISI 304 Stainless Steel	- 25 -
2.3.2	Copper	- 29 -
2.3.3	Titanium	- 30 -
2.3.4	Other Metals	- 31 -
2.4	Nanocrystallization Mechanism	- 33 -
2.4.1	Grain Refinement Mechanism of Metal with Low Stacking Fault Energy ..	- 34 -
2.4.2	Grain Refinement Mechanism of High Stacking Fault Energy Metal	- 37 -
2.4.3	Martensite Transformation	- 38 -
2.5	Numerical Modeling.....	- 39 -
2.5.1	Residual Stress Modeling	- 40 -
2.5.2	Grain Size Evolution	- 44 -
2.5.3	Twins Nucleation	- 47 -
2.5.4	Dislocation Density	- 49 -
2.6	Computational Simulation.....	- 51 -
2.6.1	Simulation of Nanostructure Production	- 51 -
2.6.2	Simulation of Microstructure	- 54 -
2.7	Summary	- 56 -
 CHAPTER 3 - THE COMPUTATIONAL MODEL OF SMAT.....		- 57 -
3.1	Introduction	- 57 -
3.2	Assumptions	- 57 -
3.3	Modeling of SMAT	- 59 -
3.4	Demonstration of SMAT.....	- 65 -
3.5	Effects of Processing Parameters	- 68 -
3.5.1	Prediction of Number of Impacts with Different Number of Balls (n) and Processing Durations.....	- 69 -

3.5.2	Effects of Maximum Ball Velocity, Height and Radius of Chamber	- 72 -
3.6	Summary	- 76 -
 CHAPTER 4 - THEORY ON CONSTITUTIVE MODELING		- 78 -
4.1	Introduction	- 78 -
4.2	Development of Constitutive Equation	- 79 -
4.2.1	Assumptions for the Constitutive Equation.....	- 79 -
4.2.2	Modification of Johnson-Cook Model	- 82 -
4.2.3	Modified Johnson-Cook (JC) Model.....	- 88 -
4.2.4	Determination of Grain Size and Twin Spacing.....	- 90 -
4.3	Validations and Stress Prediction by New Constitutive Equations	- 93 -
4.3.1	Validation of the New Constitutive Equation.....	- 94 -
4.3.2	Stress Prediction	- 94 -
4.4	Stress Integration of Metal Plasticity	- 97 -
4.4.1	Basic Components of Elastoplastic Model.....	- 98 -
4.4.2	Elastic Predictor	- 99 -
4.4.3	Plastic Predictor.....	- 100 -
4.5	Summary	- 102 -
 CHAPTER 5 - FINITE ELEMENT ANALYSIS ON SMAT		- 104 -
5.1	Introduction	- 104 -
5.2	Simulation of Mechanical Properties after SMAT	- 104 -
5.2.1	A Single Ball Normal Impact at Different Velocities	- 105 -
5.2.2	A Single Ball Impact at Different Angles	- 111 -
5.2.3	Simulation of Multiple Impacts.....	- 117 -
5.3	Summary	- 126 -

CHAPTER 6 - SIMULATION OF SMAT BY CONSTITUTIVE MODEL..	- 128 -
6.1 Introduction	- 128 -
6.2 Single-Element Test	- 129 -
6.3 Single-Ball Impact Test.....	- 130 -
6.4 Multiple Impacts in SMAT Simulated by Constitutive Equation	- 134 -
6.4.1 Case 1: 3-Min Process	- 135 -
6.4.2 Case 2: 10-min Process	- 147 -
6.4.3 Further Discussion of Cases 1 and 2	- 160 -
6.5 Summary	- 162 -
CHAPTER 7 - CONCLUSIONS AND RECOMMENDATIONS	- 165 -
7.1 Conclusions	- 165 -
7.2 Recommendations and Further Work.....	- 168 -
7.2.1 Development of Large Scale Production.....	- 168 -
7.2.2 Modeling of Stacking Fault Energy and Martensite Transformation	- 169 -
7.2.3 Development of General Equation on Various Impacting Factors.....	- 170 -
7.2.4 Application to other Several Plastic Deformation Process.....	- 171 -
BIBLIOGRAPHY	- 172 -

LIST OF FIGURES

FIGURE 1.1 TRUE STRESS AND TRUE STRAIN CURVE OF NANOCRYSTALLINE COPPER (LU, ET AL., 2004).....	2 -
FIGURE 1.2 SCHEMATIC CONFIGURATION OF SURFACE MECHANICAL ATTRITION TREATMENT SYSTEM.....	4 -
FIGURE 1.3 MICROSTRUCTURE OF STAINLESS STEEL 304 AFTER SMAT (CHEN, ET AL., 2011)	5 -
FIGURE 2.1 PLASTIC DEFORMATION DIRECTION OF SAMPLE SURFACE AFTER IMPACT IN SMAT (LU & LU, 2004).....	16 -
FIGURE 2.2 SURFACE EVOLUTION DURING SMAT (ARIFVIANTO, ET AL., 2012)	17 -
FIGURE 2.3 MICROSTRUCTURES, STRAIN, AND STRAIN RATE DISTRIBUTION ALONG THE DEPTH FROM THE SAMPLE SURFACE IN SMAT (LU & LU, 2004).....	19 -
FIGURE 2.4 REPRESENTATION OF HPT (VALIEV, ET AL., 2006)	20 -
FIGURE 2.5 ILLUSTRATION OF EQUAL CHANNEL ANGULAR PRESSING (VALIEV, ET AL., 2006)	22 -
FIGURE 2.6 SET-UP OF AIR BLAST SHOT PEENING AT: (A) THE WHOLE VIEW; (B) THE CROSS-SECTIONAL VIEW (UMEMOTA, ET AL., 2003)	24 -
FIGURE 2.7 TEM IMAGE AND GRAIN SIZE DISTRIBUTION ON THE TOP SURFACE ANNEALED AT 1080 °C AND SMAT FOR 15-MIN PROCESS (ZHANG, ET AL., 2003) ...	26 -
FIGURE 2.8 ENGINEERING STRESS-STRAIN CURVES OF AISI 304 SS (CHEN, ET AL., 2011)	28 -
FIGURE 2.9 SCHEMATIC DIAGRAM OF WARM CO-ROLLING PROCESS (LU, ET AL., 2011) ...	29 -
FIGURE 2.10 ILLUSTRATION OF THE GRAIN REFINEMENT MECHANISM OF LOW SFE METAL (TAO, ET AL., 2003)	36 -
FIGURE 2.11 SCHEMATIC DIAGRAM OF THE GRAIN REFINEMENT MECHANISM OF PURE IRON (TAO, ET AL., 2002; AZADMANJIRI, ET AL., 2015).....	38 -
FIGURE 2.12 ILLUSTRATION OF THE GRAIN REFINEMENT WITH MARTENSITE TRANSFORMATION (SHENG, 2011).....	39 -
FIGURE 2.13 HALL-PETCH RELATIONSHIP BETWEEN THE YIELD STRESS AND THE GRAIN	

SIZE (HALL, 1951; PETCH, 1953).....	- 45 -
FIGURE 3.1 CONFIGURATION IN THE SIMULATION MODEL	- 60 -
FIGURE 3.2 RELATIONSHIP BETWEEN THE POWER SETTING OF SMAT, THE BALL VELOCITY, AND THE VIBRATION AMPLITUDE OF HORN (CHAN, ET AL., 2010; TSAI, ET AL., 2015).....	- 63 -
FIGURE 3.3 (A) EXPERIMENTAL SETUP OF IMAGE CAPTURE OF SMAT; (B) ACRYLIC TRANSPARENT CHAMBER.....	- 66 -
FIGURE 3.4 THREE CONSECUTIVE IMAGES AT (A) 0.011s, (B) 0.012s, (C) 0.013s FOR 50 BALLS.....	- 67 -
FIGURE 3.5 COMPARISON OF SIMULATION RESULTS OF NUMBER OF BALL IMPACTS AND DURATION OF DIFFERENT NUMBERS OF BALLS	- 71 -
FIGURE 3.6 RELATIONSHIP BETWEEN THE NUMBER OF BALL IMPACTS PER SECOND AND THE NUMBER OF BALLS IN THE CHAMBER	- 71 -
FIGURE 3.7 RELATIONSHIP BETWEEN THE NUMBER OF BALL IMPACTS PER SECOND AND THE MAXIMUM BALL VELOCITY FOR 100 BALLS	- 72 -
FIGURE 3.8 INVERSELY RELATIONSHIP BETWEEN THE NUMBER OF BALLS AND THE MAXIMUM BALL VELOCITY	- 74 -
FIGURE 3.9 RELATIONSHIP BETWEEN THE HEIGHT OF CHAMBER AND THE NUMBER OF BALLS.....	- 75 -
FIGURE 4.1 ILLUSTRATION OF GRAIN AND TWIN BOUNDARIES (ZHU, ET AL., 2011)..	- 85 -
FIGURE 4.2 DETERMINATION OF RELATIONSHIP BETWEEN GRAIN SIZE AND EQUIVALENT PLASTIC STRAIN.....	- 92 -
FIGURE 4.3 COMPARISON OF FLOW STRESS DOMINANT BY GRAIN REFINEMENT AND/OR TWIN FORMATION	- 96 -
FIGURE 4.4 RELATIONSHIP BETWEEN FLOW STRESS DUE TO GRAIN REFINEMENT AND STRAIN AT DIFFERENT STRAIN RATES	- 96 -
FIGURE 4.5 RELATIONSHIP BETWEEN FLOW STRESS DUE TO TWIN SPACING AND STRAIN AT DIFFERENT STRAIN RATES	- 97 -
FIGURE 5.1 COMPARISON OF STRESSES ALONG THE DEPTH OF PLATE AT CENTER AT DIFFERENT BALL VELOCITIES.....	- 107 -
FIGURE 5.2 CONTOUR PLOT OF STRESS AT DIFFERENT BALL VELOCITIES AT (A) 4 M/S; (B) 5 M/S; (C) 6 M/S; (D) 7 M/S; (E) 8 M/S; (F) 9 M/S; (G) 10 M/S.....	- 108 -
FIGURE 5.3 STRESS ON HORIZONTAL DISTANCE ACROSS THE CENTER OF IMPACT IN Z-	

DIRECTION.....	- 109 -
FIGURE 5.4 COMPARISON OF EQUIVALENT PLASTIC STRAIN RATE AT DIFFERENT BALL VELOCITIES AT THE CENTER NODE	- 110 -
FIGURE 5.5 COMPARISON OF STRESS-STRAIN RELATIONSHIP AT DIFFERENT BALL VELOCITIES AT CENTER NODE	- 111 -
FIGURE 5.6 DEFINITION OF IMPACT ANGLE	- 113 -
FIGURE 5.7 COMPARISON OF EQUIVALENT PLASTIC STRAIN RATE OF ANGULAR AND NORMAL IMPACT AT THE CENTER NODE.....	- 114 -
FIGURE 5.8 COMPARISON OF STRESS-STRAIN RELATIONSHIP OF NORMAL AND ANGULAR IMPACT AT 5 M/S	- 114 -
FIGURE 5.9 COMPARISON OF STRESS-STRAIN RELATIONSHIP OF NORMAL AND ANGULAR IMPACT	- 115 -
FIGURE 5.10 COMPARISON OF STRESS-STRAIN RELATIONSHIP OF NORMAL AND ANGULAR IMPACT AT 7 M/S	- 115 -
FIGURE 5.11 COMPARISON OF STRESS-STRAIN RELATIONSHIP OF NORMAL AND ANGULAR IMPACT AT 8 M/S	- 116 -
FIGURE 5.12 COMPARISON OF STRESS-STRAIN RELATIONSHIP OF NORMAL AND ANGULAR IMPACT AT 9 M/S	- 116 -
FIGURE 5.13 THE CENTER POINTS OF BALLS' IMPACT POSITIONS IN A CIRCULAR AREA WITH DIAMETER OF 0.2 MM	- 118 -
FIGURE 5.14 FINITE ELEMENT MODEL OF 27 BALLS IMPACTING TO THE TARGET PLATE....	- 119 -
FIGURE 5.15 (A) CONTOUR DISTRIBUTION OF FINAL RESIDUAL STRESS AND (B) RESIDUAL STRESS ALONG THE DEPTH OF PLATE AT THE ORIGIN AFTER 27 BALL IMPACTS	- 123 -
FIGURE 5.16 AVERAGING SIMULATED YIELD STRESS ON THE SPECIFIC AREA AT VARIOUS IMPACT VELOCITIES, POSITIONS, AND ANGLES	- 125 -
FIGURE 5.17 AVERAGING SIMULATED YIELD STRESS WITH ALL THE BALLS' VELOCITY AT 10 M/S	- 125 -
FIGURE 6.1 CONFIGURATION OF A SINGLE-ELEMENT TEST	- 129 -
FIGURE 6.2 COMPARISON OF STRESS-STRAIN CURVE IN A SINGLE-ELEMENT TEST.-	- 130 -
FIGURE 6.3 CONTOUR PLOT OF VON MISES STRESS (VUMAT).....	- 131 -
FIGURE 6.4 COMPARISON OF STRESS-STRAIN RESULTS SIMULATED WITH THE	

EMBEDDED AND VUMAT JC MODEL.....	- 132 -
FIGURE 6.5 COMPARISON OF EQUIVALENT PLASTIC STRAIN SIMULATED WITH THE EMBEDDED AND VUMAT JC MODEL.....	- 133 -
FIGURE 6.6 COMPARISON OF STRESS SIMULATED WITH AN EMBEDDED AND VUMAT JC MODEL	- 133 -
FIGURE 6.7 SETTING OF SIMULATION MODEL.....	- 135 -
FIGURE 6.8 VON MISES STRESS ON THE SELECTED AREA FOR 3-MIN PROCESS.....	- 137 -
FIGURE 6.9 EQUIVALENT PLASTIC STRAIN ALONG THE THICKNESS OF PLATE	- 137 -
FIGURE 6.10 ESTIMATED YIELD STRESS ($A + B\epsilon^N$) CALCULATED BY EQUIVALENT PLASTIC STRAIN FOR 3-MIN PROCESS	- 138 -
FIGURE 6.11 ESTIMATED TENSILE STRESS-STRAIN CURVE BY A AT 723 MPa FOR 3-MIN PROCESS	- 139 -
FIGURE 6.12 EQUIVALENT PLASTIC STRAIN RESULT FOR 3-MIN PROCESS.....	- 140 -
FIGURE 6.13 CONTOUR PLOT OF EQUIVALENT PLASTIC STRAIN FOR 3-MIN PROCESS.....	- 141 -
FIGURE 6.14 AVERAGE OF FLOW STRESS FOR 3-MIN SMAT	- 142 -
FIGURE 6.15 AVERAGE FLOW STRESS ALONG THE DEPTH OF PLATE FOR 3-MIN PROCESS	- 142 -
FIGURE 6.16 AVERAGE GRAIN SIZE FOR 3-MIN PROCESS	- 144 -
FIGURE 6.17 CONTOUR PLOT OF GRAIN SIZE FOR 3-MIN PROCESS	- 145 -
FIGURE 6.18 AVERAGE TWIN SPACING FOR 3-MIN PROCESS.....	- 146 -
FIGURE 6.19 CONTOUR PLOT OF TWIN SPACING FOR 3-MIN PROCESS	- 147 -
FIGURE 6.20 CONTOUR PLOT OF VON MISES STRESS RESULT ON ELEMENT SET OF SELECTED AREA FOR 10-MIN PROCESS	- 150 -
FIGURE 6.21 ENGINEERING STRESS-STRAIN CURVE AS-RECEIVED 304 SS AND FOR 10- MIN PROCESS (LU, ET AL., 2011).....	- 151 -
FIGURE 6.22 COMPARISON OF SIMULATED ($A + B\epsilon^N$) AND EXPERIMENTAL YIELD STRESS RESULTS FOR 10-MIN PROCESS.....	- 151 -
FIGURE 6.23 ESTIMATED TENSILE STRESS-STRAIN CURVE BY A AT 781 MPa FOR 10-MIN PROCESS	- 152 -
FIGURE 6.24 EQUIVALENT PLASTIC STRAIN (EQPLS) PLOT IN EACH IMPACT FOR 10- MIN PROCESS	- 154 -
FIGURE 6.25 CONTOUR PLOT ON THE EQUIVALENT PLASTIC STRAIN IN LAST STEP FOR	

10-MIN PROCESS.....	- 154 -
FIGURE 6.26 AVERAGE FLOW STRESS IN EACH STEP FOR 10-MIN PROCESS	- 155 -
FIGURE 6.27 AVERAGE FLOW STRESS ALONG THE DEPTH OF PLATE FOR 10-MIN PROCESS	- 156 -
FIGURE 6.28 GRAIN SIZE REFINEMENT AT EACH IMPACT FOR 10-MIN PROCESS	- 157 -
FIGURE 6.29 CONTOUR PLOT OF GRAIN SIZE AFTER 27 BALL IMPACTS FOR 10-MIN PROCESS	- 158 -
FIGURE 6.30 TWIN SPACING REFINEMENT IN EACH IMPACT FOR 10-MIN PROCESS..	- 159 -
FIGURE 6.31 CONTOUR PLOT OF TWIN SPACING IN LAST STEP FOR 10-MIN PROCESS	- 160 -
FIGURE 6.32 COMPARISON OF EQUIVALENT PLASTIC STRAIN IN CASES 1 AND 2 FOR 10-MIN PROCESS	- 161 -

LIST OF TABLES

TABLE 2.1 SETTINGS OF SMAT FOR AISI 304 SS WITH DIFFERENT STRAIN RATES (CHEN, ET AL., 2011).....	- 27 -
TABLE 3.1 SUMMARY OF VARIOUS SETS OF MATLAB SIMULATION	- 65 -
TABLE 3.2 EXPERIMENTAL ESTIMATION AND SIMULATION PREDICTION OF THE NUMBER OF BALL IMPACTS IN 1s FOR 50 BALLS, 100 BALLS AND 200 BALLS.....	- 68 -
TABLE 3.3 RELATIONSHIP BETWEEN THE RADIUS OF CHAMBER (R) AND THE NUMBER OF BALLS (N)	- 76 -
TABLE 4.1. PARAMETERS USED IN THE NEW CONSTITUTIVE EQUATION (CHEN, ET AL., 2011; ZHU, ET AL., 2011)	- 90 -
TABLE 5.1 VELOCITIES SET IN THE ANGULAR IMPACT SIMULATION	- 112 -
TABLE 5.2 PARAMETERS OF AISI 304SS (PLATE) FOR SIMULATION	- 120 -
TABLE 6.1 IMPACT POSITIONS AND VELOCITIES OF EACH BALL FOR 3-MIN PROCESS	- 135 -
TABLE 6.2 IMPACT POSITIONS AND VELOCITIES OF EACH BALL FOR 10-MIN PROCESS	- 148 -

NOMENCLATURE

A	material constant / static yield stress in Johnson-Cook (JC) model (MPa)
B	material constant in Johnson-Cook model (MPa)
C	material constant in Johnson-Cook model
m	material constant in Johnson-Cook model
n	material constant in Johnson-Cook model
σ_f	flow stress (MPa)
$\bar{\varepsilon}^p$	equivalent plastic strain
$\dot{\varepsilon}^*$	the dimensionless plastic strain rate in JC-model
$\dot{\varepsilon}_0$	reference plastic strain rate in JC-model
$\dot{\varepsilon}$	equivalent plastic strain rate (/s)
T^{*m}	homologous temperature in JC-model
T_0	reference temperature in JC-model (°C)
T_m	reference melting temperature in JC-model
σ_y	yield stress (MPa)
d_G	grain size (μm)
σ_0	constant in Hall-Petch equation (MPa)
k	constant in Hall-Petch equation
d_∞	material constant (Kim & Kim, 2010) (μm)
ε_c	material constant (Kim & Kim, 2010)
d_0	initial grain size (μm)
r_c	critical twin nucleus thickness (nm)

σ	equivalent stress (Equation 2.6) (MPa)
G	shear modulus (Pa) (GPa)
γ_{TB}	twin boundary energy
ρ_{TB}	density of inclined dislocations in Twin Boundary Pile-up Zone (TBDPZ) / twin boundary
k^{TB}	ratio of thickness of TBDPZ and twin boundary
$\tilde{\eta}^{TB}$	effective local strain gradient in TBDPZ
σ_f	flow stress (MPa)
ρ	dislocation density
α	constant of ordering unit, depending on the strength of the dislocation
b	Burger vector
S	ball position in the chamber
V	ball velocity in the chamber (m/s)
t	current time (s)
Δt	time step (s)
V_{\parallel}	tangential velocity component of the ball at the point of impact (m/s)
V_{\perp}	normal velocity component of the ball at the point of impact (m/s)
C_R	coefficient of restitution (COR)
A_h	amplitude of the vibration horn
ω	angular frequency of the vibration horn set at 20 kHz
φ	phase angle
g	gravity at 9.81 m/s ²
N_{τ}	number of impacts per second
n	number of balls

v	maximum ball velocity set in the computational model (m/s)
τ	processing duration at SMAT in the computational model (s)
N	total number of impacts
h	height of chamber in SMAT (mm)
R	radius of chamber (mm)
ρ_I	dislocation density inside a grain
ρ_{GB}	dislocation density at grain boundary
d_{TBDPZ}	Thickness of TBDPZ (nm)
d_{TB}	twin spacing (TB) (nm)
ϕ^{TB}	geometric factor
$\tilde{\eta}^{TB}$	effective local strain gradient in the TBDPZ
η^{TB}	independent parameters of twin spacing
ϕ_p	geometric factor
η_1	independent parameters of twin spacing
η_0	independent parameters of twin spacing
N_0	constant, maximum number of inclined dislocations in a grain
η'_p	number of initial twinning partials in the TBDPZ
n_F^{TB}	number of inclined dislocations around the twin boundaries
χ	twin density in the grains
n^{GB}	number of dislocations around the grain boundaries
λ^{GB}	the average length of dislocation loops in GBDPZ
V_{cell}	the volume of the unit cell
ϕ_3	geometry constant
$\sigma_y(d_{TB})$	yield stress determined by grain size and twin spacing (MPa)

$\sigma_y(d_G)$	yield stress determined by grain size only (MPa)
$\boldsymbol{\varepsilon}$	strain tensor
$(\cdot)^e$	notation for elastic component
$(\cdot)^p$	notation for plastic component
$\boldsymbol{\varepsilon}^e$	elastic strain
$(\cdot)^*$	notation of trial value
$\boldsymbol{\varepsilon}_{n+1}^{e*}$	elastic trial strain
$\boldsymbol{\varepsilon}_{n+1}^{p*}$	trial accumulated plastic strain
$\Delta\boldsymbol{\varepsilon}$	strain increment corresponding to a typical time increment $[t_n, t_{n+1}]$
\boldsymbol{s}_{n+1}^*	corresponding trial stress
$\boldsymbol{\varepsilon}_{d(t+1)}^{e*}$	trial elastic deviatoric strain at next time step
\boldsymbol{s}	deviatoric stress
$p_{(t+1)}^*$	trial hydrostatic stress at next time step
$\boldsymbol{\varepsilon}_v$	volumetric strain
K	Bulk modulus
$\sigma(\cdot)$	calculated trial stress
$q(\boldsymbol{s})$	von Mises yield criterion
$\Phi(\boldsymbol{\sigma}, \sigma_f)$	yield function
V_y	impact Velocity at y-direction (m/s)
V_x	impact Velocity at x-direction (m/s)
θ	incident angle at the point of impact

CHAPTER 1 - INTRODUCTION

1.1 Background

Nanotechnology has now become an increasingly important branch of materials processing. Scientists have continually researching on enhancement methods for the strength, ductility and hardness of various materials at the nano-scale. Numerous manufacturing methods for preparing nanocrystalline materials, such as electrodeposition (Ebrahimi, et al., 1999; Shen, et al., 2008), powder technology (Pickens, 1981; Zhang, et al., 2011b), and the development of carbon nanotubes (Sun, et al., 2007) etc., have been developed for mechanical properties enhancement. However, these methods are mostly applicable for non-metals and some may even change the chemical composition of the material. These problems inhibit the production of metals using nanostructures to improve the mechanical properties.

In general, the mechanical hardening method is appropriate for improving the mechanical properties of metals without affecting their compositions, which can be applied in aeronautics, automotive or marine industries for advanced usages. The strength of coarse grained metals is mainly achieved by the resistance to plastic

deformation, where the propagation of lattice dislocations breaks large grains interior to small grains. A larger force is required to further split up the smaller grains, until metal fracture occurs. When the metal is initially at the nano-grained scale (grain size smaller than 100 nm), the strength of the metal can be greatly improved. However, further reduction of grain size may scarify the ductility (Lu, et al., 2004). Figure 1.1 compares the strengths of coarse-grained and nano-twin copper after Surface Mechanical Attrition Treatment (SMAT). The coarse-grained copper has a lowest value of yield true stress than nanocrystalline copper (nc Cu). Nanocrystalline copper with twins (nano-twin Cu) has the highest value of yield true stress and is more ductile than nanocrystalline copper. This proves that nanocrystallization can effectively increase the metal strength.

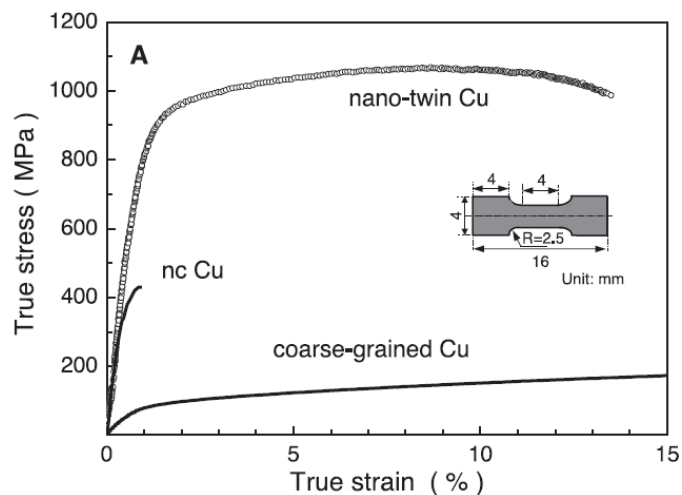


Figure 1.1 True stress and true strain curve of nanocrystalline copper (Lu, et al.,

2004)

Surface treatment is one of the nanocrystallization processes. It neither changes the chemical composition nor reshapes the dimensions of the metal after treatment. It only produces nanostructure on the material surface. Severe Plastic Deformation (SPD) is one of its significant and effective technologies for surface treatment and is a kind of mechanical method for producing nano-scaled surfaces. A high pressure, accompanied with large shear strain, is applied during the SPD process. Through this strain hardening process, the grains are refined superficially to become nanostructure. SMAT is one of the surface treatment methods for producing nano-grains on the metal surface.

Similar to shot peening, a number of steel or ceramics balls are positioned in a chamber with a vibration horn. As illustrated in Figure 1.2, the balls fly in random directions and hit the metal surface to achieve plastic deformation.

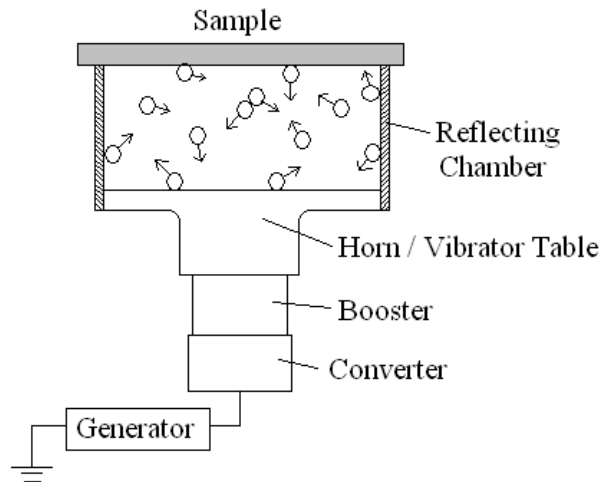


Figure 1.2 Schematic configuration of surface mechanical attrition treatment system

With the benefits of non-directional grain refinement, SMAT is superior to the other methods since the mechanical hardening comes in multi-directions. As shown in Figure 1.3, the stainless steel 304 metal surface becomes nanostructured after the SMAT, and the grain size of the stainless steel is now less than 100 nm, as the grain nano-scale and the aspect ratio is small. This implies that the metal can maintain isotropic properties better than other strain hardening methods in producing anisotropic material.

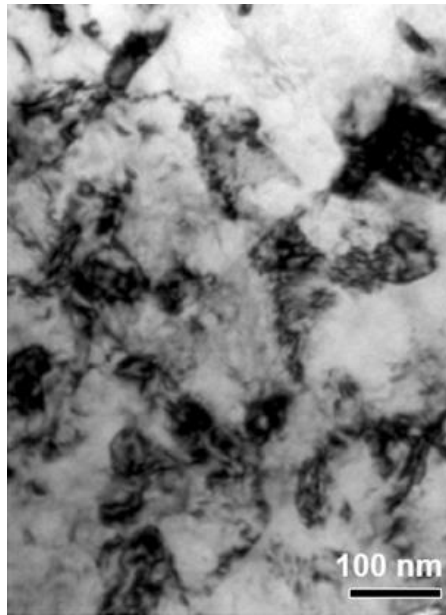


Figure 1.3 Microstructure of stainless steel 304 after SMAT (Chen, et al., 2011)

Extensive experimental studies have been conducted by researchers to investigate the subsurface nanostructures after SMAT in copper (Wang, et al., 2006), titanium (Zhu, et al., 2004; Zhang, et al., 2004), nickel (Li, et al., 2009), inconel 600 alloy (Tao, et al., 2003), stainless steel (Zhang, et al., 2003; Chan, et al., 2010; Arifvianto, et al., 2011; Chen, et al., 2011; Lu, et al., 2011), aluminium (Cheung, et al., 2011), steel (Prabhu, et al., 2012; Gatey, et al., 2013) and iron (Tao, et al., 2002) etc. The grain size was in a range from a few nanometers on the top surface to several micrometers at a 100 μm depth. The yield stresses of the treated samples were greatly increased due to the grain refinement, dislocation multiplication, twin-twin intersection, twin-induced grain boundary and/or martensitic transformation etc. The

evolution of the microstructure is affected by, but not limited to, a number of factors, such as frequency of the vibration horn, ball size, ball density, type of target and ball material, processing duration of SMAT etc.

Since there are many parameters affecting the metal behaviour after SMAT, conducting experiments may not cover every possible combination before SMAT. With the aid of computation simulation, the development of a simulation model can vary different parameters to predict the results after SMAT. With the work of many scientists, much experimental data for various metals treated by SMAT are presented in major or limited simulations (Zhang, et al., 2011a) conducted to predict the mechanical properties after SMAT. If the relationship between the processing duration and number of impacts in SMAT has not been determined in current development, that will be obstructing the development of simulation in predicting the behaviours of metal after SMAT because the processing duration cannot be quantified in the simulation of the mechanical properties. A model is to be developed to determine each ball impact location and velocity in all directions in order to count the number of impacts in a certain processing duration.

Besides, by observing the experimental results, the strength is affected by both the macrostructure and microstructure of the metal (i.e. ball size and grain refinement). Conventional material laws may not be appropriated to predict the mechanical properties. A new constitutive model is required with consideration of the microstructure and macrostructure together. With the known ball impact location and velocity, and governing law, the strength of the metal after SMAT can then be determined using finite element analysis. The impact motion of a ball on the metal surface can be simulated in steps at the required location and velocity. After a series of impacts, the mechanical properties of stainless steel 304 (304 SS) can be calculated, without conducting experiments, so as to examine the results of combining different parameters.

1.2 Objectives

On the basis of the above background information, the major objectives of this research are:

1. to build a model and determine the relationship between the number of ball

- impacts and processing duration of SMAT, and the number of balls;
2. to develop a constitutive model that represents the relationship between the flow stress and the grain size, twin spacing, strain, strain rate and temperature;
 3. to develop a finite element model for simulating the SMAT process and estimating the grain size and twin spacing after the SMAT treatment.

1.3 Engineering Significance

Metals are hard, ductile and thermal conductive materials, and are widely used in different areas especially in the automotive, aerospace and marine industries for producing outer shells or engine components. Insufficient protection of a metal may cause a drastic failure or even a disaster. It is obvious that the high strength and high ductility material is demanded in the future when fabricating the protective components.

Nanotechnology is one of the most efficient and feasible techniques to produce desirable metals. SMAT can dramatically increase the strength of a treated metal surface. The refined nano-grains are highly concentrated on the top surface and up to

several micrometers in depth. This surface protection is well suited for manufacturing the outer shell to enhance protection.

In accordance with different applications, metal strength and ductility properties may be different. Conducting unlimited experiments on numerous types of metal is a waste of time and resources. The development of simulation can act as a prediction and design tool before SMAT. It saves time compared to conducting experiments when seeking the perfect match between duration and number of balls for the SMAT, enabling the metal to be manufactured with the desired strength.

1.4 Scope of Work

Developing an accurate simulation model for SMAT is the main task in this study. To achieve the objectives stated above, the following tasks were completed.

- 1) The work done by other researchers on SMAT, other surface treatment processes, microstructure behaviors and mechanisms, finite element analysis on different manufacturing processes, metal plasticity theory and constitutive modeling on material property were reviewed.

- 2) The duration of SMAT is an important measure in the process. A model was built to quantify the duration of SMAT for the frequency of ball impacts used in the simulation.
- 3) A constitutive model was developed that represented the contribution of grain refinement and twin spacing in the residual stress, i.e. the residual stress was not only caused by the energy of the ball impacts, but also by the microstructure refinement.
- 4) The simulation on balls impacting on a target plate with the application of conventional governing material law and constitutive model were conducted.
- 5) The developed constitutive equations and simulations results were compared with those reported in the relevant literature.

1.5 Organization of this Report

This report is divided into 7 chapters:

Chapter 1 introduces the background of the research problem and clarifies the direction and objectives. The engineering significance shows the value and application

of the research technique. The scope of work summarizes the work done to achieve the objectives listed.

Chapter 2 reviews previous research on SMAT and other surface treatment. The works on finite element analysis for various manufacturing processes are also studied. The dynamic simulation is based on the material properties. Earlier research proposing models to describe the flow stress are also addressed in this chapter.

Chapter 3 describes the model developed for simulating the flying balls in the SMAT chamber. The relation between the duration and the number of ball impacts on the sample is discussed. Some other factors affecting the SMAT process are also presented in this chapter.

Chapter 4 explains the theory on the development of constitutive equation in describing the material properties during SMAT, with the metal plasticity theory applied in the subroutine writing on the finite element analysis (FEA).

Chapter 5 shows the FEA results by implementing the conventional governing material equation. The impact positions and velocities are based on the MATLAB simulation to imitate the ball impact in SMAT.

Chapter 6 further demonstrates the FEA by the implementation of the new constitutive equation. A subroutine program is written and runs in the FEA to calculate the increment of equivalent plastic strain and stress. The simulation results are then compared with the experimental results reported in the literature.

Chapter 7 concludes the contributions of the research work and recommends further developments in the future.

CHAPTER 2 - LITERATURE REVIEW

2.1 Introduction

In recent decades, a significant progress has been made in material processing technology (Ye, et al., 2014; Ye, et al., 2015). Nanocrystallization can successfully enhance metals with greater strength. The principle and various methods of nanocrystallization are reviewed here before further discussion.

The objectives of this study are to simulate the SMAT process and to predict the residual stress of the treated material. An understanding of the nanostructure after processing is crucial for the development of computational analysis. The marked experimental findings for common metals are reviewed, followed by a discussion of the grain refinement mechanism.

A comprehensive review on the description of residual stress and microstructure is conducted. The strength and ductility of a metal are affected by its microstructural evolution. To develop a new constitutive equation to model the effect of the microstructure on the strength, the relationship between the microstructure and residual stress should be quantified with different approaches. Studies on

microstructure modelling are also discussed for further development of a constitutive model.

Simulation of microstructure and prediction of the mechanical properties of material are a current trend in materials science. Recent studies with finite element modelling are summarized to benefit from their findings.

2.2 Nanocrystallization (NC) Process

After the discovery of nanostructure in metal composites in the 20th century, scientists rarely addressed the detection and production methods of nanostructure materials (Aliofkhazraei, 2015). Nanocrystallized metals provide increased strength and fracture behaviour via a reduction in their grain size. According to the Hall-Petch relationship, the decrease in the grain size at 100 nm results in an increase in strength (Hall, 1951; Petch, 1953). In a "top-down" procedure, coarse-grained metals are refined to smaller-grained metal. Various production methods, such as Severe plastic deformation (SPD), SMAT (Lu & Lu, 1999), High Pressure Torsion (HPT) , Equal Channel Angular Pressing (ECAP), and Air Blast Shot Peening (ABSP), are capable of producing metal

with ultrafine-grained materials and nanocrystal grains (Azushima, et al., 2008). The details of these nanotechnologies are reviewed in a later section 2.2.1 - 2.2.4.

2.2.1 Surface Mechanical Attrition Treatment

Surface treatment is a common method of enhancing the strength of metallic materials. It protects the surface of the metal without affecting its inner structure or changing its chemical composition.

Lu and Lu (1999 & 2004) invented a new surface treatment production method, SMAT by refining the grain on the metal surface. Figure 1.2 illustrates the configuration of the SMAT system. A number of rigid balls with smooth surface are randomly placed in a chamber. The balls can be made of stainless steel (SS) or ceramic, depending on the target metal. A horn or vibration table is installed at the bottom of the chamber and connected to a booster and converter. A generator is connected to the converter that can also control the vibration frequency output to the ball between 50 and 20 kHz (Azadmanjiri, et al., 2015).

Before conducting SMAT, the metal sample must be heated to release all residual stresses. The specimen is then mounted at the top of the chamber with one surface facing down toward the balls. During the SMAT process, the balls are resonated by the vibration of the horn and fly toward the sample. When the ball randomly strikes the sample, plastic deformation is initiated in multiple directions (Figure 2.1). The velocity of the balls is 1 to 20 m/s (Lu & Lu, 2004).

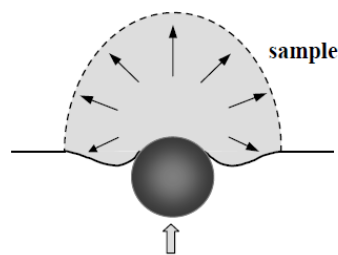


Figure 2.1 Plastic deformation direction of sample surface after impact in SMAT

(Lu & Lu, 2004)

In a normal impact, the ball strikes the sample surface vertically. The metal piles up around the milling ball and create an impression on the metal (Figure 2.2 (a)). In an oblique impact, the ball is flying at an angle to the surface normal. The direction in which the metal piles up is the direction of the impact (Figure 2.2 (b)). Because the ball bounces off the sample, a small amount of the pile-up material detaches (Figure 2.2 (c)). At the next impact, if the ball strikes the piled-up region, the region is

deformed (Figure 2.2 (d)) (Arifvianto, et al., 2012). By repeating impacts from multiple directions, the slip system changes with strain inside the same grain.

Therefore, the grains can be subdivided into smaller grains even to a nano-scale.

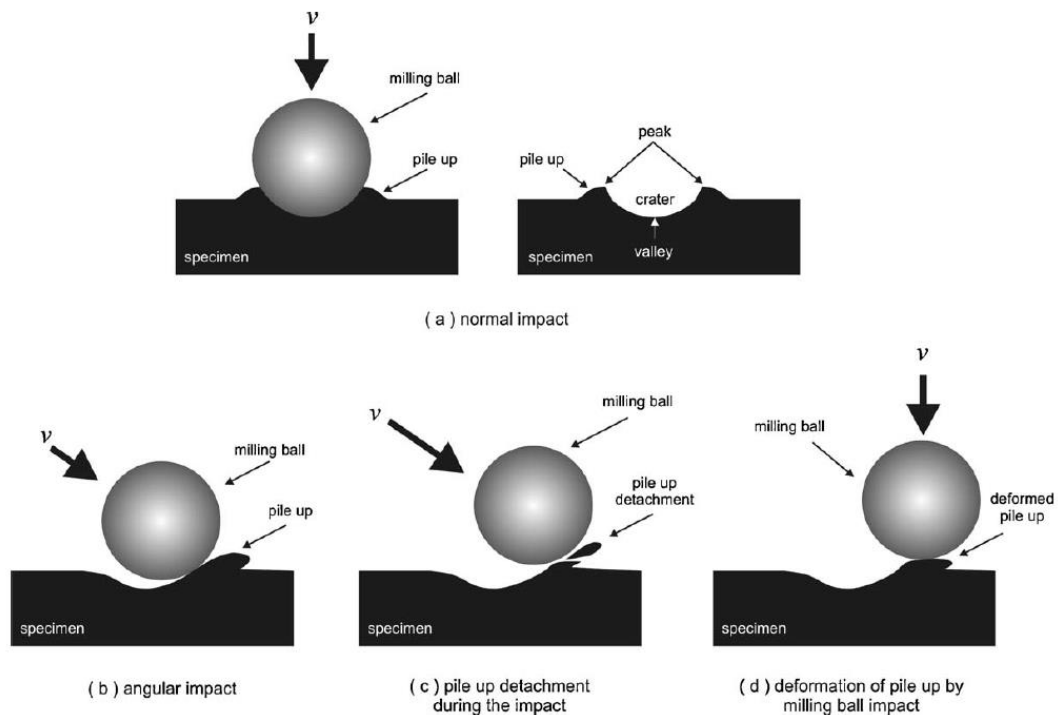


Figure 2.2 Surface evolution during SMAT (Arifvianto, et al., 2012)

Different materials may have different responses to SMAT. The thickness of the nanostructural layer varies according to many factors, including the size and material of the balls, the vibration frequency of the horn, and the processing duration. Figure 2.3 illustrates the microstructure distributions after SMAT (Lu & Lu, 2004). In general, when the strain and the strain rate are large, the grain sizes on the treated surface can

be a few nano-meters and the depth of the nanostructure can be up to 50 μm . Under the nanostructured layer is a submicrostructured layer. Less energy can be transmitted to this layer during the ball impacts, which leads to further decreases in the strain and the strain rate. The grain size is as fine as several micrometers. The energy transferred to the third layer is significantly decreased and the deformed coarse-grained layer is formed. The final layer is a strain-free coarse-grained matrix. The balls' impact has no effect on this region. It can be concluded that the grain refinement process is due to the gradient variation of the strain and the strain rate at different layers. The dislocation formation affects the accumulation of strains. The energy for dislocation activity decreases sharply at the deeper layers, which results in reduction in the strain and the strain rate.

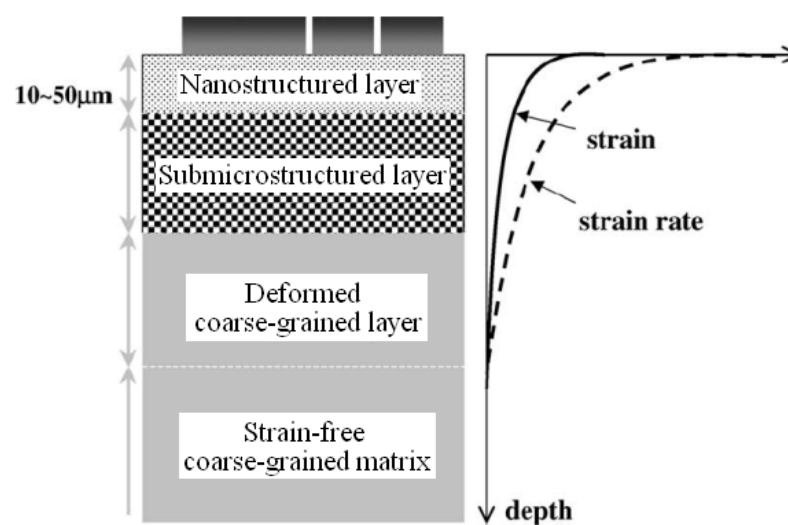


Figure 2.3 Microstructures, strain, and strain rate distribution along the depth from the sample surface in SMAT (Lu & Lu, 2004)

2.2.2 High Pressure Torsion (HPT)

The first study on HPT was performed by Bridgman in 1943. (Bridgman, 1943). High pressure and torsional strain are applied together on a short specimen to increase its ductility and to prevent the buckling effect for long specimens. As reviewed by Zhilyaev and Langdon, even though the torsional strain was increased, the precise value of the strain was difficult to define in this early work (Zhilyaev & Langdon, 2008). On the basis of this work, a modified HPT process was introduced by Valiev and his colleagues in 1993 (Valiev, et al., 1993), whose HPT system was based on the design of the Bridgeman anvil-type device, as illustrated in Figure 2.4 of the new model (Valiev, et al., 2006). A disc-shaped metallic sample is initially placed in a cavity between an anvil and a support. Great hydrostatic pressure is then applied to the sample by rotating the anvil. The sample is subjected to torsional strain. In strain hardening, the polycrystalline structure undergoes grain refinement to a nanocrystalline structure. The grain size varies from 50 to 100 nm, depending on the sample material (Valiev, et al., 1993; Zhilyaev, et al., 2003; Pakieła, et al., 2006;

Sakaia, et al., 2005; Valiev & Langdon, 2006; Valiev, et al., 2006; Zhilyaev & Langdon, 2008). The thickness with HPT is generally about 0.3 mm. The refined grain size varies gradually from the center. The advantage of HPT is its high grain refinement and suitability for even brittle materials. However, it cannot be used with bulk materials and the distribution of the refined grains is unevenly from the disc center.

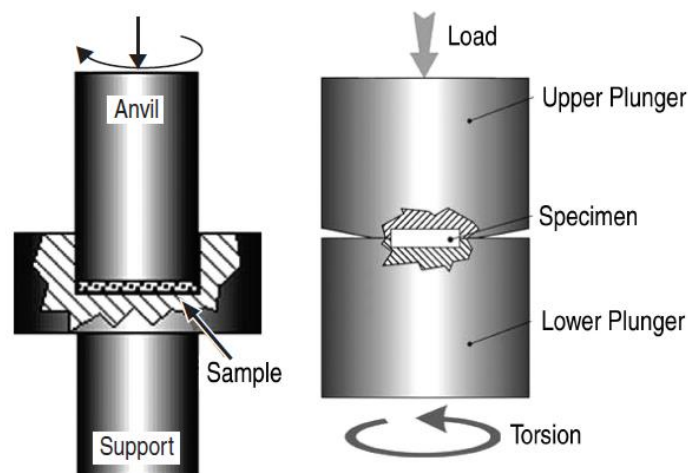


Figure 2.4 Representation of HPT (Valiev, et al., 2006)

After compression, the metal is annealed at a high temperature to achieve higher yield stress than with the coarse-grain size. However, comparing with other severe plastic deformation processes, ductility is still sacrificed. In addition, HPT is better for the production of specimen in disc form than for cylinders due to the lack of

microstructural homogeneity in its vertical section. Mass production in a large sample is also difficult (Zhilyaev & Langdon, 2008).

2.2.3 Equal Channel Angular Pressing (ECAP)

By the principle of strain hardening, ECAP is another renowned severe plastic deformation processing technology. As with forging and extrusion, a rod-shaped sample is pressed by a plunger into a die containing two channels with equal cross-sections. The channels are bent at an abrupt angle (ϕ) and addition angle (ψ) as illustrated in Figure 2.5 (Iwahashi, et al., 1996; Pakiela, et al., 2006; Valiev & Langdon, 2006; Valiev, et al., 2006). The sample is undergone a shear strain when passing through the intersection of two channels and the slip plane is formed after pressing. With adjustment of the angles or repeated pressing, a different slip system is formed (Iwahashi, et al., 1996; Nagasekhar & Kim, 2008; Valiev, et al., 2006). Because the cross-sectional areas of the two channels are the same, the size of the sample remains unchanged. Only grain refinement is induced by the high plastic straining.

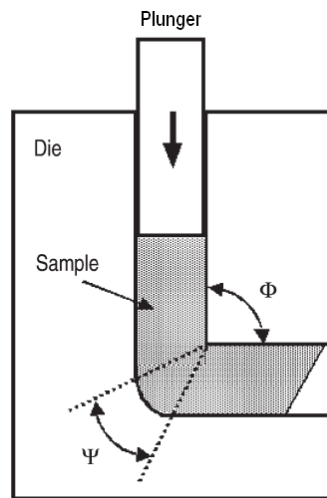


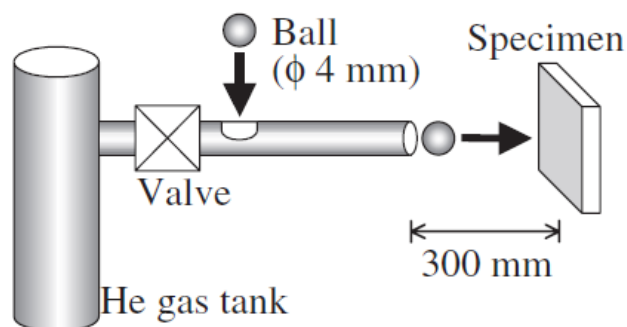
Figure 2.5 Illustration of equal channel angular pressing (Valiev, et al., 2006)

Unlike HPT, a larger sample can be pressed with ECAP to produce an ultra-fine grained structure. The grain size after ECAP is on the micro-scale, which is larger than the processes of SMAT and HPT (Pakiela, et al., 2006). For some specific metals, the grain size may be reduced to the nano-scale but still over 200 nm.

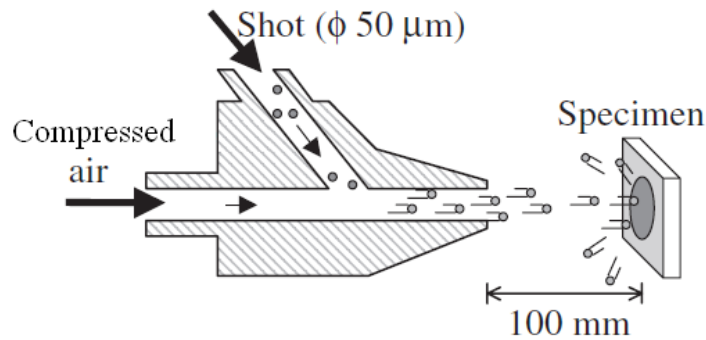
2.2.4 Air Blast Shot Peening (ABSP)

ABSP is a surface nanocrystallization process by strain hardening. The working principle of ABSP is illustrated in Figure 2.6. A number of small balls are inserted into the tube of the device. With a high pressure light gas gun, compressed air is used to produce a large force to shoot the balls at the specimen (Umemota, et al., 2003;

Todaka, et al., 2004). The shots are unidirectional and normally perpendicular to the specimen's surface. The diameter of the shot can be as small as 50 μm with a velocity over 100 m/s. The impact on the specimen's surface produces a large quantity of energy that causes surface plastic deformation. The formation of a nanocrystalline structure is dependent on the ball size, the coverage and the distance between the gun and the specimen. Umenota (2003) showed that, each shot can have coverage of more than 50 % at 100 mm. The strain was between 7 and 31 % for steel. The grain size was estimated at 260 nm with a flow stress of 1.4 GPa.



(a)



(b)

**Figure 2.6 Set-up of Air Blast Shot Peening at: (a) the whole view;
(b) the cross-sectional view (Umemota, et al., 2003)**

Since ABSP is a unidirectional process, refinement of the grain depends greatly upon the target material and the shot direction (Umemota, et al., 2003; Todaka, et al., 2004). Similar to the SMAT process, the grain sizes increase with the depth from the specimen's surface.

2.3 Experiments on Various Metals using SMAT

The major advantage of SMAT over other nanocrystallization processes is its ability to produce evenly distributed nano grains on the metal surface. In past years, many

studies have been conducted on various metals to produce nano grains on the surface layer with SMAT. This section summarizes the performance of SMAT on different metals in particular AISI 304 SS.

2.3.1 AISI 304 Stainless Steel

AISI 304 SS is a face-centered cubic (FCC) structured material with low stacking fault energy (SFE) (Tao, et al., 2003). Over the past decade, experiments have been conducted by many researchers to investigate its mechanical properties and microstructure after SMAT. In the experiment conducted by Zhang et al. (2003), a 304 SS plate was annealed in vacuum at 1080°C for 1 h before SMAT for 15 min. The vibration frequency was set at 50 Hz. The grain size increased with the depth from the surface as illustrated in Figure 2.7. At the surface, the grains were refined and the grain size was mostly around 11 nm, and martensite transformation was found. At a depth of 15 μm , the grain size ranged from 8 to 140 nm, with an average value of 30 nm. At a depth of 30 μm , the grain size was about 60 nm. Mechanical twins with a thickness of 300 μm were observed at the surface. The density of the mechanical twins increased as the depth increased.

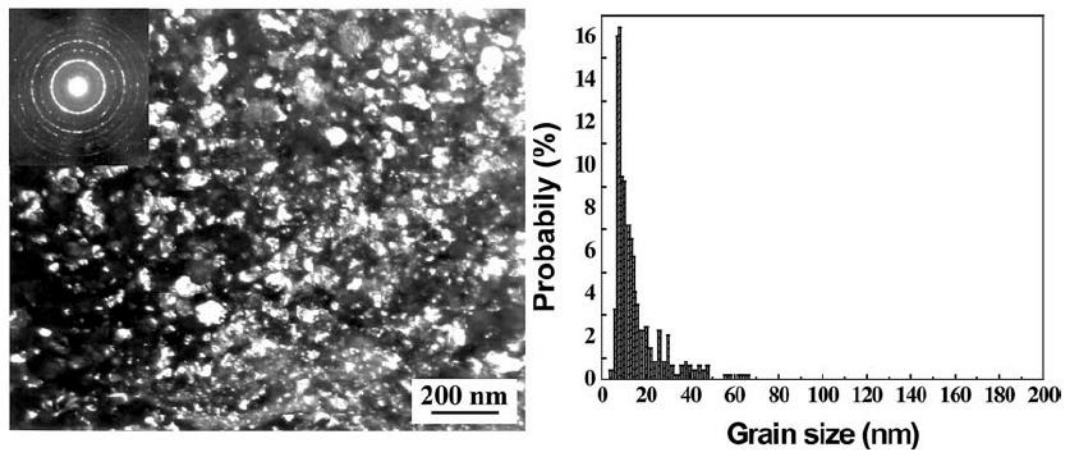


Figure 2.7 TEM image and grain size distribution on the top surface annealed at 1080 °C and SMAT for 15-min process (Zhang, et al., 2003)

Similar results were also found in other studies at two different strain rates (Chan, et al., 2010; Chen, et al., 2011). The use of 100 balls gave a higher yield stress than the use of 50, 200, or 400 balls. A longer processing duration could have a positive effect on the SMAT. The settings of SMAT used by Chen et al. (2011) are summarized in Table 2.1. When the balls make impact at a high velocity, the metal is deformed drastically to give a high strain rate. Martensite transformation was observed in both cases. The grain size at the surface ranged from 2 to 100 nm, with an average size of 10 nm at a low strain rate. This result perfectly matched that of Zhang et al. (2003). The grain size was much large in cases with a high strain rate than in those with a low strain rate, which averaged 120 nm for α' -martensite and 250 nm for γ -austenite

grains. Denser deformation twins were found in 304 SS, even at a depth of 50 μm from the surface. The high strain rate is not good for the reduction of the grain size due to the hindering effect of α' -martensite transformation. However, this effect is the main mechanism by which the low strain rate can produce nano-grains.

Table 2.1 Settings of SMAT for AISI 304 SS with different strain rates
(Chen, et al., 2011)

	SMAT – L	SMAT – H
Strain Rate (s^{-1})	$< 5 \times 10^3$	$5 \times 10^4 - 1.2 \times 10^5$
Ball velocity (m/s)	0.5	10
Vibration frequency (Hz)	50	20000
Ball material	GGr15	Bearing steel
Ball diameter (mm)	8	3
Duration (min)	40	15
Residual strain	0.07	0.2

The hardness of coarse-grained AISI 304 SS is generally 200 MPa; however, after the SMAT process, it can be increased to a maximum of 495 MPa at the surface

in both cases. The ultimate engineering stresses of samples with high and low strain rates were over 1000 and 800 MPa respectively, which were much higher than that with coarse-grained 304 SS. The engineering strains were approximately 35% for the sample with a high strain rate and 52% for the sample with a low strain rate, as illustrated in Figure 2.8.

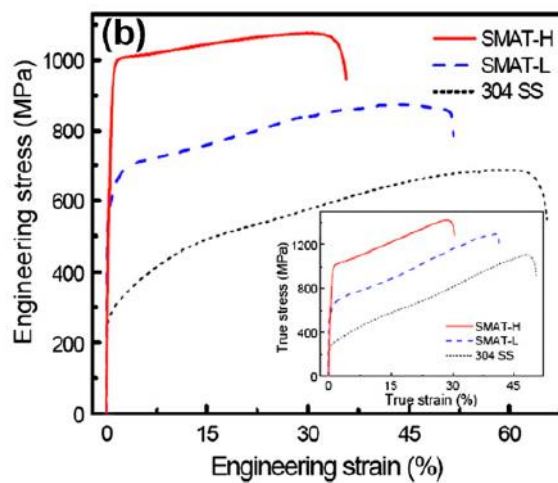


Figure 2.8 Engineering stress-strain curves of AISI 304 SS (Chen, et al., 2011)

The SMAT cannot only improve the mechanical properties, but also the corrosion resistance (Balusamy, et al., 2013). When a larger ball size is used for SMAT, the corrosion resistance is greatly improved.

The yield strength and ductility could coexist by cold working after the nanocrystallization process (Wang, et al., 2002). To achieve further enhancement of

strength and ductility, a second processing stage was applied after SMAT in a laminate structure, as shown in Figure 2.9 (Chen, et al., 2007; Chen, et al., 2008 ; Lu, et al., 2011; Guo, et al., 2012; Chen, et al., 2014). One AISI 304 SS was firstly treated by SMAT and then fabricated in a layered structure for further warm co-rolling, resulting in great strength the layer-structured metal, which was greater than that of the single layer metal after SMAT. The engineering strain reported in the literatures is similar to that of a single metal with SMAT. The annealing temperature also affected the strength of the metal. An excessively high temperature resulted in a weaker yield and ultimate stresses after co-rolling.

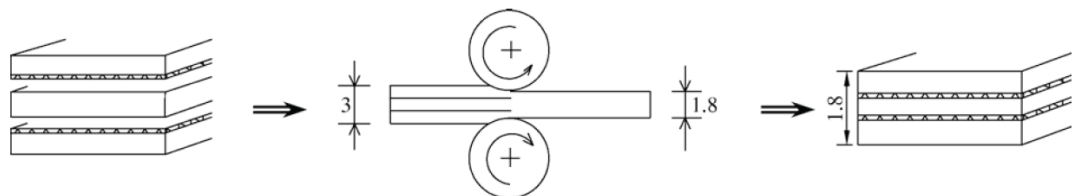


Figure 2.9 Schematic diagram of warm co-rolling process (Lu, et al., 2011)

2.3.2 Copper

Copper is also a FCC metal with a medium SFE. Nano grains are formed on the surface after the copper underwent SMAT for 30 min. Generally, the grain size ranged from

30 to 100 nm (Dao, et al., 2006, Guo, et al., 2006, Wang, et al., 2006), which is larger than the grain size of 304 SS. The grain size increased directly with the depth from the surface, and the processing duration of SMAT also had a direct effect on the grain size. The grain size after 30 min of SMAT was smaller than after 5 min of SMAT (Wang, et al., 2006).

Twinning was also observed in copper after SMAT. Denser twins were found with a higher strain rate and plastic strain. As seen in Figure 1.1, the strength and ductility of nano-twin copper surpassed those of the nanocrystalline copper. Twinning had a major and significant effect on both strength and ductility.

2.3.3 Titanium

Many experiments have also been conducted on metals other than AISI 304 SS and copper to investigate the differences in their behaviours after SMAT. Titanium is a well-known hard metal commonly used in the aerospace industry. When titanium is treated with SMAT, a nanostructure develops on its surface (Zhang, et al., 2004; Zhu, et al., 2004; Gallitelli, et al., 2014). As reported by Zhang et al. (2004) and Zhu et al. (2004), the nanostructure of the titanium after SMAT could be as thick as 50 μm . The

grain size was between 50 and 250 nm and averaged in 150 nm at the top surface (Zhu, et al., 2004). Twins formation was found in the nanostructure layer and polygonal submicronic grains were formed in the micro-grain layer, these structural observations are similar to those of AISI 304 SS.

The hardness of treated titanium decreased with the depth (Zhang, et al., 2004; Gallitelli, et al., 2014). The surface hardness increased by 15% over that of the coarse-grained titanium. When compared with the shot peening, metal that underwent the SMAT process at high velocity had a high level of micro-hardness due to the presence of the nanostructure as a result of the multi-directional impacts from SMAT in the refinement of the grain (Gallitelli, et al., 2014).

2.3.4 Other Metals

Other metals have also been examined with SMAT, including iron (Tao, et al., 2002), alloys (Azadmanjiri, et al., 2015) and other type of SS (Chen, et al., 2005; Michiuchi, et al., 2006; Balusamy, et al., 2010; Chemkhi, et al., 2013). A nanostructure was formed on the surface of each of these metals. Tao et al. (2002) found that when the

micro-strain increased over 10^4 , the grain size decreased to the nano-scale to a depth of 15 μm , followed by sub-grain layer to a depth of 40 μm .

The nanocrystallization process of other types of SS obtained similar results. For AISI 316L austenitic SS (316L SS), the average grain size was found to be 40 nm in γ -structure. The yield stress was examined as high as 1.45 GPa, which also obeyed the Hall-Petch relationship (Chen, et al., 2005). However, low strain is an issue in the nanostructure metal. In addition to the mechanical properties, corrosion resistance is also considered in other studies. Under the high strain rate of SMAT, the surface roughness improved, especially with the use of larger SS balls (5 mm and/or 8 mm) for a longer processing duration (e.g., 30 and 45 min). However, the corrosion resistance decreased with the increase in micro-strain (Balusamy, et al., 2010) due to the defect density induced in the process. In contrast, the use of smaller balls and/or a shorter processing duration can improve corrosion resistance by passive film formation. To improve corrosion resistance, AISI 316 austenitic SS underwent SMAT and nitriding for 20 h (Chemkhi, et al., 2013). The thickness of the nitrided layer was increased, and the hardness of the nitrided SS was improved because the SMAT first refined the grain to nano-scale so that the nitrogen content could dissociate deeply into the metal.

In twinning-induced plasticity (TWIP) steel, twinning is the major deformation mechanism that subdivides the grains (Li, et al., 2012). The width of the intersection of mechanical twins was reported at 20 nm in two directions. The size of rhombic blocks formed by intersecting twins ranged from 80 to 100 nm. The formed twins in TWIP steel differed from those of AISI 304 SS at a 150- μm depth after SMAT. The multiple twins were wider, and the rhombic blocks at the intersection of different directional twins were smaller in TWIP steel than in AISI 304 SS. The twin spacing decreased to refine the grain by a single twin, whereas the intersection of multiple twins occurred in the refinement of grains.

2.4 Nanocrystallization Mechanism

Dislocation, grain boundary, phase transformation and/or twin formation always appeared in the grain refinement (Tao, et al., 2002; Tao, et al., 2003; Zhang, et al., 2004; Lu & Lu, 2004; Guo, et al., 2006; Chan, et al., 2010), which is the major process in the nanocrystallization of metals in SMAT. An understanding of the grain refinement mechanism is critical for simulation of the SMAT process.

2.4.1 Grain Refinement Mechanism of Metal with Low Stacking Fault Energy

The grain refinement mechanism of low SFE is illustrated in Figure 2.10 (Tao, et al., 2003). Twins and dislocations formations are two major processes in low-SFE metal to form a nanostructure. During the nanocrystallization process, high-density twins are formed in the coarse grains, which are subdivided into twin laminates (process 1). Two conditions may appear in SFE metals.

Micro-twins are grown inside the grains only, and not across the twin boundaries. The driving force for such dislocation movement is insufficient to overcome the barrier of the grain boundary. An increasing number of micro-twins are formed in the twin laminate. When the strain increases, plastic deformation is triggered until the formation of mechanical micro-twins is saturated. A dislocation wall is then formed in the twin laminate to balance the increase in strain energy (process 2A). A strain-induced sub-boundary is formed from the dislocation wall at which smaller grains are developed (process 3).

An alternative condition after the formation of twin laminate is the development of twin-twin intersection. The driving force of the mechanical twins is sufficiently large to overcome the barrier of the twin boundary. A new twin boundary can be developed at the intersection of the twins (process 2B). A misorientation equiaxed nanometer-sized block is formed (process 3). The boundary formed is a large-angle boundary that increases the boundary misorientations in the accumulation and annihilation of dislocations at the grain boundary.

Smaller grains are formed by repeating the above mechanism inside an individual grain. The misorientated nanometer-sized blocks are finally developed as rotational and sliding of the grains and the grain boundary become easier on the nano-scale (process 4).

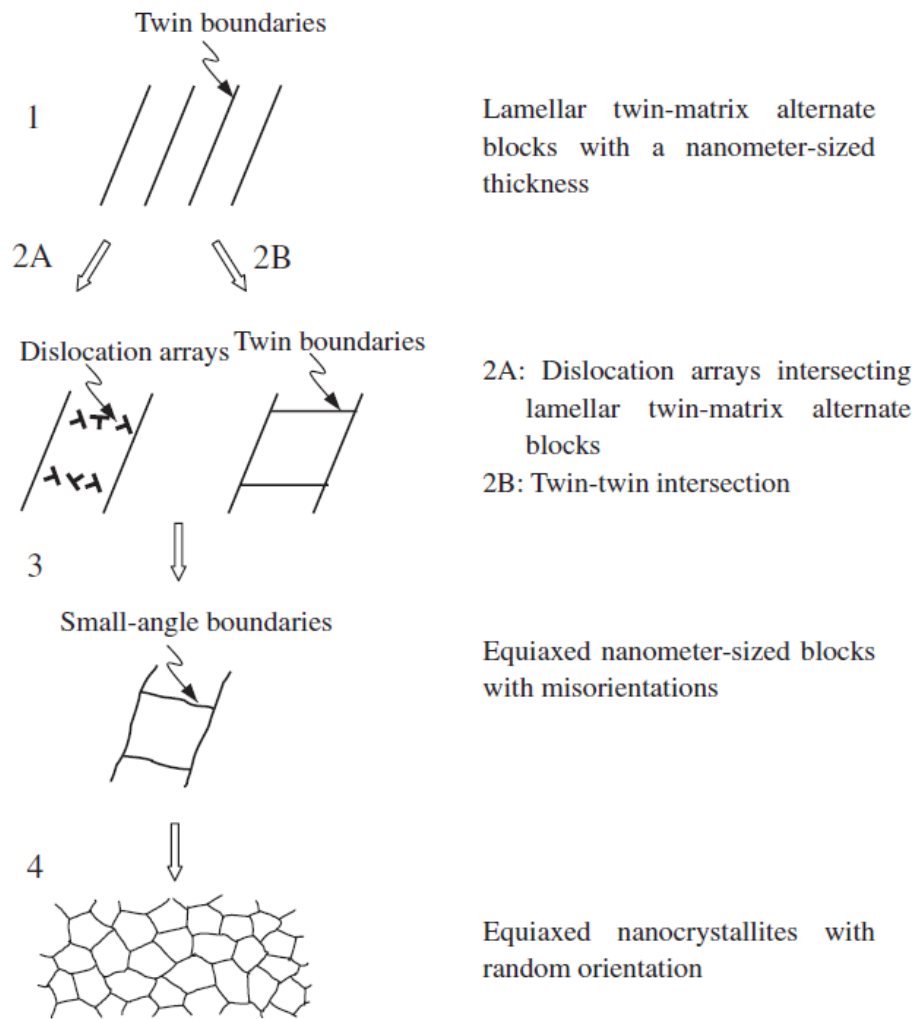


Figure 2.10 Illustration of the grain refinement mechanism of low SFE metal (Tao, et al., 2003)

2.4.2 Grain Refinement Mechanism of High Stacking Fault

Energy Metal

As reported by Tao et al. (2002), there are two grain refinement mechanisms for high-SFE pure iron. As illustrated in Figure 2.11, either dense dislocation walls (DDWs) or dislocation tangles (DTs) developed inside an original grain. DDWs and DTs are transformed into sub-boundaries by further straining together with misoriented cells or sub-grains. Sub-boundary would be developed to a new highly misoriented grain boundary. By repeating the above movement of DDWs or DTs, a large grain is refined to be nanostructure.

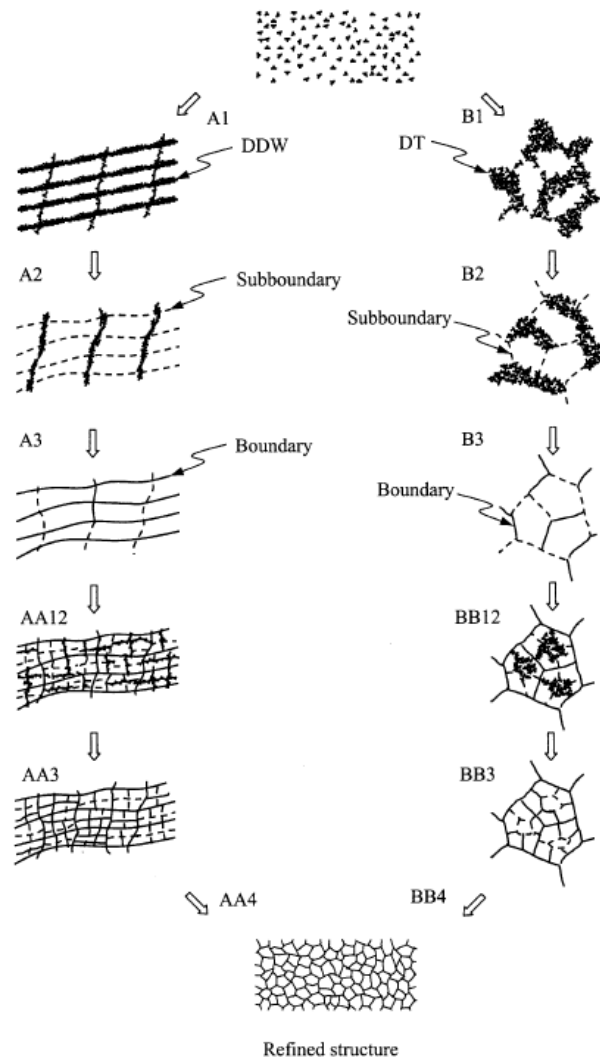


Figure 2.11 Schematic diagram of the grain refinement mechanism of pure iron

(Tao, et al., 2002; Azadmanjiri, et al., 2015)

2.4.3 Martensite Transformation

In some cases, martensite transformation occurs during grain refinement in the twin-twin intersection. As illustrated in Figure 2.12 (Sheng, 2011), dislocation forms in

multiple directions. Similar to the twin-twin intersection development, twin laminate is formed with the increase in strain. In the formation of a twin-twin intersection, the martensite transformation takes place at the intersection. The series of processes repeats until the nano grains are formed.

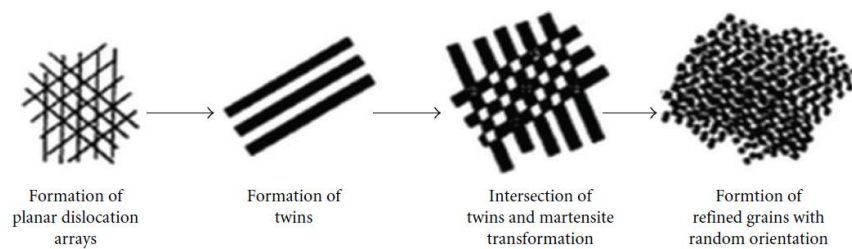


Figure 2.12 Illustration of the grain refinement with martensite transformation

(Sheng, 2011)

2.5 Numerical Modeling

The evolution of the microstructure affects stress and strain of the material. In the grain refinement process, the grain size is reduced and twins are produced for low SFE material, such as AISI 304 SS or 316L SS. Quantification of the grain refinement and twin formations can predict the effects of stress. In this section, the modeling related to the grain size, twins size, and residual stress is reviewed.

2.5.1 Residual Stress Modeling

During the SMAT process, the plastic deformation on the surface was mainly determined by the strain and strain rate. The high velocity of the ball impacts on the metal developed a range of strains, strain rates, temperatures, and pressures. The strain rates especially, defined the metal that was under a dynamic process rather than static loading.

A constitutive model developed by Johnson and Cook described the flow stress as a product of the effects of strains, strain rates, and temperatures on metal (Johnson & Cook, April, 1983; Johnson & Cook, 1985). This experiment was conducted on an explosive impact. Many other researchers adopted this model to quantify the flow stress in an isotropic hardening situation (Rule & Jones, 1998; Liang & Khan, 1999; Umbrello, et al., 2007; Ruan, et al., 2010a; Ruan, et al., 2010b; Chen, et al., 2011; Visser, et al., 2011; Zhang, et al., 2011a).

In the Johnson and Cook's experiments, the metals underwent torsion test with one parameter varied each time. The Johnson-Cook (JC) relationship was expressed in the following:

$$\sigma_f = [A + B\bar{\epsilon}^n][1 + C \ln \dot{\epsilon}^*][1 - T^{*m}] \quad (2.1)$$

where A, B, C, m, and n are the material constants. σ_f is the flow stress. $\bar{\epsilon}^p$ is the equivalent plastic strain $\dot{\epsilon}^*$ is the dimensionless plastic strain rate as

$$\dot{\epsilon}^* = \frac{\dot{\epsilon}}{\dot{\epsilon}_0} \quad (2.2)$$

where $\dot{\epsilon}_0 = 1.0 \text{ s}^{-1}$, is the reference plastic strain rate. T^{*m} is the homologous temperature as

$$T^{*m} = \frac{(T-T_0)}{(T_m-T_0)} \quad (2.3)$$

where T_0 is the reference temperature. T_m is the reference melting temperature.

The first part of the JC equation is the strain function, the second part is a function of the strain rate, and the last part is the function of temperature. The flow stress is a function of strain for $\dot{\epsilon}^* = 1.0$ and $T^{*m} = 0$, which means that the material is currently at the melting temperature by the definition of Equation (2.3).

In addition to the JC model, some researchers developed another mathematical model to determine the flow stress. Yoshino and Shirakashi proposed a new equation to determine the flow stress, strain rate and temperature by plastic deformation energy (Yoshino & Shirakashi, 1997). In a Hopkinson bar-type impact test, a specimen was compressed with high pressure air. The flow stress and strain rate were determined

separately by the obtained strain. However, the relationships between the flow stress and the strain, strain rate and temperature history are not obvious.

A statistical method was used by Zhu et al. to predict the mechanical properties of bimodal metal (Zhu, et al., 2012). With a combination of coarse grains and nano/ultrafine grains, the polycrystalline metal acted as a composite mixture. Dislocations inside the grain and on the grain boundary were encountered to develop a new constitutive equation. The flow stress was a result of the dislocation density inside the grain and on the grain boundary.

The behaviour of the metal deformation may not be isotropic hardening. Kim et al. proposed that the mechanical properties of the crystalline phase of fine grained material could be modeled as viscoplastic material with dislocation density evolution (Kim, et al., 2000). With the same concept of the composite rule of mixture, the volume fraction and stress of intercrystalline components with grain boundaries were considered to calculate the final stress. Combined with the viscoplastic model, the plastic strain rate tensor can be expressed in term of the deviatoric stress tensor. In the nanocrystallization process, the grain was refined and the mechanical strength of the

metal become improves. However, only the strain or strain rate was considered in the above models. The evolution of the microstructure has not yet been considered.

The prediction of flow stress in superplastic alloys has raised the interest of researchers (McFadden, et al., 1999; Cheong, et al., 2000; Cheong, et al., 2001). McFadden et al (1999) proposed a combination of the activation of grain-boundary sliding, and an increase in diffusion and dislocation generation. Cheong et al (2000 & 2001) accounted for the strain rate and grain size in the viscoplastic constitutive equation. The flow stress was a summation of strain rate hardening, grain growth, isotropic hardening and yield stress. The grain refinement and strain rate effects have been considered in the contribution of the flow stress; only the strain is not considered. Grain growth also plays a key role in the hardening effect on the flow stress to the viscoplastic constitutive equation.

Twinning has also been considered in many studies to model the flow stress (Barnett, 2007a; Barnett, 2007b; Wei, 2011; Li & Soh, 2012). In the analysis by Wei (2011), the critical shear stress triggered the nucleation of partial dislocations. In the elastic-viscoplastic model (Li & Soh, 2012), intra-twin and twin-boundary-mediation (TBM) were two approaches of deformation mechanism in nanotwinned metals. The

former included the motion of dislocations inclining to the twin boundary emitted from the grain boundary, whereas the latter included the nucleation and movement of the twinning partials parallel to the twin boundary. These studies explained that twin formation is crucial in nano-scale metals.

2.5.2 Grain Size Evolution

As discussed in the previous section, the grain size has not yet been considered in the conventional residual stress calculation. Because the plastic deformation of metal is caused by grain refinement, the strength increases with a reduction in the grain size. As proposed by Hall and by Petch, the inversely relationship between the yield stress (σ_y) and grain size (d_G) has become a classical model, as shown in Equation (2.4) and Figure 2.13 (Hall, 1951; Petch, 1953). This equation is well-known and commonly used by other researchers to determine the stress and/or further development (Chou & Pande, 1972; Chokshi, et al., 1989; Kashyap & Tangri, 1990; Wang, et al., 1993; Takeuchi, 2001; Phaniraj, et al., 2007; Zhang, 2011a). The further reduction in the grain size strengthens the metal by increasing the yield stress until the grain size is

saturated at 10 nm. When the grain size is smaller than 10 nm, further reduction would only cause the yield stress to decrease instead.

$$\sigma_y = \sigma_0 + \frac{k}{\sqrt{d_G}} \quad (2.4)$$

where σ_0 and k are constants.

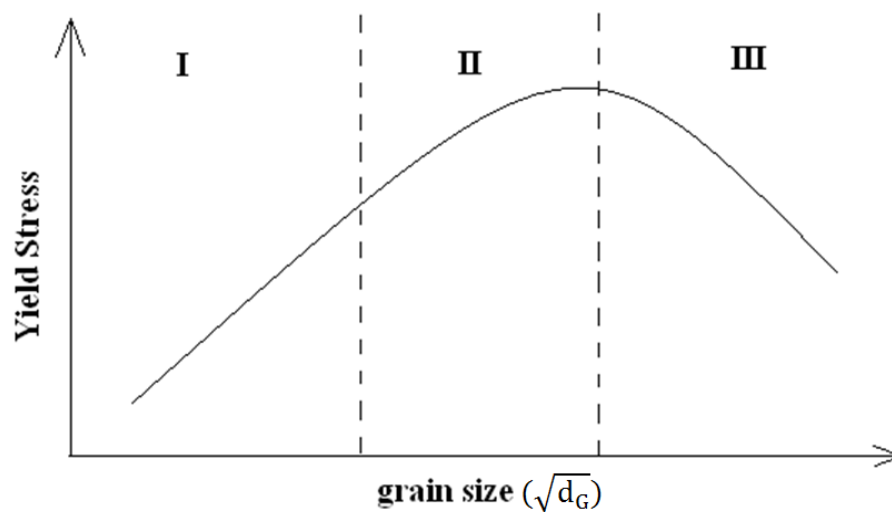


**Figure 2.13 Hall-Petch relationship between the yield stress and the grain size
(Hall, 1951; Petch, 1953)**

The yield stress can be easily determined by the grain size with the Hall-Petch equation. However, the yield stress is not only contributed by the grain size in the plastic deformation. The strain, strain rate or other microstructure parameters may also affect the mechanical stresses.

In the strain-induced deformation, the grain is not refined by the stress. For example, the grain was refined in the ECAP process, especially in multiple pressing processes. In the strain-induced situation, the grain size must to be defined according to different strain values (Kim & Kim, 2010). The grain size (d) is given by

$$\frac{1}{d} = \frac{1}{d_{\infty}} + \left(\frac{1}{d_0} - \frac{1}{d_{\infty}} \right) \exp\left(\frac{-\bar{\epsilon}^p}{\epsilon_c}\right) \quad (2.5)$$

where $\bar{\epsilon}^p$ is the equivalent plastic strain. d_0 is the initial grain size. d_{∞} and ϵ_c are material constants. The grain size is equal to the initial grain size when the equivalent strain is zero.

Some researchers have found some correlation between the grain boundary and the grain size (Tsureskawa, et al., 2006). It was found that 10% of atoms were found in the grain boundaries when the grain diameter was at 20 nm (Swygenhoven, 2002). Deformation was caused by the movement of grain boundaries by partial dislocations. In their simulation, when the grain size was 30 nm, full dislocations was found. By repeating the dislocations motions, the grain was refined. Dislocations were found to be active in the grain boundaries at a small grain size.

2.5.3 Twins Nucleation

As reviewed, the dislocation movement produced twins on a nano-scale when the strain rate is high to achieve greater strength (Bilde-Sørensen & Schiøtz, 2003; Meyers, et al., 2006; Lu, et al., 2009; Jain, et al., 2011). When the dislocation density is high, the stress increases. When the stress reaches a certain level, deformation twinning occurs and further narrows the separation between the twins. In extensive twinning, heterogeneous and homogeneous nucleation of the deformation twins appeared in the grain boundary and inside the grain respectively. The stress can then be as high as 2.5 GPa with a high level of plastic strain at 12% (Yamakov, et al., 2002).

Many experimental results have shown that nano-twins always appeared in various metals (Chen, et al., 2003; Wu & Ma, 2006; Michiuchi, et al., 2006; Kibey, et al., 2007; Xiao, et al., 2008; Li, et al., 2010). Quantifying the twin size and/or spacing have long been studied to determine the stress induced. Some researchers have developed two different equations to tackle different twinning dislocations, that is, perfect and partial dislocations (Chen, et al., 2003). The SFE affects mostly the partial dislocations.

Kibey et al. considered the twinning energy pathways in the twin nucleation process to predict the twinning stress (Kibey, et al., 2007). Three layers of twin nuclei were considered. Thus, the true twinning stress was then a function of the grain size and the fault energy.

In the expression of Equation (2.6), the relationship between the critical twin nucleus thickness (r_c) and the equivalent stress (σ) is simplified (Xiao, et al., 2008; Chen, et al., 2011).

$$r_c = \frac{5\pi G \gamma_{TB}}{4 \sigma^2} \quad (2.6)$$

where G is the shear modulus and γ_{TB} is the twin boundary energy.

This equation indicates that the twin nucleus thickness is inversely proportional to the square of the equivalent stress. The twin nucleus thickness is affected drastically by the stress. Because the stress is directly proportional to the strain, the strain would increase significantly with a decrease in the twin thickness. When the twin thickness decreases, the density of the twin increases, and the strain therefore increases. This confirms the experimental results that nano-twinned metal is more ductile than non-twinned metal.

As proposed by Zhu et al., a piled-up zone was enclosed in the grain boundary and twin boundary (Zhu, et al., 2011). Numerous tiny and dense dislocations were formed in the Twin Boundary Dislocation Pile-up Zone (TBDPZ) under deformation. The dislocation density in the TBDPZ is calculated by

$$\rho_{\text{TB}} = k^{\text{TB}} \frac{\tilde{\eta}^{\text{TB}}}{b} \quad (2.7)$$

where ρ_{TB} is the density of inclined dislocations in TBDPZ. b is Burgers vector. k^{TB} is a ratio of the thickness of the TBDPZ and the twin boundary. $\tilde{\eta}^{\text{TB}}$ is the effective local strain gradient in the TBDPZ.

2.5.4 Dislocation Density

The mechanism of plastic deformation in single crystal of metal was studied by Taylor in the early 20th century (Taylor, 1934a; Taylor, 1934b). The shear strain between the atoms affected the dislocation movement in the crystal. A slip of the atomic planes was caused by the discrete displacement discontinuities (dislocations). Based on this observation, Mecking and Kocks proposed an equation to relate the macroscopic behaviour and the property of dislocations (Mecking & Kocks, 1981). The following

Equation (2.9) expressed the relationship between the flow stress (σ_f) and the dislocation density (ρ).

$$\sigma_f = \alpha G b \sqrt{\rho} \quad (2.9)$$

where α is a constant of the ordering unit, depending on the strength of the dislocation.

b is the Burgers vector, and G is the shear modulus.

Proposed by Mecking and Kocks, the dislocation density was used to calculate the flow stress. However, other researchers believed that this equation was used to calculate the flow shear stress rather than the flow stress. The tensile flow stress should be multiplied by a constant, M (Wu, et al., 2011). They also developed mechanism-based strain gradient plasticity to consider the twins lamella and matrix lamella.

In the experiments by Ni et al., high dislocation densities were observed on the grain boundaries and twin boundaries (TBs) (Ni, et al., 2012). Under the plastic deformation, the dislocations on the grain boundaries and TB significantly refined the grains to the nano-scale.

2.6 Computational Simulation

Computational simulation has been widely applied in material science to predict the mechanical properties and microstructural evolution of the material. In the past decade, many studies on various severe plastic deformation processes have been conducted to simulate the fracture or stress-strain behaviour of the material.

2.6.1 Simulation of Nanostructure Production

FEA was used to simulate the equal-channel angular pressing process with ANSYS 5.5. The specimen was assumed under a loading with friction only. The microstructural evolution was not considered in this case. The deformation of the specimen under ECAP was simply considered macroscopically as isotropic hardening (Zhernakov, et al., 2001). Another study considered the effects of grain size on stress in the simulation of High Pressure Torsion process. The rigid-plastic finite element method was applied to study the homogeneity of internal stress and strain distributions to optimize the process on bulk materials for grain refinement and nanostructure (Yoon, et al., 2008). By developing a dislocation cell evolution constitutive model, the dislocation density and cell walls are applied on the model to calculate the stress and

strain values on the bulk material under the process. This method made use of the number of dislocation density and cell walls to compute the desired stress-strain values after the process.

The aforementioned simulation model on the nanocrystallization processes applied continuous loading to a specimen. The load was either constant or changed gradually. To simulate dynamic impact, another working principle was required. The approach for simulation of shot peening was similar to SMAT, as a ball flew towards the sample and impacted it in a short time. The stress induced by the impact was of interest to researchers (Meo & Vignjevic, 2003; Majzoobi, et al., 2005), who simulated the residual stress of sample after shot peening. A simple one-time impact was used in the simulation. Dynamic relaxation was applied to compute the permanent deformation and frictional effects to the model instead of the effect by elastic motion. With the aid of commercial software, ANSYS, the residual stress after an impact was computed. In a further development, multiple-impact simulation was studied by Majzoobi et al., whose study was quite similar to a real shot peening process as several balls impacted a unit area. A Johnson-Cook constitutive model was applied to assume the material under an isotropic hardening process. The balls were assumed to strike the target directly at different, but close, local points. In a real case, the ball may not

be shot in an even distribution to the target and numerous impacts may occur. The stress is not only a result of the mechanical impact of the balls, but also of the refinement of grain. In addition, the effects of the velocity and ball size have not yet been studied.

The effect of velocity in multi-directional impacts was studied with ANSYS (Du, et al., 2009). Different velocities were applied on a single ball in the simulations. In advance, a dynamic model was used to predict the stress on the specimen with impacts of various velocities. With the same diameter of ball, the ball velocity has significantly effects on the Von Mises stress. The stress on the impact area is directly proportional to the ball's velocity. However, the stress decreases with the depth from the surface. These simulation results matched the experimental results well. Other than the ball's velocity during impact, the ball size, the impact coverage and the incident angles of impact are the factors that may affect the residual stress in shot peening or SMAT. To answer these effects, Zhang et al. studied the coverage after SMAT and the effect of oblique impacts with ABAQUS (Zhang, et al., 2011a). 10 random shots were studied to determine the coverage and depth of impacts by two different ball sizes. Still, the microstructural influence to the stress was not included in their study.

As presented in the previous sections, a one-step surface treatment may not significantly enhance both strength and ductility. A laminated structure was developed and the numerical prediction was studied for comparison (Guo, et al., 2010; Guo, et al., 2012). SMAT and rolling processes created a number of cracks on the specimen. These studies determined the relationship between the number of micro cracks and the strain. A fundamental technique was used to investigate how the severe plastic deformation affects the strength of the material. More studies on the control of the crack distribution and single SMAT are required to systemize the SMAT process.

2.6.2 Simulation of Microstructure

Many researchers have developed various models for simulation of microstructure. In the involvement of twinning evolution, FEA had been used with the application of a constitutive equation (Thamburaja, et al., 2009). In this study, the evolution of microstructure was considered from the basis of single crystal to determine the stress.

Grain refinement of the microstructure or even nanostructure was simulated by the consideration of the grain boundary (Schiøtz, et al., 1997). The use of cellular automata is one of the recently used methods to simulate the grain structure. Xu and

Liu modelled the microstructure of aluminium alloy with cellular automata (Xu & Liu, 2001). Based on the physical mechanism of nucleation and the kinetic theory of grain growth, the grain growth was calculated when the temperature was lower than the melting temperature. The grain density can thus be calculated in this manner.

Salehi and Serajzadel applied coupled cellular automata and finite element modelling to evaluate static recrystallization kinetics during non-isothermal annealing of cold-deformed low-carbon steels (Salehi & Serajzadeh, 2012). The material domain was divided into some regular square finite small cells. The state of this cell was defined by crystal orientation, dislocation density, temperature, and phase type. The neighbouring cells with the same crystal orientation and phase type belongs to a specific grain and probabilistic transformation rules are applied to change the state of each cell. The cellular automata algorithm and governing physical principle can determine the static recrystallization.

2.7 Summary

This chapter reviews the mechanisms of various nanocrystallization processes to yield an overview of their advantages and disadvantages. The severe plastic deformation process and SMAT were introduced together with the experimental results for various common metals, including AISI 304 SS, copper, and titanium. Nano-twins, grain refinement and martensite transformation were observed after the SMAT process. The nano-twinned metal has better ductility than other nano-scale metals without twinning. By studying the grain refinement mechanism, the formation of twins has been understood and mainly occurred in the low SFE metals.

The constitutive models for quantification of the residual stress, grain size, twin spacing and dislocation density were also reviewed. These equations were useful in the development of a new constitutive model. The computational modelling of various nanocrystallization processes and microstructural evolution was briefly introduced to present the concept of simulation of the SMAT process in this study.

CHAPTER 3 - THE COMPUTATIONAL MODEL OF SMAT

3.1 Introduction

The changes in mechanical properties that occur after SMAT with a certain processing duration have been investigated in many studies (Tao, et al., 2002; Zhang, et al., 2003; Chan, et al., 2010; Balusamy, et al., 2013). However, to predict changes in mechanical properties, the relationship between the number of ball impacts and the processing duration must be determined. For this purpose, a dynamics model was developed to simulate the random motions of balls in the SMAT chamber and to obtain detailed information regarding the number of ball impacts, the impact positions, and the impact velocities. The details of the model are presented in this section, followed by experimental verification.

3.2 Assumptions

The following assumptions are made in the MATLAB simulation:

1) Principle of energy and momentum

In the ball-ball and ball-chamber collisions, the energy and momentum are conserved as a whole. So that the mass of the chamber and the balls should neither be deformed nor changed. Because no report of a dramatic decrease in the balls' velocities in the collisions was found in the literature, it is assumed that the dissipated energy during the collisions will be regained after the rebound on the horn. As a whole, the energy in the chamber is conserved.

2) Deceleration due to gravity is negligible

In the experimental setup for SMAT, the height of the chamber (H) was commonly set at 20 mm. If the maximum ball velocity is 10 m/s traveling vertically to the target metal, the rebound velocity is theoretically 10.02 m/s where the energy dissipation in the collision is small. If the ball velocity is 3 m/s before the collision, the rebound velocity is 3.065 m/s.

$$V_{\perp(t+\Delta t)}^2 - V_{\perp(t)}^2 = 2gH$$

The height of the chamber is low enough that the effect of gravity is only 0.2% to 2.2%. This is a very small effect when compared with the energy regain and

dissipation during the collision, that is, 5%. In this condition, the deceleration due to gravity after the collision is negligible.

3) Initial maximum ball velocity due to the power setting of the ultrasonic horn

In the simulation, all balls are assumed to occupy random positions in a 3-dimensional chamber and do not overlap. As an initial condition, the ball velocity is randomly assigned within a range. The ball velocity component normal to the ceiling has an initial maximum value due to the power setting of the ultrasonic horn. For example, Chen et al. (2011) found from their experiments that when the ultrasonic horn was used at a 35% power setting, the maximum initial ball velocity was 4.5 m/s; this value was used to constrain the initial maximum ball velocity in the simulation.

3.3 Modeling of SMAT

The cylindrical chamber with a radius (r) of 35 mm and a height of 20 mm for SMAT is schematically shown in Figure 1.2. The diameter of the metal balls generally used in SMAT is 3 mm. As depicted in Figure 3.1, the z-axis of the Cartesian coordinate

system lies along the axis of the cylindrical chamber and the origin of the coordinate system was set at the center of the chamber.

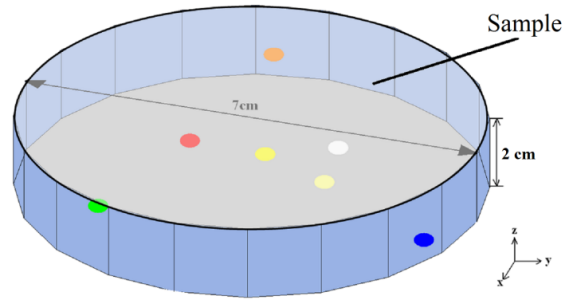


Figure 3.1 Configuration in the simulation model

For each simulation, a fixed number of balls are first placed in non-overlapping random locations on the chamber floor. The balls then begin to travel upward with a random orientation and a random speed less than or equal to the maximum ball velocity. Because the balls can only fly inside the chamber, the x - and y - coordinates of the balls must satisfy Equation (3.1), and the z -coordinate must neither exceed that of the chamber ceiling nor fall below that of the chamber floor.

$$\mathbf{x}^2 + \mathbf{y}^2 \leq (\mathbf{r} - 1.5)^2 \quad (3.1)$$

After updating the positions of the balls at each time step, the occurrences of collisions among the balls and between the balls and the chamber's wall, ceiling, or floor were checked. If a ball experienced a collision, its velocity was updated. A collision between two balls was checked by computing the updated distance between their centers. If the Euclidean distance between two balls was found to be less than the ball's diameter, a collision occurs between t and $t+\Delta t$. Because perfectly elastic collision between the two balls was assumed, the normal velocity was simply reversed and used in subsequent position calculations. A collision between a ball and the ceiling of the chamber occurred between t and $t + \Delta t$ if the z -coordinate of the ball was equal to or larger than that of the chamber ceiling. The velocity component normal to the ceiling was reversed, and the velocity component remained tangential to the ceiling. The impact position and velocity were both recorded for further use. The current position ($\mathbf{S}_{(t)}$) and velocity ($\mathbf{V}_{(t)}$) of the balls were used to determine the rebound position vector ($\mathbf{S}_{(t+\Delta t)}$) using the following Equations (3.2 - 3.5). Possible collision with the floor of the chamber was checked for in a similar manner. To ensure that no ball collision was left undetected, the time step was set to a value so small that the ball would travel a distance less than its diameter. For a maximum initial speed of 4.5 m/s and a ball diameter of 3 mm, the time step was set to a value below 0.667 ms.

$$\mathbf{S}_{(t+\Delta t)} = \mathbf{S}_{(t)} + \mathbf{V}_{(t)} \cdot \Delta t \quad (3.2)$$

$$\mathbf{V}_{(t+\Delta t)} = \mathbf{V}_{(t)} \quad (\text{no collision}) \quad (3.3)$$

$$\mathbf{V}_{\parallel(t+\Delta t)} = \mathbf{V}_{\parallel(t)} \quad (\text{after collision}) \quad (3.4)$$

$$\mathbf{V}_{\perp(t+\Delta t)} = -\mathbf{C}_R \mathbf{V}_{\perp(t)} \quad (\text{after collision}) \quad (3.5)$$

where \mathbf{V}_{\parallel} is the tangential velocity component; \mathbf{V}_{\perp} is the normal velocity component of the ball at the point of impact and C_R is the coefficient of restitution .

The bottom boundary was the horn surface of an ultrasound generator. The vibration amplitude was also involved in the simulation model. The vibration horn was a sinusoidal vibrating table. When the ball impacted the horn, the horn directed the ball's motion according to the vibration amplitude, and thus the rebound of the ball velocity after impact with the horn ($\mathbf{V}_{\perp(t+\Delta t)}$) can be obtained using Equation (3.6) (Luo and Han 1996).

$$\begin{aligned} \mathbf{V}_{\perp(t+\Delta t)} = & -\mathbf{A}_h \boldsymbol{\omega} \cos(\boldsymbol{\omega} \cdot (\mathbf{t} + \Delta \mathbf{t}) + \boldsymbol{\varphi}) - \mathbf{g}(\mathbf{t} + \Delta \mathbf{t}) \\ & + [-\mathbf{C}_R \mathbf{V}_{(t)} + \mathbf{g}(\mathbf{t}) + \mathbf{A}_h \boldsymbol{\omega} \cos(\boldsymbol{\omega} \mathbf{t} + \boldsymbol{\varphi})] \end{aligned} \quad (3.6)$$

where ω is the angular frequency of the vibration horn set at 20 kHz; A_h is the amplitude of the vibration horn; ϕ is the phase angle; g is the gravity at 9.81 m/s^2 , and C_R is the coefficient of restitution of the horn.

The vibration amplitude was controlled by the power setting at different percentages. Chan et al. (2010) determined the relationship between the power setting and the average ball velocities. The velocities of balls under different vibration amplitudes of the horn were also defined (Tsai, et al. 2015) . The relationship between the power setting and vibration amplitude is shown in Figure 3.2.

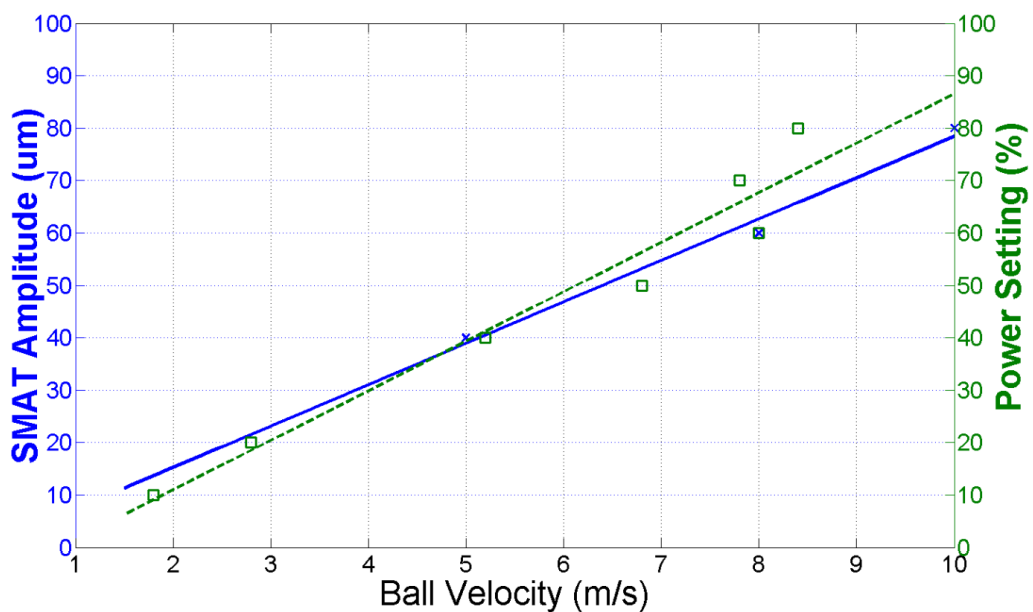


Figure 3.2 Relationship between the power setting of SMAT, the ball velocity, and the vibration amplitude of horn (Chan, et al., 2010; Tsai, et al., 2015)

The coefficient of restitution was not only applied for the collision with the horn surface, but also in the calculation of the rebound velocity in the ball-ball and ball-boundary impacts. In a collision, the lost fraction of kinetic energy is $(1 - C_R^2)$. A ball would gain energy after impacted on the horn surface that maintained the ball flying randomly in the chamber.

The relationships between the number of ball impacts, and the processing duration, and the number of balls were investigated by simulation. Different numbers of balls and processing duration were applied, and the corresponding numbers of ball impacts were determined. Details of the simulation are summarized in Table 3.1. Each set of simulations was conducted at least five times to ensure statistical reliability.

According to the study by Chan et al. (2010), an increase in the number of balls did not necessarily increase the efficiency of nanocrystallization because the number of ball impacts was not directly proportional to the number of balls. The efficiency of SMAT under different combinations of factors can be determined more accurately by counting the number of ball impacts via the simulation because it is very difficult to determine through experiments.

Table 3.1 Summary of various sets of MATLAB simulation

Duration (s)		5		10		15		20		25	
Number of Balls	50	70	100	125	150	170	200	230	250		

3.4 Demonstration of SMAT

To verify the computational result, experiments were conducted with the aid of a high-speed camera to capture images of the balls impacts. Figure 3.3(a) shows the setup of the experiment. A transparent cylindrical chamber was formed by placing an acrylic collar with a height of 20 mm and an inner diameter of 70 mm atop the 70-mm-diameter ultrasonic horn of the SMAT machine. The square acrylic target plate was placed atop the collar and fixed to the platform of the SMAT machine with a mounting plate as shown in Figure 3.3(b). A fixed number of stainless steel balls was placed inside the cylindrical chamber and excited at the 35% power setting of the ultrasonic horn for 5 s. The test was repeated three times to obtain a statistical average. A Phantom VR706 high-speed camera was used to capture the motion of the balls in an acrylic transparent chamber at a rate of 1000 frames per second. To facilitate later

distance measurement from the captured images, a paper ruler was attached to the wall of the acrylic chamber. The experiments were conducted for 50, 100 and 200 balls.

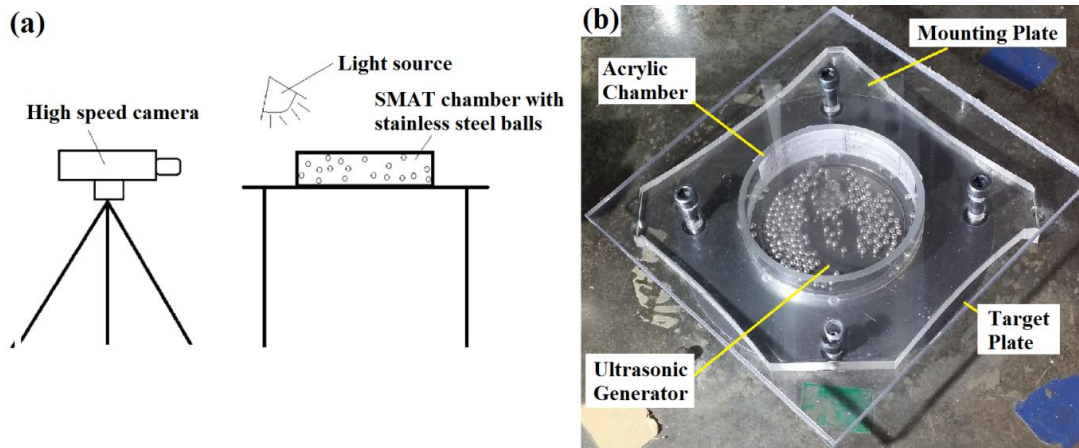


Figure 3.3 (a) Experimental setup of image capture of SMAT;

(b) Acrylic transparent chamber

About five thousand images were captured from each 5-second trial. The images were reviewed consecutively to trace the balls' motions and to determine whether one or more balls collided with the chamber ceiling. Figure 3.4 shows three consecutive images captured at 0.011, 0.012, and 0.013 s in a trial with 50 balls. In Figure 3.4(a), balls 1, 2, and 3 were away from the top surface. Figure 3.4(b) was captured 1 ms after ball 1 struck the top surface and balls 2 and 3 were still moving toward the top surface. In Figure 3.4(c), ball 1 rebounded from the top surface. Ball 2 was moving downward, implying that it had struck the top surface between 0.012 s and 0.013 s. Ball 3 hit the

top surface at this instant. Therefore, the number of impacts at a particular moment can be counted by observing these consecutive images.

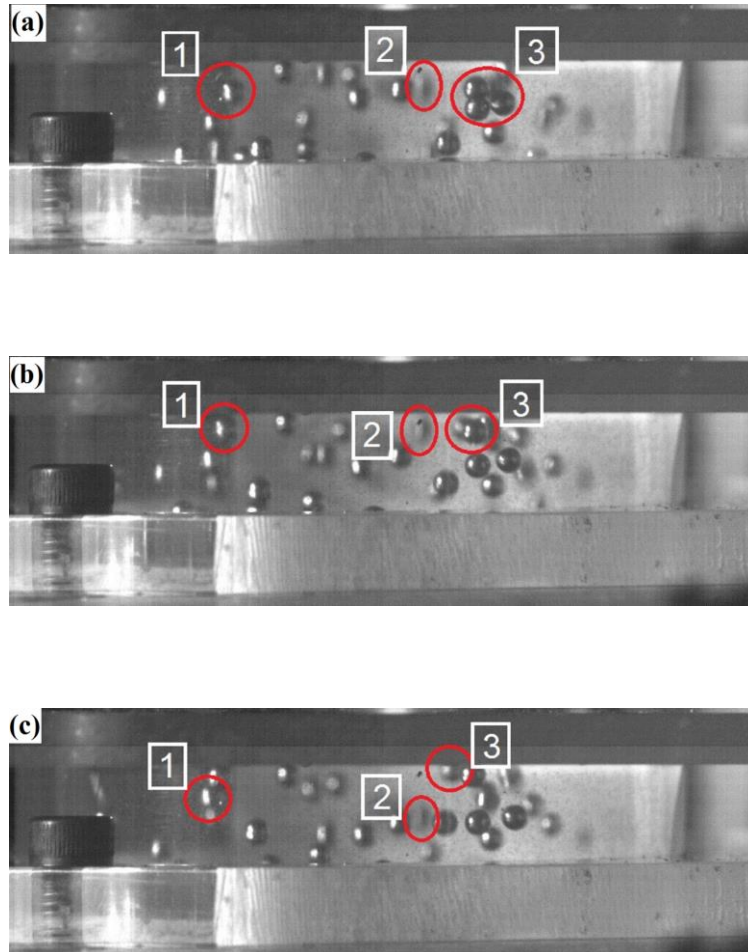


Figure 3.4 Three consecutive images at (a) 0.011s, (b) 0.012s, (c) 0.013s for 50 balls

Five sets of consecutive images in one trial were used to estimate the average number of ball impacts per second to have statistical average. Each set had 10 consecutive images, accounting for a 0.01-s interval. After counting the total number

of impacts visually from the 10 images, the average number of ball impacts per second was then calculated from the average of five sets. As each setting had 3 trials, this counting process was completed three times and took the average number of ball impacts per second. The simulations were conducted under conditions identical to those of the experiments. The experimental and computational results are summarized in Table 3.2, which shows excellent agreement.

Table 3.2 Experimental estimation and simulation prediction of the number of ball impacts in 1s for 50 balls, 100 balls and 200 balls

	50 balls	100 balls	200 balls
Experimental estimation	1360	3020	4880
Simulation prediction (average)	1354	2732	4712

3.5 Effects of Processing Parameters

The mechanical properties of a material after SMAT have long been investigated experimentally, yet little has been done regarding the processing parameters' influence

on SMAT performance. Experimental determination of the number of ball impacts is difficult, but without this knowledge, it is difficult to predict the mechanical properties of a material after SMAT numerically. This is the first time that the number of ball impacts has been determined with the computation model presented above. The effects of various parameters on the number of impacts were studied via simulations. Using seven different numbers of balls, the number of impacts for processing durations of 5, 10, 15, 20 and 25 s were studied. The results are summarized in Figure 3.5. It is confirmed that the number of impacts was proportional to the processing duration.

3.5.1 Prediction of Number of Impacts with Different Number of Balls (n) and Processing Durations

Previous experimental works on SMAT performance have simply used the processing duration for comparison of results. However, for the same processing duration, the mechanical properties after SMAT could differ if any of the influencing parameters, such as the number of balls, was varied. The processing duration was not very useful in providing clear guidelines regarding how SMAT could be carried out to obtain desirable mechanical properties. This problem could be solved if the number of ball

impacts was used to quantify the SMAT performance under different combinations of parameter values.

In this study, the experimental results of SMAT were used to examine the relationship between the number of ball impacts and the processing duration and number of balls. The effect of the number of balls on the number of ball impacts per second was determined by plotting the slope from Figure 3.5 against the number of balls, as shown in Figure 3.6. The number of impacts per second with different numbers of balls was linear to the number of balls, which is given by Equation (3.7)

$$N_{\tau} = d_1 n^2 + d_2 n \quad (3.7)$$

where N_{τ} is the number of impacts per second, and d_1 and d_2 are -0.033 and 30.5, respectively, for the case shown in Figure 3.6.

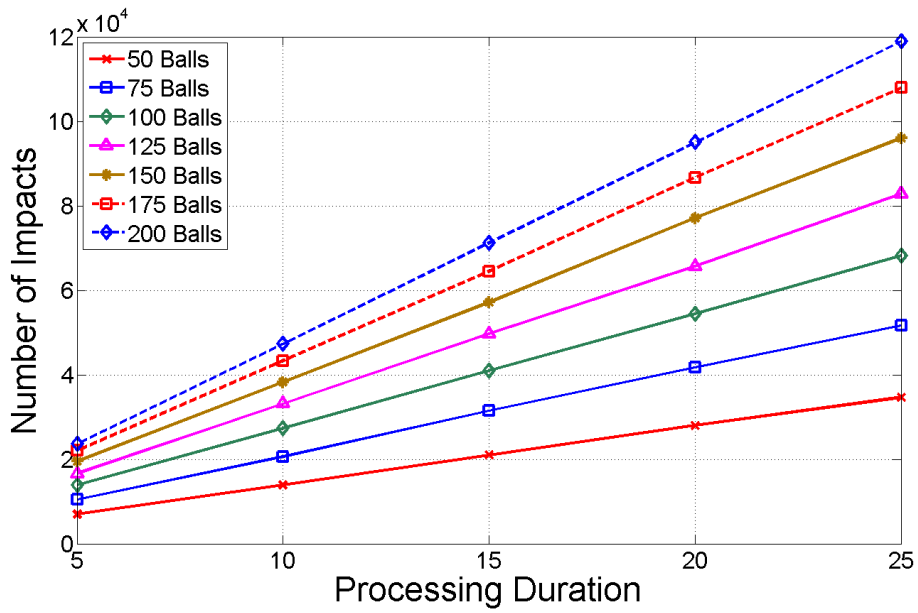


Figure 3.5 Comparison of simulation results of number of ball impacts and duration of different numbers of balls

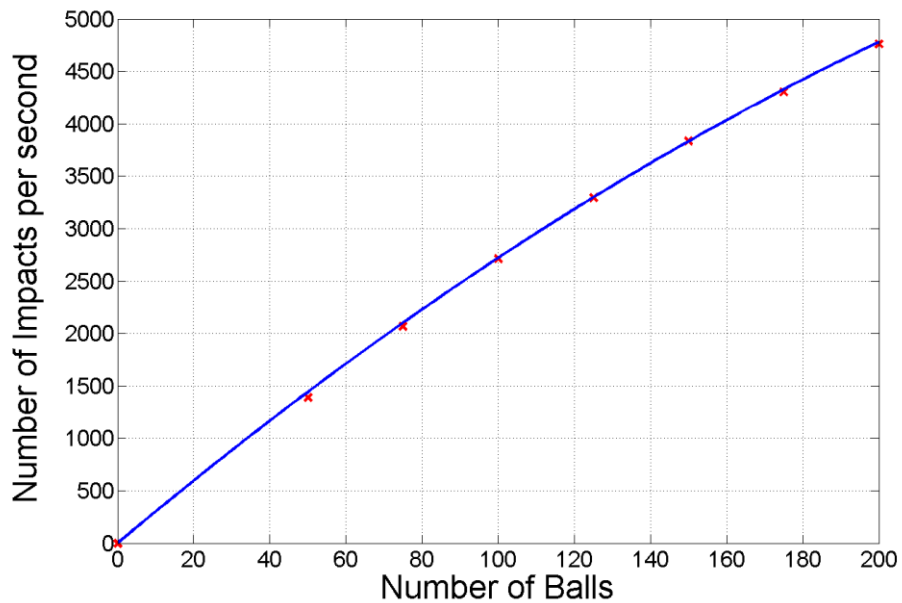


Figure 3.6 Relationship between the number of ball impacts per second and the number of balls in the chamber

3.5.2 Effects of Maximum Ball Velocity, Height and Radius of Chamber

In addition to the number of balls and the processing duration, the number of ball impacts is also a function of the maximum ball velocity after it hits the horn surface.

As shown in Figure 3.7 for the case with 100 balls, the number of impacts in a second increases with the balls' velocity. However, such an increase is nonlinear because of the constraints of the chamber's dimensions. Faster movement of the balls also brings about a greater probability of ball-ball and ball-boundary collisions.

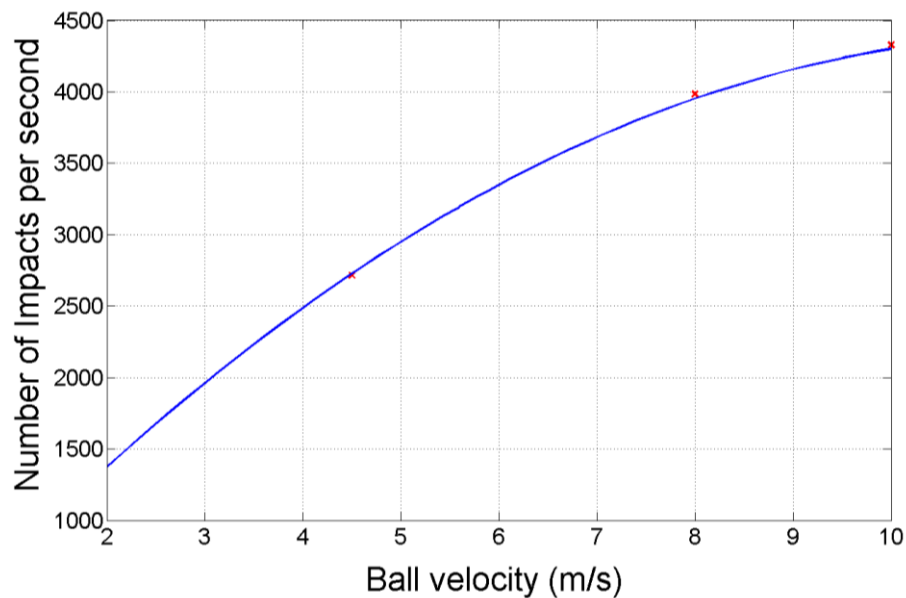


Figure 3.7 Relationship between the number of ball impacts per second and the maximum ball velocity for 100 balls

Further investigation of the combined effects of ball velocity and ball number was conducted with a constant number of ball impacts per second (N_{τ}). As shown in Figure 3.8, the increase in the maximum ball velocity is associated with the decrease in the number of balls when the number of ball impacts is maintained. However, due to the limitations of the chamber's dimensions, a greater maximum ball velocity (v) leads to more ball-ball and/or ball-boundary collisions, and an insignificant reduction in the number of balls (n). The relationship between the number of balls and the ball velocity could be obtained as Equation (3.8).

$$\frac{1}{n} = a_1 v + a_2 \quad (3.8)$$

where a_1 and a_2 are 0.016 and 0.012 respectively.

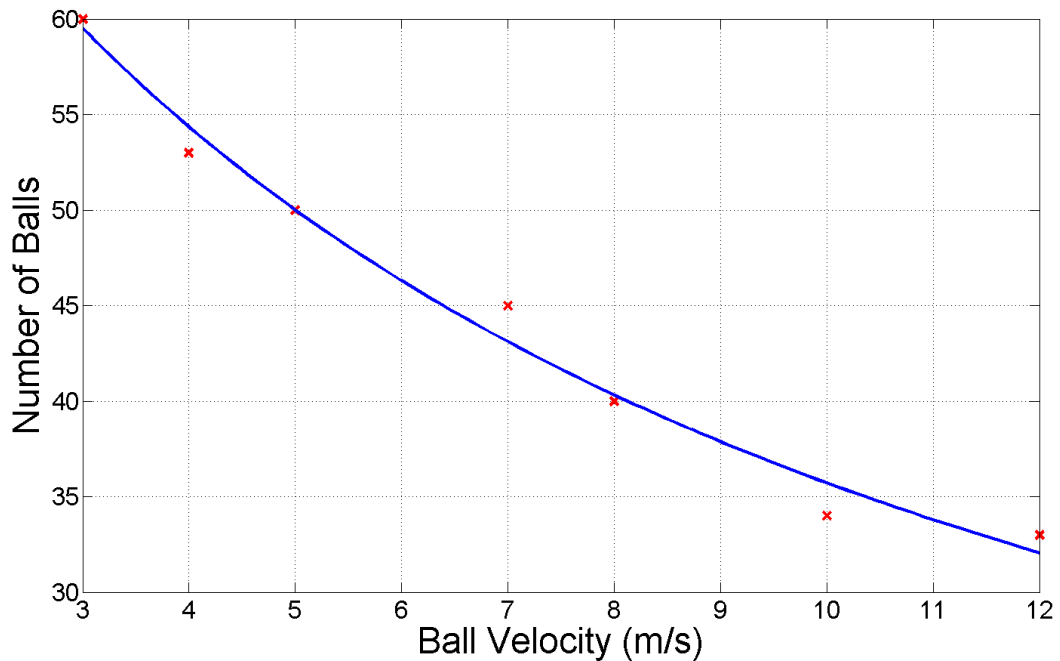


Figure 3.8 Inversely relationship between the number of balls and the maximum ball velocity

The height of the chamber also affects the number of impacts. It is predicted that an increase in the height of the chamber would lead to a reduction in the number of balls (n) if the total number of ball impacts (N), the processing duration (τ), and the maximum ball velocity (v) remain unchanged. When the height of the chamber increases, the number of balls must be increased to keep the same number of impacts. As shown in Figure 3.9, the relationship between the height of the chamber (h) and the number of balls is nonlinearly dependent for a given $N\tau$. The change in the height

of the chamber could be compensated by adjusting the number of balls in Equation (3.9).

$$n = \frac{h^2}{b_1} + \frac{h}{b_2} + b_3 \quad (3.9)$$

where b_1 , b_2 , and b_3 are 39.4, 1.12, and 24.5, respectively.

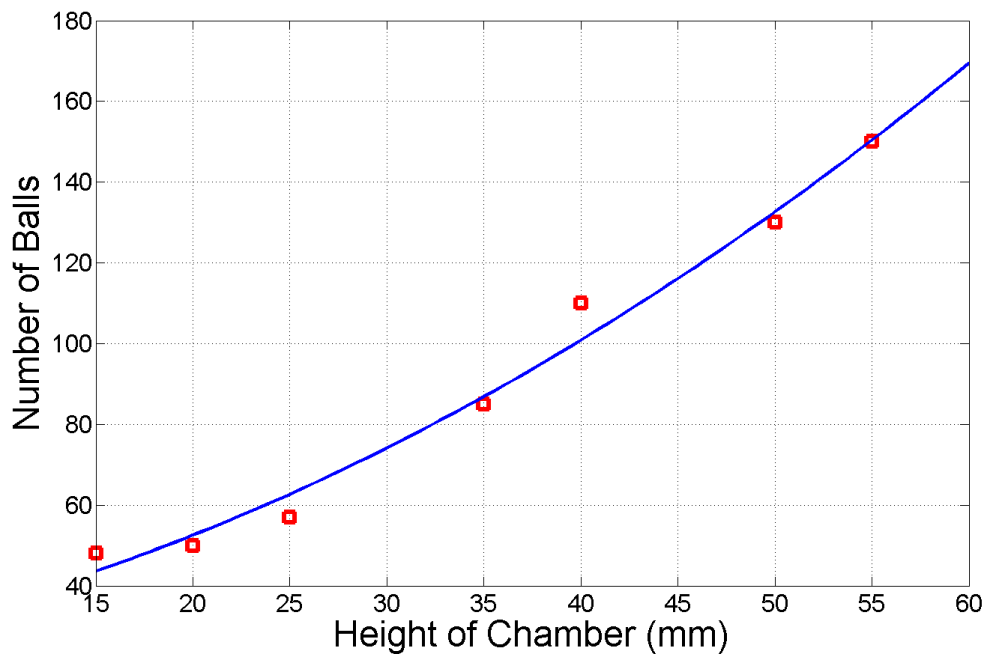


Figure 3.9 Relationship between the height of chamber and the number of balls

We also found that a change in the radius of chamber (R) resulted in an insignificant change in the number of balls needed to maintain a constant N_τ , which is summarized in Table 3.3. When the height of chamber was maintained at 20 mm and

the number of ball impacts was kept constant, changing the radius of the chamber from 28 to 70 mm does not require a notable change of the number of balls.

The number of ball impacts may be predicted with the use of the Equations (3.7) through (3.9). Furthermore, the simulation model demonstrated here is a tool to determine the impact position and velocity for further simulation of the enhancement of mechanical properties.

Table 3.3 Relationship between the radius of chamber (R) and the number of balls (n)

Radius of chamber (R) (mm)	28	35	42	50.4	63	70
Number of balls (n)	53	50	53	54	54	56

3.6 Summary

Different parameters of SMAT affect its results. The model presented here can be used to predict the number of impacts after SMAT. The vibration of the horns and balls'

flying motions in the chamber were modelled with a mathematical equation. With these computational simulations, the following results were observed:

- i). The number of ball impacts was related to the number of balls, the processing duration, and the ball velocity, that is, the vibration frequency of the ultrasonic horn, which could be predicted by a mathematical model.
- ii). The number of ball impacts was directly proportional to the processing duration of SMAT and to the number of balls.

This section forms a bridge between the processing duration and the number of ball impacts under the SMAT process. This is significant in further predictions of flow stress after random ball impacts with the use of the recorded impact position and velocity for each ball on every impact.

CHAPTER 4 - THEORY ON CONSTITUTIVE MODELING

4.1 Introduction

The calculation of the residual stress and strain in various manufacturing processes has long been a hot topic. Lots of experiments were conducted to investigate the mechanical properties of varying parameters with SMAT. However, lacks of research studied on the prediction of stresses with SMAT. Some studies just focused on how would mechanical properties be affected by the macroscopic or microscopic parametric change to the material. Few studies have been conducted to consider the effects of the macroscopic and microstructure evolution together of mechanical property. This combination factors are important especially in SMAT process. A high ball velocity of impact to the target material instantaneously caused the microstructure evolution, the grain refinement and/or the twin development, and the force acting on the material together. This chapter is going to discuss how a constitutive model predicts the residual stress and the strain under the considerations of the impact force. The microstructure evolution of the material with SMAT process is also discussed here.

In addition to the material equation development, the theory of finite element analysis should be first clarified before conducting a further simulation of the SMAT process, followed by the development of the elasticity and the plasticity equations. After preparing these equations, the finite element model can be developed in ABAQUS.

4.2 Development of Constitutive Equation

The grain size, the twin spacing, the strain and/or the strain rate are the factors affecting the residual stress in the SMAT. To develop a new constitutive model, those factors are now investigating to find out their effect to the residual stress.

4.2.1 Assumptions for the Constitutive Equation

The following assumptions are made.

- 1) The refinement of the grain and the twin spacing are essential as similar to the strain, the strain rate and the homogenous temperature as stated in Johnson-Cook (JC) model in the contribution to yield stress.

The impinging of the dislocations formed a pile-up zone around the twin and the grain boundaries. The twin spacing and the grain boundary, therefore, act as barriers to obstacle the dislocations' motions. Several studies mentioned that both mechanisms were strong barriers to stop the propagation of dislocations (Greulich & Murr, 1979; Kibey, et al., 2007; Li & Soh, 2012). The theoretical model and the experimental investigation elucidated that a finer twin spacing and grain size led to a higher stress level to the material. The influence is as important as the changes of the strain, the strain rate and the homogenous temperature.

- 2) The grain size produced with SMAT is greater than the twin spacing.

The twin formation should be occurred inside the grain. When the twin spacing is continuously developed, it breaks the grains into finer grains. Thus, it is impossible for the twin spacing larger than the grain size.

- 3) The minimum grain size is limited by the twin spacing.

As the grain size cannot be smaller than the twin spacing, the lower limit of the grain size is set to be equal to the twin spacing. By further diminishing of grain size but not the twin size, the minimum grain size can be as the size of the twin

spacing in a cycle of refinement process. A new fine grain would be formed until the refinement process completes.

- 4) The deformation twin can only form at/above a certain strain rate, and the twin spacing formed in the strain hardening process depends on the equivalent plastic strain only.

With the results of various studies (Xiao, et al., 2008; Chan, et al., 2010; Chen, et al., 2011; Li & Soh, 2012), the strain rate affects the twins formation. Twins are only found at a certain level of strain rate. This level differs in various metals. In the increase of the strain rates, the twins thickness also increases. At a high strain rate, the elastic deformation only occurs at a very small strain. Therefore, it is assumed that the twins are formed at a strain hardening process and its size depends on the equivalent plastic strain.

- 5) The effect of the grain size of flow stress follows the Hall-Petch relation.

When the strain rate is lower than the twins triggered level, only the grain refinement is occurred in the contribution of flow stress. In the Hall-Petch relation, the stress was affected by the grain size. As reported by other studies (Schiøtz, et

al., 1997; Pande, et al., 2004; Marchenko & Zhang, 2012), the stress was in an inverse relationship with the grain size even in nanocrystalline materials.

- 6) The metal should be under a small deformation.

It is assumed that the metal is under a small deformation so that the strain gradient can be approximately as in a linear relationship. Thus, the total strain is a linear summation of elastic and plastic strain. The flow rule can be applied in the metal plasticity.

4.2.2 Modification of Johnson-Cook Model

The JC model is the constitutive equation used to calculate the flow stress. However, the original model only related the strain, the strain rate and the homogenous temperature to the flow stress of the materials without considering the effect of microstructure evolution. In this section, the detailed modifications of the original JC model is presented in relation to the evolution of the grain and the twin spacing.

4.2.2.1 Johnson-Cook (JC) Model

In the JC model, the flow stress is expressed as a function of the strain, the strain rate $\dot{\epsilon}^*$ and the homologous temperature T^{*m} as presented (Grujicic, et al., 2012; He, et al., 2013; Wang & Shi, 2013).

$$\sigma_f = (A + B \epsilon^n)(1 + C \ln \dot{\epsilon}^*)(1 - T^{*m}) \quad (4.1)$$

where A, B, C, m and n are material constants. The homologous temperature is given by $T^{*m} = \frac{(T-T_0)}{(T_m-T_0)}$, where T_0 is the reference temperature and T_m is the melting temperature.

Since the flow stress is a function of the strain, the JC equation represents the plastic deformation induced by the strain hardening. If the effect of the material response is mainly determined by the term $(A + B \epsilon^n)$, that is, the flow stress is expressed in terms of the yield stress and the strain hardening, where the strain rate and the homologous temperature are no significant effect on it (Ruan, et al., 2010a). The material constant, A, can then be determined as a static yield stress before the strain hardening occurs, that is, $A = \sigma_y$. The parameter A in the JC model represents the static yield stress in the elastic response. If the material is under a continuous hardening process, parameter A is no longer as a constant. The parameter A varies with the material response in the growth of dislocations. In this condition, the yield

stress depends on the microstructure evolution and the changing in the strain. Thus, the flow stress can relate to the change of microstructure and macrostructure as well.

4.2.2.2 Yield Stress (σ_y)

The yield stress σ_y increases in the increase of dislocation density in the strain hardening (Taylor, 1934a; Taylor, 1934b; Mecking & Kocks, 1981). An effort is made to determine the relationship between the microstructure parameters, for instance the dislocation density, to the apparent yield stress as

$$\sigma_y = \alpha G b \sqrt{\rho_I + \rho_{GB} + \rho_{TB}} \quad (4.2)$$

where ρ_I , ρ_{GB} , and ρ_{TB} refer to the dislocation densities inside a grain, at a grain boundary and at a twin boundary, respectively; G is the shear modulus; b is the Burgers vector; α is a geometric constant.

The dislocation densities in the grain boundary and the twin boundary are assumed much greater than that inside the grain. The total dislocation density can be approximated as

$$\sigma_y = \alpha G b \sqrt{\rho_{GB} + \rho_{TB}} \quad (4.3)$$

4.2.2.2.1 Dislocation Density in Twin Boundary (ρ_{TB})

The formation of the deformation twins and the refinement of grains occur over certain level of strain rate for different materials during SMAT. It is assumed that there is a twin boundary dislocation pile-up zone (TBDPZ) at the twin boundary (Zhu, et al., 2011). A high density of dislocations concentrates at this very thin layer. The phenomena are illustrated in Figure 4.1.

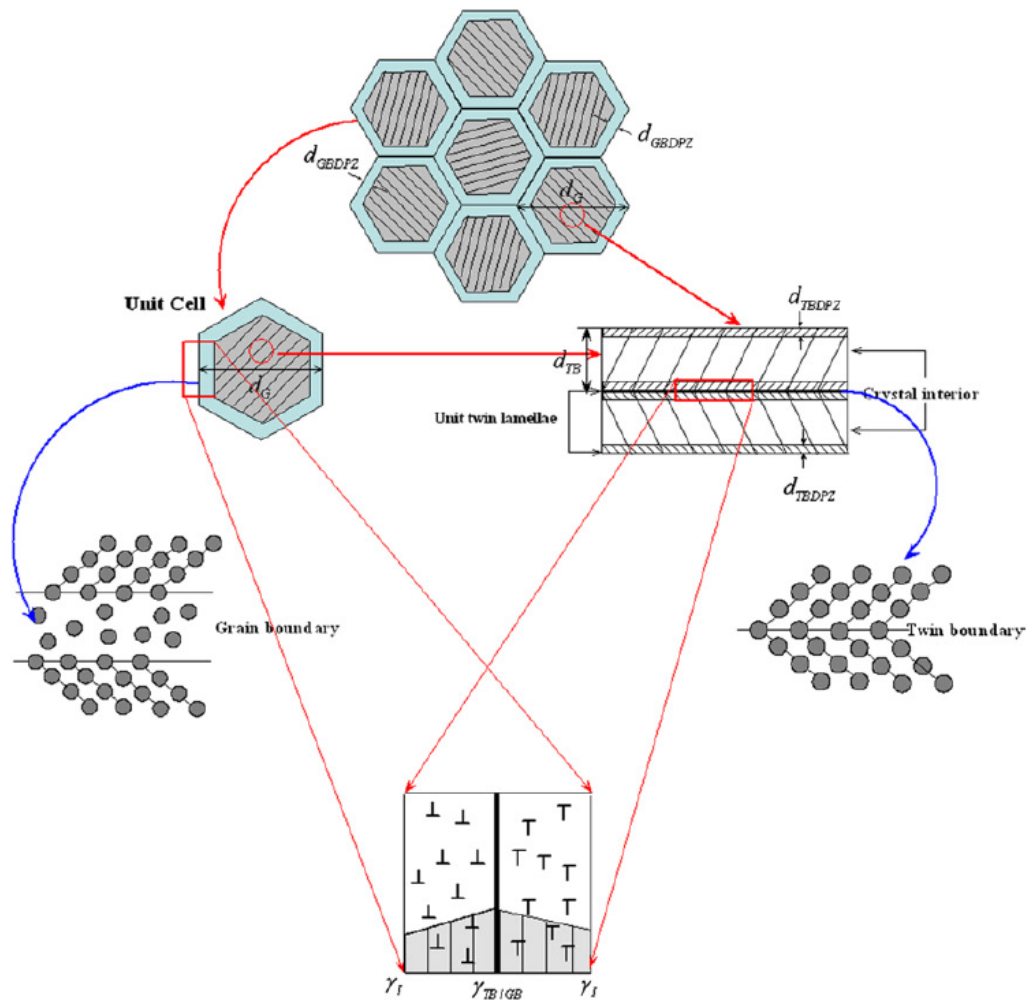


Figure 4.1 Illustration of grain and twin boundaries (Zhu, et al., 2011)

The dislocation density at the TBDPZ is affected by the effective local strain gradient in the TBDPZ as

$$\rho_{TB} = k^{TB} \frac{\tilde{\eta}^{TB}}{b} \quad (4.4)$$

where ρ_{TB} is the dislocation density in the Twin Boundary Dislocation Pile-up Zone (TBDPZ). b is the Burger's Vector. $\tilde{\eta}^{TB}$ is the effective local strain gradient in the TBDPZ; and k^{TB} is a constant to be determined by the following equations.

	d_{TBDPZ}	Thickness of TBDPZ	
$k^{TB} = \frac{12d_{TBDPZ}}{\phi^{TB} \pi d_{TB}}$	d_{TB}	Twin spacing (TB)	(4.4a)
	ϕ^{TB}	Geometric factor	

	$\tilde{\eta}^{TB}$	Effective local strain gradient in the TBDPZ	
$\tilde{\eta}^{TB} = \eta^{TB} - \frac{\eta_p}{d_{TB}}$		Independent parameters of twin spacing	(4.4b)
	η^{TB}		

	ϕ_p	Geometric factor	
$\eta_p = \frac{\sqrt{3} \pi \phi_p b}{12 d_{TBDPZ}}$			(4.4c)

	η_1, η_0	Independent parameters of twin spacing	
$\eta^{TB} = \eta_1 d_{TB} + \eta_0$			(4.4d)

	N_0	A constant, maximum number of inclined dislocations in a grain	
$\eta_1 = \frac{\phi^{TB} N_0 b}{d_{TBDPZ} d_G^2}$			(4.4e)
	d_G	Grain size	

$$\eta_0 = \frac{\phi^{TB} \eta_p' b}{\sqrt{3} d_{TBDPZ} d_G} \quad \eta_p' \quad \text{Number of initial twinning partials in the TBDPZ} \quad (4.4f)$$

$$n_F^{TB} = \frac{N_0}{\chi} \quad \eta_F^{TB} \quad \text{Number of inclined dislocations around the twin boundaries} \quad (4.4g)$$

$$\chi = \frac{d_G}{d_{TB}} \quad \chi \quad \text{Twin density in the grains} \quad (4.4h)$$

By rearranging Equation (4.4), the dislocation density in twin boundary is now related to the twin spacing (d_{TB}) as

$$\rho_{TB} = \left(\frac{12 d_{TBDPZ}}{\phi^{TB} \pi d_{TB}} \right) \left(\eta_1 d_{TB} + \eta_0 - \frac{\eta_p}{d_{TB}} \right) \left(\frac{1}{b} \right) \quad (4.5)$$

where d_{TBDPZ} is the thickness of TBDPZ; ϕ^{TB} and η_p are geometric factors; d_{TB} is the twin spacing; η_1 and η_0 are constants independent of the twin spacing.

This equation agrees with the result in the Hall-Petch relationship, in which the grain reduction increases the yield stress.

4.2.2.2 Dislocation Density in Grain Boundary (ρ_{GB})

The grain boundary dislocation pile-up zone (GBDPZ) is another region containing a high density of dislocations (Zhu et. al., 2011). This region is around the grain boundary as shown in Figure 4.1 and plays an active role in the plastic deformation in the dislocation development. The dislocation density at the GBDPZ can be calculated by

$$\rho_{GB} = \frac{n^{GB}\lambda^{GB}}{V_{cell}} = \frac{6d_{GBDPZ}}{\phi_3 d_G} \quad (4.6)$$

where n^{GB} is the number of dislocations around the GBs, λ^{GB} is the average length of dislocation loops in GBDPZ ($=\pi d_G$), d_G is the grain size. V_{cell} is the volume of the unit cell ($=\pi \frac{d_G^3}{6}$), d_{GBDPZ} is the size of the grain boundary dislocation pile-up zone, ϕ_3 is the geometry constant ranged from 0.5 to 1.5.

4.2.3 Modified Johnson-Cook (JC) Model

Substituting the Equations (4.5) and (4.6) in Equation (4.3), the yield stress triggered by the twin spacing $\sigma_{y(d_{TB})}$ is calculated as:

$$\sigma_{y(d_{TB})} = \alpha G b \sqrt{\left(\frac{12 d_{TBDPZ}}{\phi_{TB} \pi d_{TB}}\right) \left(\frac{1}{b}\right) \left(\eta_1 d_{TB} + \eta_0 - \frac{\eta_p}{d_{TB}}\right) + \frac{6 d_{GBDPZ} n^{GB}}{\phi_3 d_G b}} \quad (4.7)$$

In the study of Chen et al. (2011), a critical strain rate was required for twin formation in stainless steel. When the strain rate was greater than 10^4 s^{-1} , the deformation twins were formed; while, if the strain rate was less than 10^4 s^{-1} , no twin was formed in 304 SS. At a low strain rate, the yield stress was simply determined by the grain size according to the Hall-Petch relationship. The experimental data by other researchers were used to determine the material constants in the Hall-Petch relationship for 304 SS (Schino & Kenny, 2003a & 2003b, Chen, et al., 2011). The yield stress triggered by the grain refinement for 304 SS $\sigma_{y(d_G)}$ is determined as

$$\sigma_{y(d_G)} = 297 + \frac{57}{\sqrt{d_G}} \quad (4.8)$$

The JC equation is finally modified by considering together the twin spacing and the grain refinement at different strain rates.

$$\sigma_f = \begin{cases} [\sigma_{y(d_{TB})} + B(\bar{\epsilon}^P)^n][1 + C \ln \dot{\epsilon}^*][1 - T^{*m}], & \dot{\epsilon} \geq 10^4 \\ [\sigma_{y(d_G)} + B(\bar{\epsilon}^P)^n][1 + C \ln \dot{\epsilon}^*][1 - T^{*m}], & \dot{\epsilon} < 10^4 \end{cases} \quad (4.9)$$

This new constitutive equation shows that the flow stress is not only affected by the equivalent plastic strain and the strain rate, but also the grain size and the twin spacing. The values of those variables in Equations (4.7) and (4.9) are given in Table 4.1.

Table 4.1. Parameters used in the new constitutive equation (Chen, et al., 2011; Zhu, et al., 2011)

α	G	b	d_{TBDPZ}	d_{GBDPZ}	n^{GB}
0.33	86GPa	0.258nm	3.6nm	3.6nm	4×10^6
η_1	η_0	η_p	ϕ^{TB}	ϕ_3	B
3.5×10^{12}	2.975×10^6	0.03675	0.5 - 1.5	0.5 - 1.5	1GPa
n	C	ϵ_0	m	T_0	T_m
0.65	0.07	1.0	1	293K	1500K

4.2.4 Determination of Grain Size and Twin Spacing

The flow stress determined by the new constitutive equation is now related to the grain size and/or the twin spacing, which depends on the strain rate. The refinement of the grain and the twin spacing depends on the equivalent plastic strain in the hardening process.

4.2.4.1 Grain Size Evolution

In an isotropic hardening process, the grain is redefined with the equivalent plastic strain. The refined grain was determined by the initial grain size and the equivalent plastic strain in Equal Channel Angular Pressing (ECAP) (Kim & Kim, 2010).

However, twin formation was not considered in their model.

Chen, et al. (2011) found that the increase in the equivalent plastic strain could lead to the decrease in the grain size when the strain rate was low. The grain size could be determined by Equation (4.10). The grain size reached the minimum size as 20 nm.

The relationship between the grain size and the equivalent plastic strain is plotted in Figure 4.2.

$$\frac{1}{d_G} = 200 - 199.95 e^{-\frac{5}{3}\bar{\epsilon}^p} \quad (4.10)$$

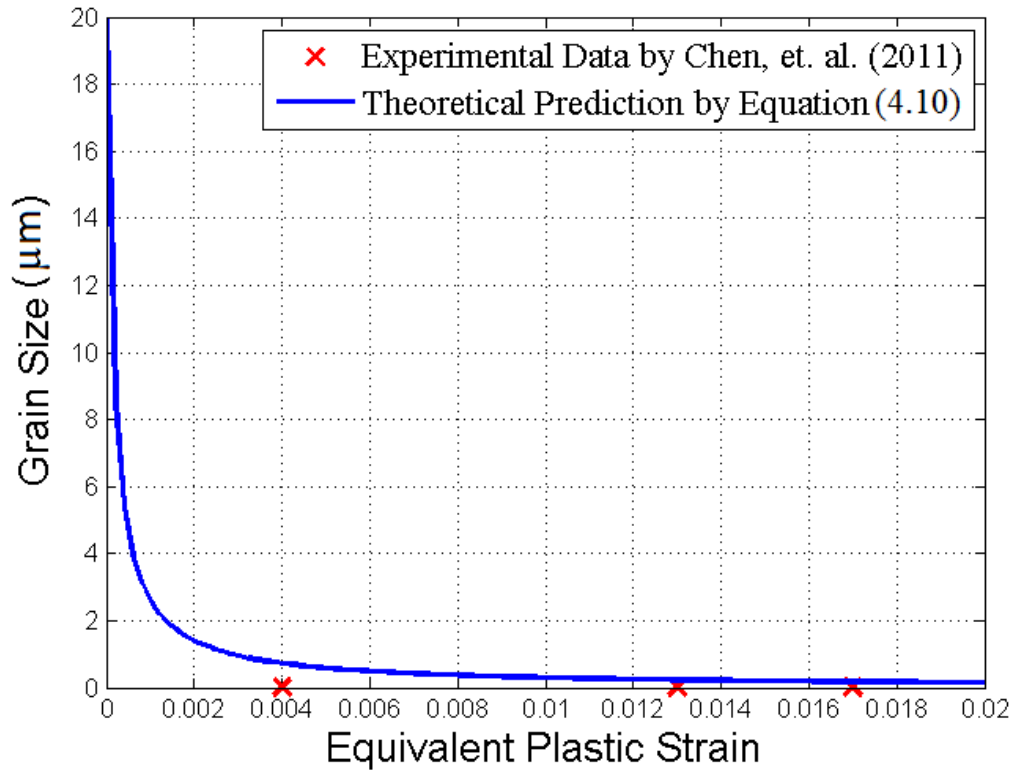


Figure 4.2 Determination of relationship between grain size and equivalent plastic strain

When the strain rate is larger than 10^4s^{-1} , the twins formation become more important in the microstructure evolution. The twins are formed in the grain until the twin spacing equals to the grain size. At this situation, the grain size reduces with the plastic deformation comparable to twin spacing

$$d_G = d_{TB} \quad (4.11)$$

4.2.4.2 Twin Spacing Reduction

Twin spacing is another factor that must be considered in SMAT process. The diminishing of the twin spacing occurs when the strain rate is larger than 10^4 s^{-1} . In this situation, the twin spacing is affected by the equivalent plastic strain. The experiment conducted by Chen et al. (2011) provided the data to determine the mathematical model in Equation (4.12) that is used to calculate the twin spacing. Similar to the grain refinement, the increase in the plastic strain leads to the decrease in the twin spacing. The twin spacing decreases until the grain is split into a smaller grain. The minimum size of the twin spacing is found as 12.5 nm when the plastic strain is about 0.08. By Equations (4.10) and (4.12), the stress is determined by the new constitutive model, Equation (4.9).

$$d_{\text{TB}} = \frac{1}{40e^{(57\bar{\epsilon}^P + 10)}} \quad (4.12)$$

4.3 Validations and Stress Prediction by New Constitutive

Equations

4.3.1 Validation of the New Constitutive Equation

The new constitutive model, Equation (4.9), is now used to predict the flow stress. The simulated results are compared to the experimental results found in other studies (Chan et al., 2010). The twin spacing and the grain size were approximately 10 and 20 nm, respectively found in the literature (Chan et al., 2010). The predicted yield stress is approximately 1.3 GPa, which compares well to the experimental yield stress at 1.2 GPa under the same condition.

4.3.2 Stress Prediction

The flow stress of SS304 is determined by two mechanisms: the grain refinement and the twin spacing, which depends on the strain rate in the strain hardening. The change in the flow stress by these mechanisms are calculated by Equation (4.9) and compared in Figure 4.3 against the strain in the impact (z-) direction in SMAT. The flow stress by the grain refinement increases with the strain monotonically. While the flow stress by the twin spacing and the grain refinement together (blue line) increases to reach a

maximum value and then decreases. Further decrease of the twin spacing can no longer increase in the flow stress.

When the strain is below 0.05, the flow stress by the grain refinement is greater than that by the twin formation; while at a higher strain, the behaviour is reversed. The flow stress reaches the maximum value at 1.33 GPa when the twin formation is in effective with the grain refinement.

Figure 4.4 and 4.5 shows the variations of the flow stress as a function of strain rate. The maximum flow stress is found at 1.46 GPa due to the twin formation at a strain rate of 1×10^5 /s. In SMAT, the balls stroke at a high velocity generated the strain rate as high as 1×10^5 /s. This prediction is consistent to the experimental results conducted by Chan et al. (2010).

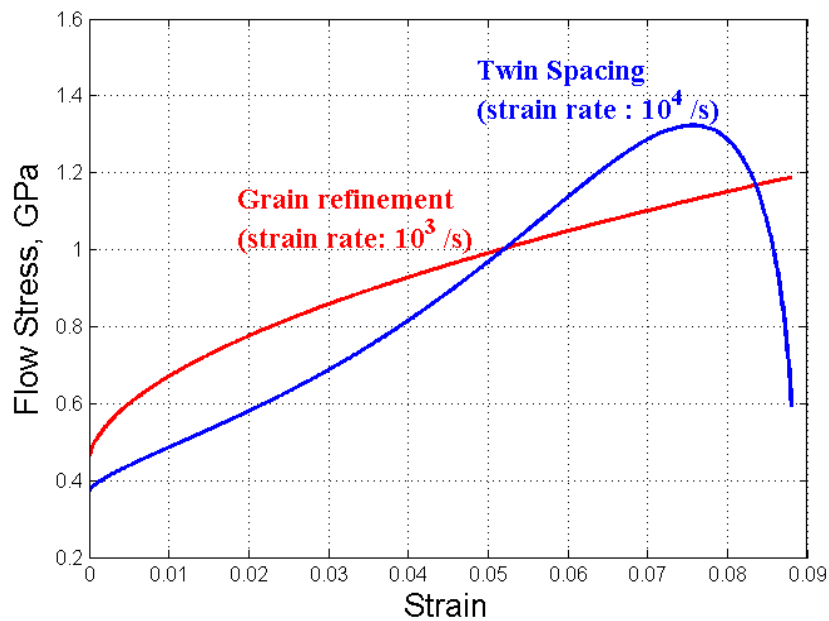


Figure 4.3 Comparison of flow stress dominant by grain refinement and/or twin formation

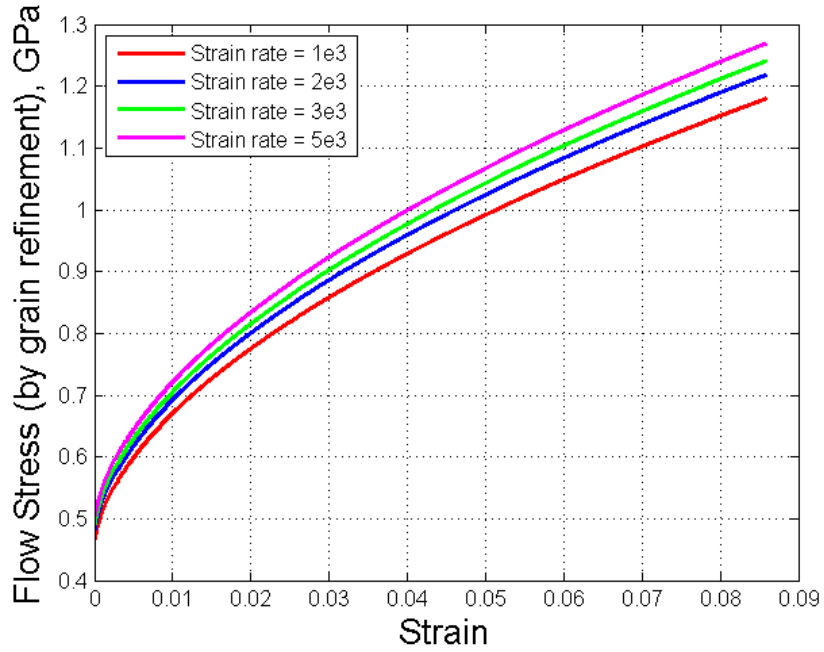


Figure 4.4 Relationship between flow stress due to grain refinement and strain at different strain rates

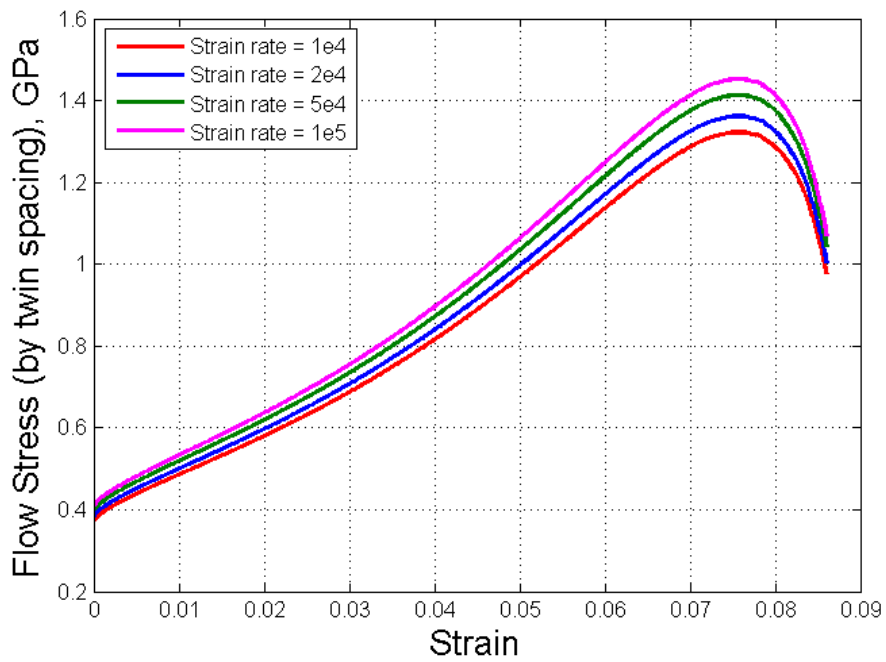


Figure 4.5 Relationship between flow stress due to twin spacing and strain at different strain rates

4.4 Stress Integration of Metal Plasticity

In the previous sections, the new constitutive model is developed in Equations (4.9), (4.10), and (4.12) to update the evolution of the grain size and the twin spacing. FEA is implemented with a new constitutive model as a material law to simulate the SMAT. The flow stress on the target metal is predicted after a number of random and in multi-directional ball impacts. The dynamics forces and the metal behaviour must not be the same at every impact. The stress level of the targeting metal depended on either elastic or plastic deformation critically.

Before conducting the simulation by FEA in next chapter, the governing equations of the elasticity and plasticity behaviours of metal should be defined clearly to update of the plastic stress and the plastic strain at every time increment.

4.4.1 Basic Components of Elastoplastic Model

As introduced in the above sections, the constitutive model was applied to determine the stress induced by the twin spacing and the grain refinement by the metal plasticity.

The elastic and plastic behaviours of the metal are determined by the general components (Chen, 1994; Wu, 2005; Neto, et al., 2008):

1. Summation of strain tensor by elastic $(\cdot)^e$ and plastic $(\cdot)^p$ components.

$$\boldsymbol{\varepsilon} = \boldsymbol{\varepsilon}^e + \bar{\boldsymbol{\varepsilon}}^p \quad (4.13)$$

2. Free-energy function by all hardening components.
3. Constitutive equation for the flow stress and the hardening thermodynamic force,
A.
4. Yield function.
5. Plastic flow rule and the hardening law.
6. Loading and/or unloading criterion.

The general steps in the calculation of stress integration are by the elastic and plastic predictor.

4.4.2 Elastic Predictor

The constitutive model is assumed as J_2 plasticity with isotropic hardening. In the elastic response, the increment of equivalent plastic strain is zero, $\Delta \bar{\epsilon}^p = 0$. The elastic trial strain (ϵ_{t+1}^{e*}) and trial accumulated plastic strain ($\bar{\epsilon}_{t+1}^{p*}$) are updated by

$$\epsilon_{(t+1)}^{e*} = \epsilon_{(t)}^e + \Delta \epsilon \quad (4.14)$$

$$\bar{\epsilon}_{(t+1)}^{p*} = \bar{\epsilon}_{(t)}^p \quad (4.15)$$

where $\Delta \epsilon$ is the strain increment corresponding to a typical time increment $[t_t, t_{t+1}]$.

Because there is no plastic strain in the elastic deformation, the trial total strain equals to the elastic strain. The corresponding trial stress, \mathbf{s}_{n+1}^* , is then computed as

$$\mathbf{s}_{(t+1)}^* = 2\mathbf{G} \epsilon_{d(t+1)}^{e*} \quad (4.16)$$

and

$$\mathbf{p}_{(t+1)}^* = \mathbf{K} \epsilon_{v(t+1)}^{e*} \quad (4.17)$$

Denote $q(\mathbf{s}) = \sqrt{3}J_2(\mathbf{s})$

$$\mathbf{q}_{(n+1)}^* = \sqrt{\frac{3}{2} \mathbf{s}_{(n+1)}^* : \mathbf{s}_{(n+1)}^*} \quad (4.18)$$

where the notation $(\cdot)^*$ refers to the trial value; the subscripts e and p denote as the elastic and p lastic system; \mathbf{s} and p refer to the deviatoric and hydrostatic stresses; $\boldsymbol{\varepsilon}_d$ and $\boldsymbol{\varepsilon}_v$ denote the deviatoric and volumetric strain; $\boldsymbol{\varepsilon}$ is strain tensor; ε_v is a sum of ε_{11} , ε_{22} and ε_{33} ; G and K are the shear and bulk modulus respectively.

The calculated trial stress, $\sigma_{(\cdot)}$, is compared with the yield function, $\Phi(\boldsymbol{\sigma}, \sigma_f)$, in the following conditions. If the yield criteria ε is inside of the trial yield surface, σ_f , the flow stress is calculated by the constitutive Equation (4.9).

$$\Phi(\boldsymbol{\sigma}, \sigma_f) = \sqrt{3 J_2(\mathbf{s}_{n+1})} - \sigma_f < 0 \quad (4.19)$$

The process is purely elastic.

The elastic trial states are updated by

$$\boldsymbol{\varepsilon}_{(n+1)}^e = \boldsymbol{\varepsilon}_{(n+1)}^{e*} \quad (4.20)$$

$$\mathbf{s}_{(n+1)} = \mathbf{s}_{(n+1)}^* \quad (4.21)$$

$$\bar{\boldsymbol{\varepsilon}}_{(n+1)}^p = \bar{\boldsymbol{\varepsilon}}_{(n+1)}^{p*} = \bar{\boldsymbol{\varepsilon}}_{(n)}^p \quad (4.22)$$

4.4.3 Plastic Predictor

When the yield criteria Φ^* is outside the yield surface, i.e.

$$\Phi(\boldsymbol{\sigma}, \sigma_f) = \sqrt{3 J_2(\mathbf{s}_{n+1})} - \sigma_f \geq 0 \quad (4.23)$$

the material is under the plastic deformation and the yield function should be updated by the associated flow rule

$$\boldsymbol{\varepsilon}_{(n+1)}^e * = \boldsymbol{\varepsilon}_{(n+1)}^e * + \Delta \bar{\boldsymbol{\varepsilon}}^p \sqrt{\frac{3}{2}} \frac{\mathbf{s}_{(n+1)}}{\|\mathbf{s}_{(n+1)}\|} \quad (4.24)$$

$$\bar{\boldsymbol{\varepsilon}}_{(n+1)}^p * = \bar{\boldsymbol{\varepsilon}}_{(n)}^p + \Delta \bar{\boldsymbol{\varepsilon}}^p \quad (4.25)$$

$$\Phi^* = \sqrt{3} J_2(\mathbf{s}_{n+1}) - \sigma_f(\bar{\boldsymbol{\varepsilon}}_{(n+1)}^p) = 0 \quad (4.26)$$

Because the initial static yield stress σ_y is a function of the equivalent plastic strain and the twin spacing, and/or the grain size by Equation (4.7), or (4.8), respectively, the yield criteria is updated by Equation (4.9). The associative hardening rule is given by

$$\dot{\bar{\boldsymbol{\varepsilon}}}^p = \sqrt{\frac{2}{3}} \|\dot{\bar{\boldsymbol{\varepsilon}}}^p\| \quad (4.27)$$

After considering the hardening effect, the incremental plastic multiplier is solved by Newton-Raphson method.

$$\Phi^*(\Delta \bar{\boldsymbol{\varepsilon}}^p) \equiv \mathbf{q}_{(n+1)}^* - 3\mathbf{G}(\Delta \bar{\boldsymbol{\varepsilon}}^p) - [\sigma_y(\bar{\boldsymbol{\varepsilon}}^p + \Delta \bar{\boldsymbol{\varepsilon}}^p)] = 0 \quad (4.28)$$

The plastic strain can be updated as

$$\bar{\boldsymbol{\varepsilon}}_{(n+1)}^p = \bar{\boldsymbol{\varepsilon}}_{(n)}^p + \Delta \bar{\boldsymbol{\varepsilon}}^p \quad (4.29)$$

The plastic stress is finally updated by

$$\mathbf{s}_{n+1} = \left(\mathbf{1} - \frac{3G \Delta \bar{\epsilon}^p}{\bar{\epsilon}^p_{(n+1)}} \right) \mathbf{s}_{n+1}^* \quad (4.30)$$

4.5 Summary

In SMAT, numerous impacts on the material surface caused the plastic deformation and the microstructure evolution. The development of the constitutive equation was considered both the macroscopic and microscopic changes to calculate the flow stress by a modified Johnson-Cook model. The flow stress related to the strain, the strain rate, the homogenous temperature, together with the grain size and the twin spacing in the presence of the deformation twins. The predictions by this new constitutive model of flow stress were compared to the experimental results for 304 SS. The range of the flow stresses in two cases, by the grain refinement alone and/or the twin spacing together, were predicted by the new constitutive equation. In the presence of deformation twins and the grain refinement, the flow stress was 1.33 GPa; while it was 1.13 GPa in the case by the grain refinement only at the same strain level. Because the incident angle and the velocities of ball affected the energy transmission to the

metal in SMAT, the strain rate of the metal in the impact could be as high as 1×10^5 /s.

This resulted at a high flow stress induced by the twin formation. It was predicted that the maximum flow stress could reach at 1.46 GPa for 304 SS.

The implementation of the constitutive model with the metal plasticity calculation replaced the conventional material law used in the commercial FEM software. With the aid of the user-defined subroutine, the constitutive model with metal plasticity replaced the conventional material law to predict the mechanical properties with SMAT. The iterations of the equivalent plastic stress and the strain were also considered in this chapter, which were prepared for the development of the user-defined simulation to simulate the SMAT process.

CHAPTER 5 - FINITE ELEMENT ANALYSIS ON SMAT

5.1 Introduction

The previous chapters discussed the modelling of the SMAT process and the constitutive model in the metal plasticity deformation. This chapter focuses on the finite element analysis to predict the stresses in SMAT.

With the aid of common FEA software - ABAQUS, the sequential ball impact is modelled first by the embedded governing material equation. The simulated results are compared with the experimental results found in other studies.

5.2 Simulation of Mechanical Properties after SMAT

The effects of different parameters in SMAT were determined with the aid of the simulation model in Chapter 3. The increase of the processing duration increased the number of ball impacts that could produce nano-grains efficiently. However, when the increase of the processing duration reached to a saturated value, the efficiency of nano-

grain production could decrease because large amount of energy was required to further reduce the grain. FEA was conducted to understand the efficiency and to predict the change of mechanical properties in SMAT process. The impacting velocities and angles of balls affected the mechanical behaviours of the metal sample in SMAT. Thus, the effects of the velocities and impact angles of the balls were investigated first.

The aforementioned MATLAB model in Chapter 3 was verified using 35% power setting of the ultrasound generator. The MATLAB model was used for the same condition as experiment, In the following simulation for multiple impacts, the ultrasonic horn was assumed at 80% power setting to have a ball velocity at 10 m/s. This setting was the same as the experimental setup conducted by Chan et al. (2010).

5.2.1 A Single Ball Normal Impact at Different Velocities

The ball velocity affected the mechanical behaviours of the metal with SMAT. To understand the effects of ball velocity, different ball velocities were applied in the simulation. It is assumed that the ball struck the target metal in the normal direction, where all balls' energies were transferred to the metal at maximum level. Figure 5.1

shows the simulation results at different ball velocities ranging from 4 m/s to 10 m/s. The trends of all curves are similar, which have the highest stresses at the impact surface and further decrease along the depth of the plate. The gradient of the stress change at a certain depth of the plate. In the contour plot in Figure 5.2(a), the colour spreads out from the impact location to the half of the plate's thickness. When the ball velocity increases, more energy can be transmitted to the deeper regions that have a higher stress level as illustrated in Figure 5.2 (b) - (g). The contour plots of the plate by different ball velocities show that the high stress region is found at a circle around the center of impact. The ball rebound causes a second strain deformation that stress further increases. Figure 5.3 plots the stress distribution along the horizontal distance from the impact location. The stress at the center of the impact is lower than the surrounding regions from the center. When the ball velocity during impact is below 5 m/s, the maximum stress regions are at 0.2 mm away from the center of impact. When the ball velocity is slow, the energy penetration is low, which affects the top surface of the metal plate. The stress concentrates on a closer region around the impact center. When the ball velocity is greater than 6 m/s, the maximum stress regions are constantly at 0.3 mm away from the center of impact. A high amount of energy causes deeper

plastic deformation before rebounding at a high impact velocity. The affected regions are then wider.

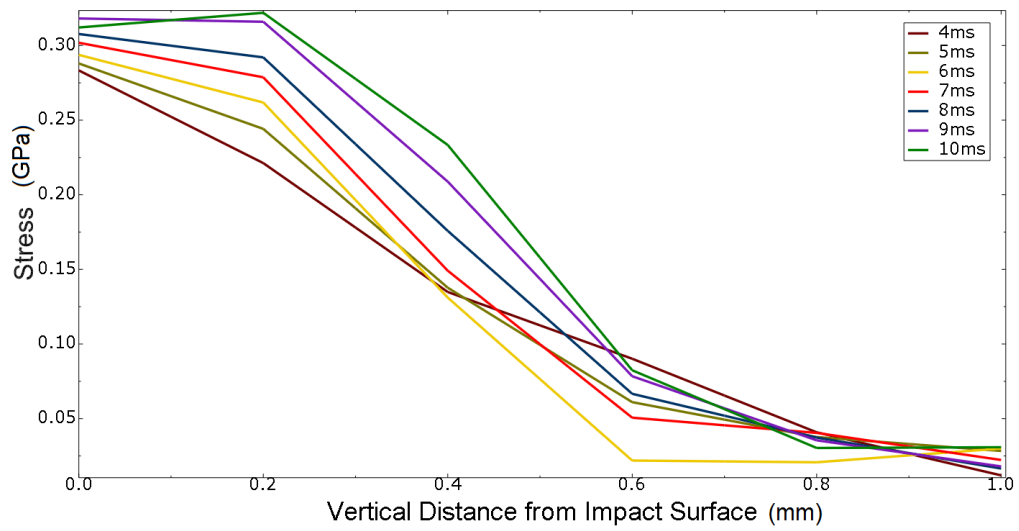


Figure 5.1 Comparison of stresses along the depth of plate at center at different ball velocities

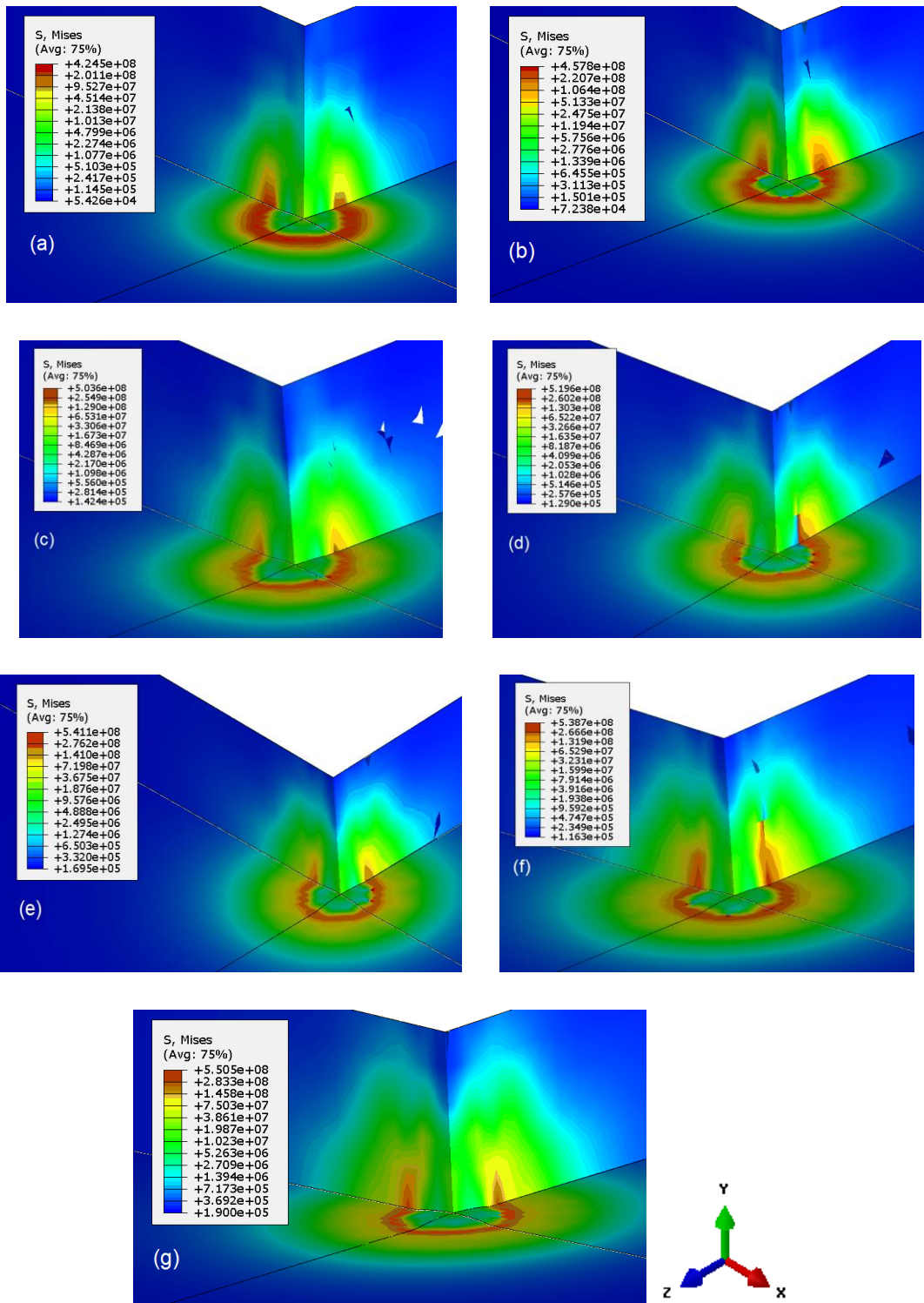


Figure 5.2 Contour plot of stress at different ball velocities at
 (a) 4 m/s; (b) 5 m/s; (c) 6 m/s; (d) 7 m/s; (e) 8 m/s; (f) 9 m/s; (g) 10 m/s

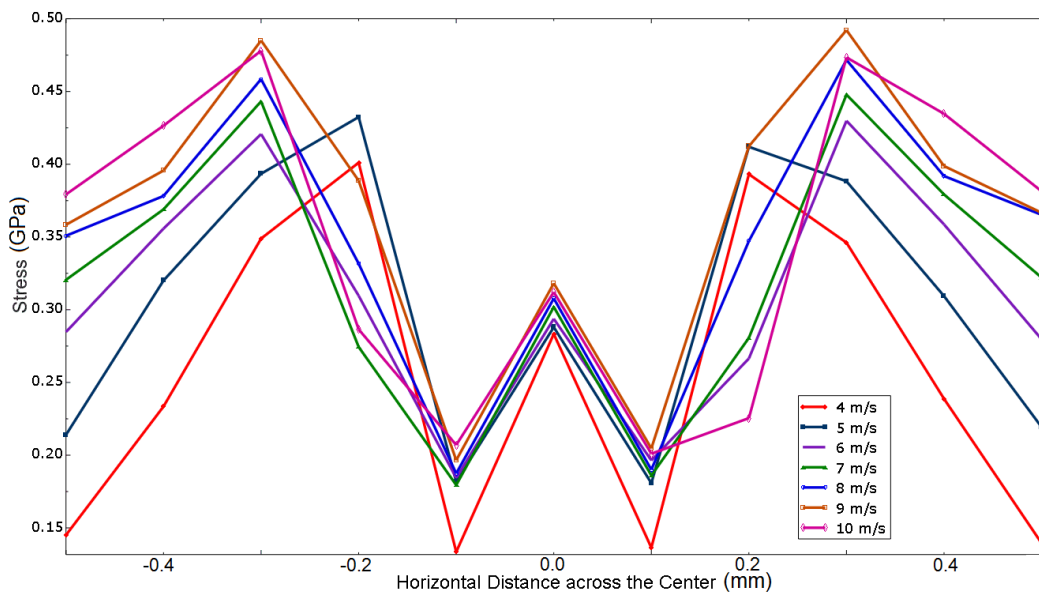


Figure 5.3 Stress on horizontal distance across the center of impact in z-direction

Plastic deformation even occurs the ball impact velocity is at 4 m/s as shown in Figure 5.4. The equivalent plastic strain rate steadily increases with the increase of the ball impact velocity to cause plastic deformation. The strain rate becomes a constant in micro-seconds. The plastic deformation was stopped when the ball starts to rebound. The equivalent plastic strain is then saturated.

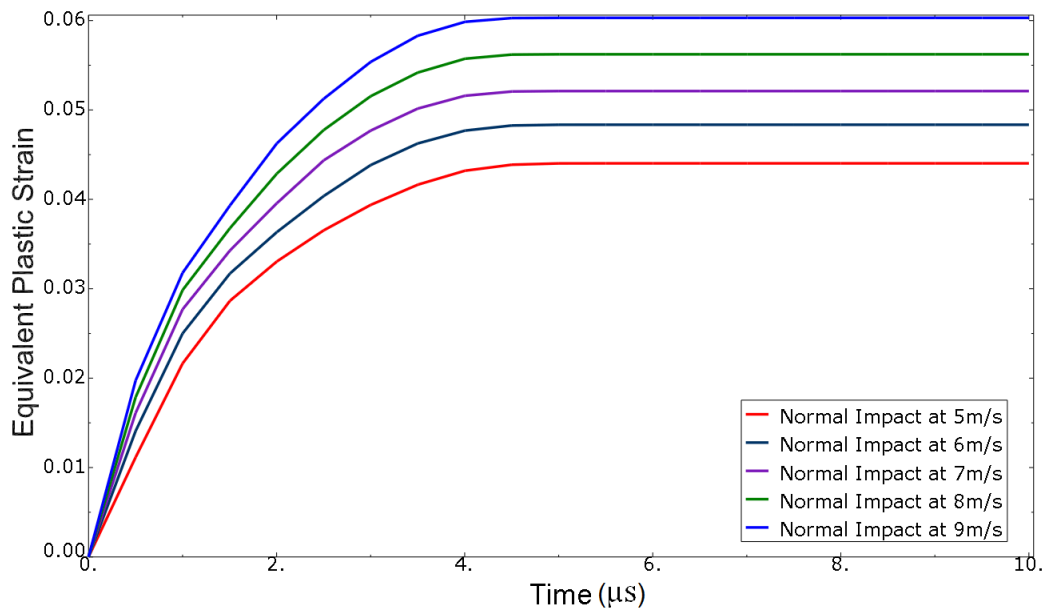


Figure 5.4 Comparison of equivalent plastic strain rate at different ball velocities at the center node

A low impact velocity causes a lower strength and ductility as shown in Figure 5.5. When the ball velocity is at 5 m/s, the stress increases sharply to the yield point at about 63 GPa. The plastic deformation is interrupted as the ball has not sufficient energy for further transmission. The ball velocity at 10 m/s has the greatest stress and strain among the selected ball velocities. Sufficient energy allows the ball causing a greater plastic deformation along the depth of the plate.

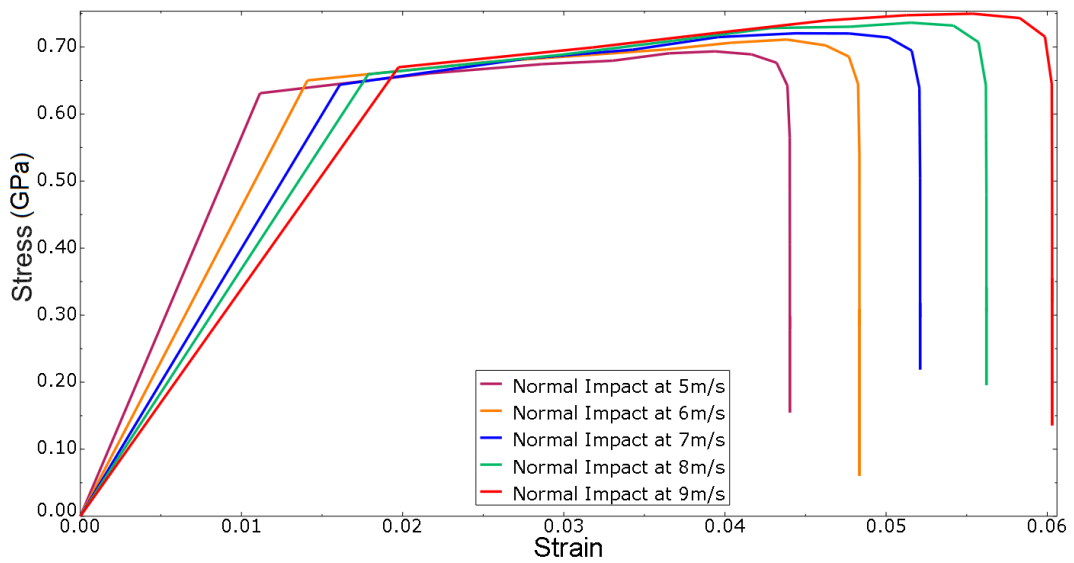


Figure 5.5 Comparison of stress-strain relationship at different ball velocities at center node

5.2.2 A Single Ball Impact at Different Angles

The impact velocity is not a single factor affecting the mechanical properties in SMAT.

The main working principle of SMAT is random ball impacts to achieve an isotropic property. The oblique impact can also affect the results in the plastic deformation of the target metal. Zhang et al. (2011a) introduced that the impact angle affected the residual stress on the plate. However, the relationship between the normal and oblique impacts has not yet investigated. The ball was assumed to strike the metal plate angularly at 10 m/s in this simulation. The vertical velocity was set at different

intervals from 5 m/s to 9 m/s as listed in Table 5.1. The results were compared with the case with normal impact at the same velocity. The incident angle is defined as Figure 5.6 from the normal.

Table 5.1 Velocities set in the angular impact simulation

Impact Velocity at y-direction V_y (m/s)	Impact Velocity at x-direction V_x (m/s)	Angle θ
5	8.66	60°
6	8	53.13°
7	7.14	45.57°
8	6	36.89°
9	4.36	25.84°

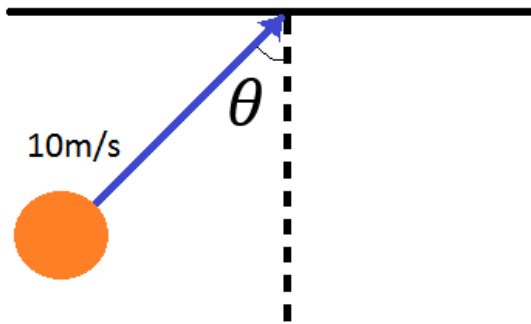


Figure 5.6 Definition of impact angle

The trends of the equivalent plastic strain rate of angular and normal impacts agree at various ball velocities well in Figure 5.7. The equivalent plastic strain rate is generally steady until $4 \mu\text{s}$. The vertical component of the ball velocity affects the stress and the deformation of the target plate. Even though the incident angle and velocity of ball are different in oblique and normal impacts, if the vertical component of ball velocity are the same, the stress distribution achieve the same result. Similar results are also found on the stress-strain relationship in the oblique and normal impacts at different ball velocities. In Figure 5.8 – 5.12, the stress-strain relationship in oblique impacts are matched well compared with that the cases in the normal impact.

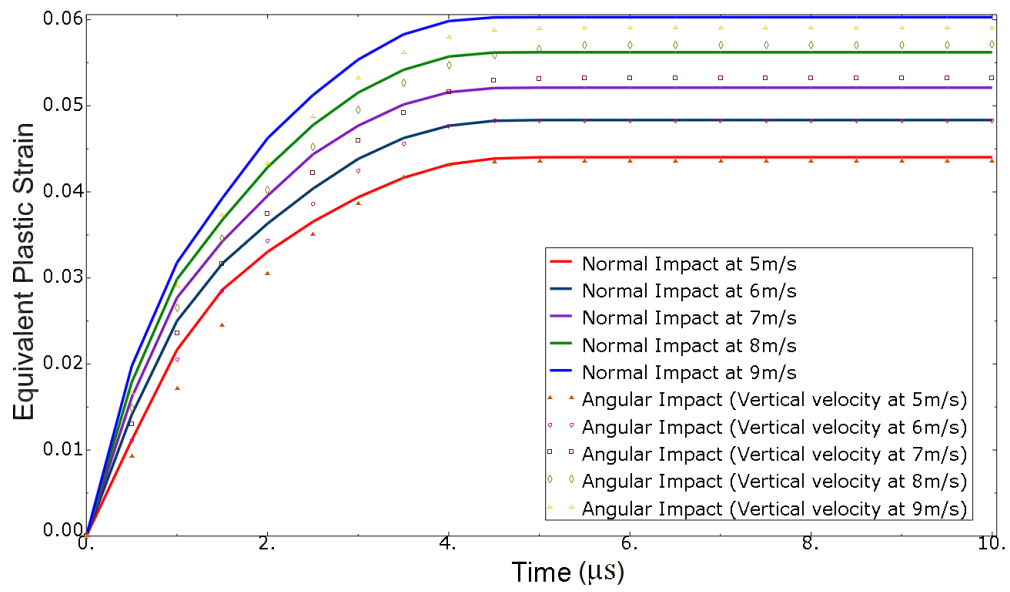


Figure 5.7 Comparison of equivalent plastic strain rate of angular and normal impact at the center node

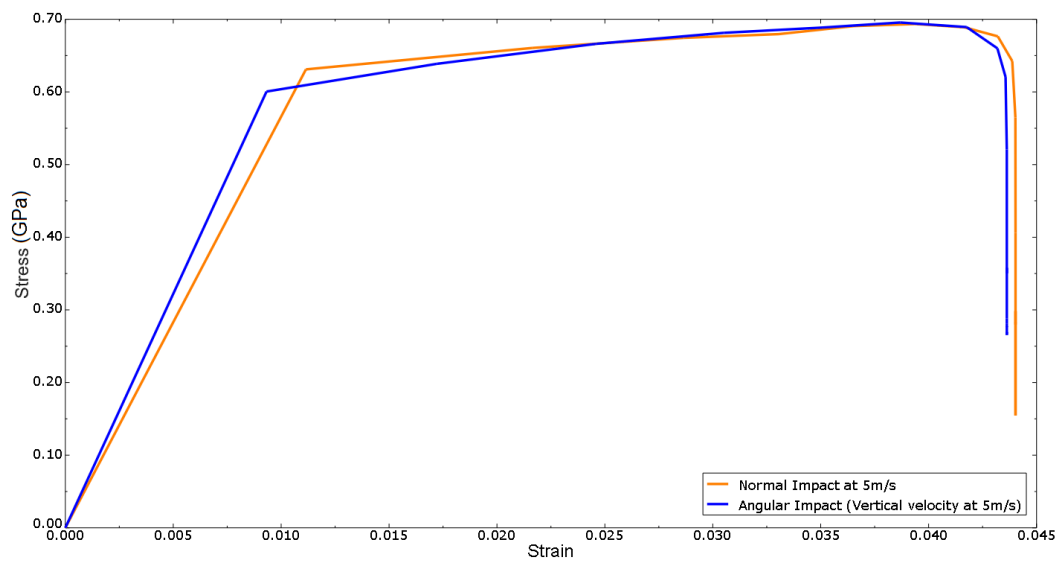


Figure 5.8 Comparison of stress-strain relationship of normal and angular impact at 5 m/s

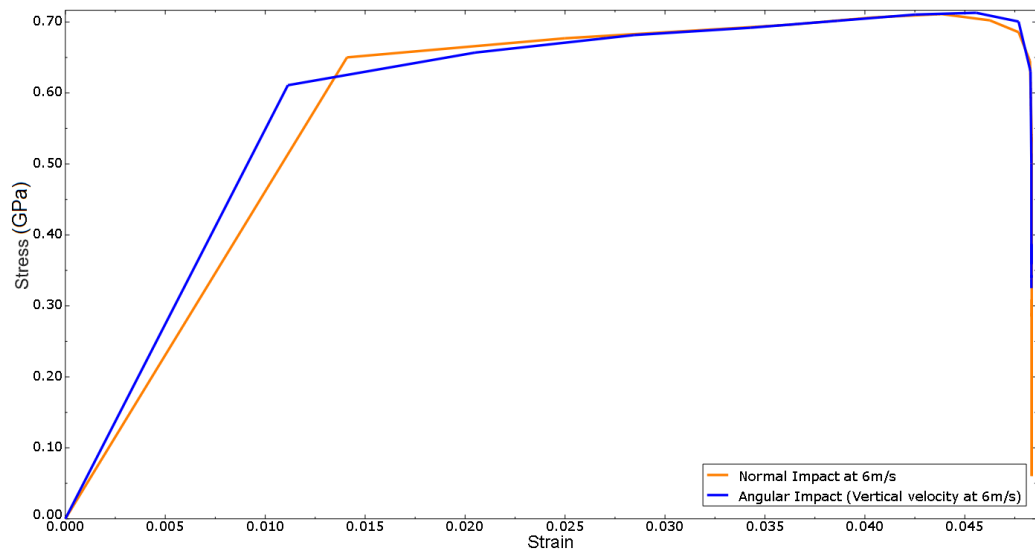


Figure 5.9 Comparison of stress-strain relationship of normal and angular impact at 6 m/s

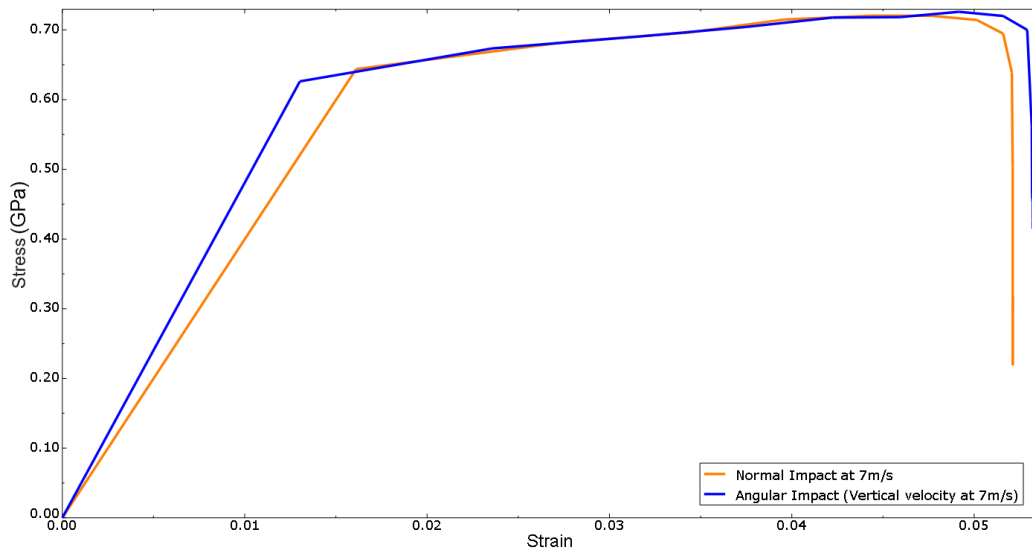


Figure 5.10 Comparison of stress-strain relationship of normal and angular impact at 7 m/s

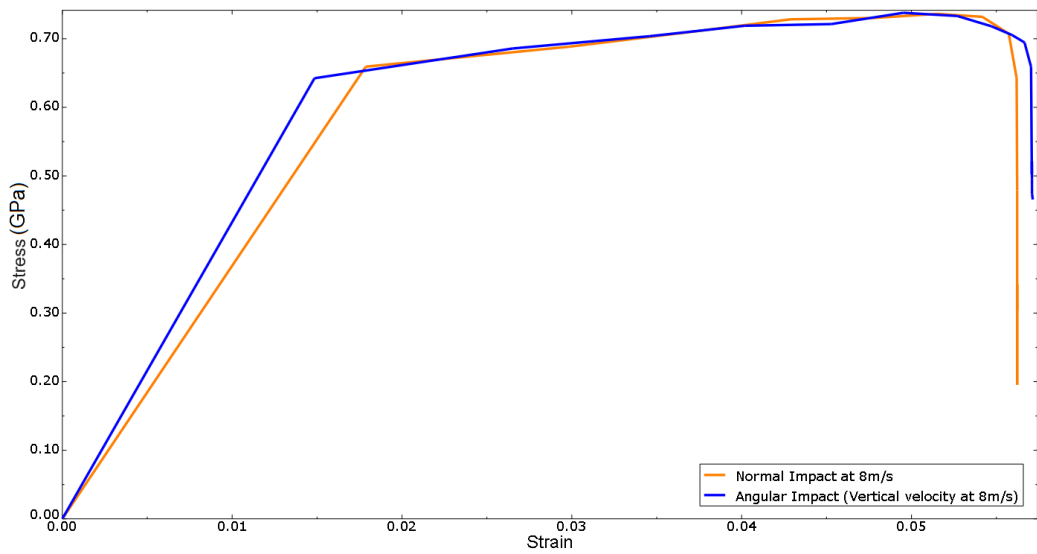


Figure 5.11 Comparison of stress-strain relationship of normal and angular impact at 8 m/s

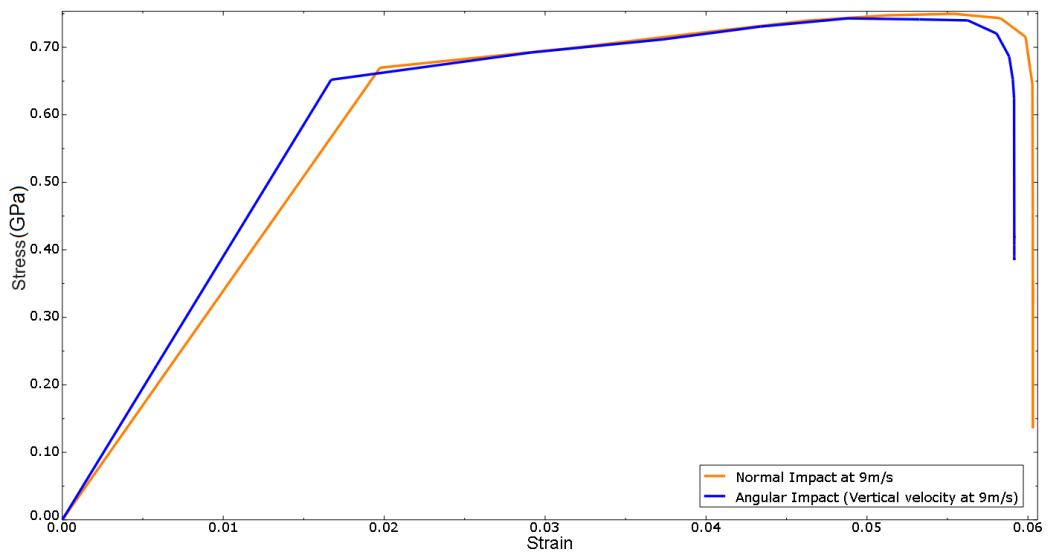


Figure 5.12 Comparison of stress-strain relationship of normal and angular impact at 9 m/s

5.2.3 Simulation of Multiple Impacts

After the simulation of a single impact, multiple impacts were also conducted by ABAQUS. The impact locations and velocities were generated by the MATLAB simulation introduced in Chapter 3 first to simulate the impact in SMAT. The diameter and height of chamber were 70 and 15 mm, respectively. The number of balls in the chamber was 100 and the initial velocity was limited to 10 m/s. The processing duration was set to 10 min. Only the center of balls struck on a specific circle was selected to reduce the computational time. A 3D finite-element model with a plate size of $10 \times 10 \times 1$ mm was created and 27 balls were placed at the corresponding impact positions. The center positions of the 27 balls are plotted in Figure 5.13. The mechanical properties of the plate by the random impacts was then determined by examining a specific area with a 0.2-mm diameter of circle around the center of the target plate.

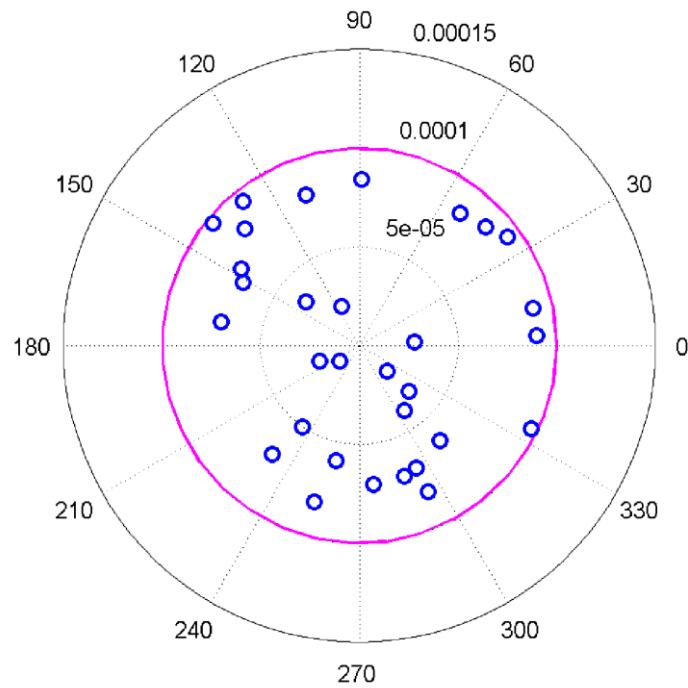


Figure 5.13 The center points of balls' impact positions in a circular area
with diameter of 0.2 mm

5.2.3.1 Pre-Processing

The top surface of the plate is constrained completely as shown in Figure 5.14. The mesh was generated with a 3D 8-node reduced integration element (C3D8R). It was supposed that the target plate was AISI 304 SS owing to the experimental work of Chan et al. (2010). The material parameters and governing equation of the target plate were the JC model in Equation (4.1).

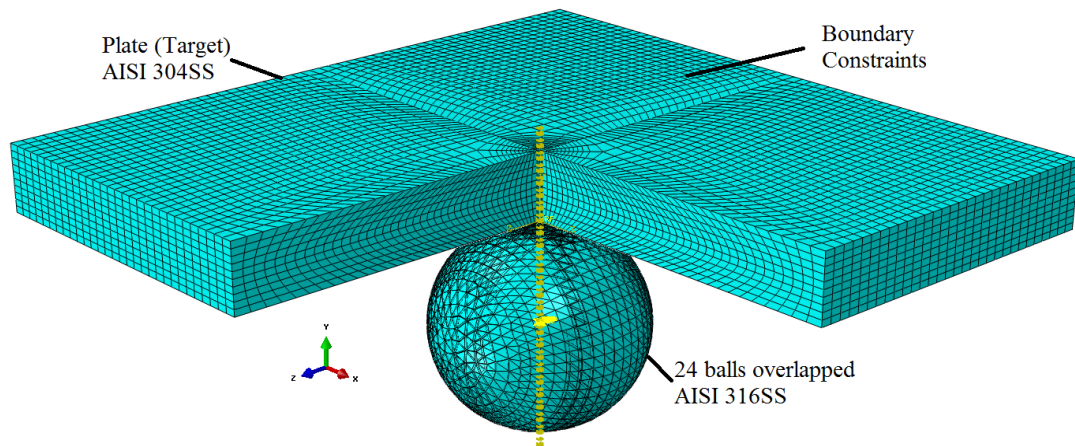


Figure 5.14 Finite element model of 27 balls impacting to the target plate

Same as the single ball impact test, the 316 SS balls were assumed to be pure elastic with the Young's modulus and the Poisson's ratio as 200 GPa and 0.3, respectively. The density of the balls was 7990 kg/m^3 . The material properties of the metal plate are listed in Table 5.2. The JC model, in Equation (4.1), indicates that the material is under work hardening. The enhanced yield stress can be calculated by the first part in JC equation: $A + B\epsilon^n$ (Ruan, et al., 2010a; Ruan, et al., 2010b). It is noted that the effect of the strain rate is not included in the evaluation on the enhancement of the yield stress because the mechanism of the work hardening in high strain rate has not understood well. Although Chen et al. (2011) and Zhu et al. (2011) found that the high strain rate deformation of the stainless steel resulted in nanotwins that led to the enhancement of strength effectively, the working mechanism has needed to further investigate.

Table 5.2 Parameters of AISI 304SS (plate) for Simulation

Density (kg/m ³)	Elastic Modulus (GPa)	Poisson's ratio	A (MPa)	B (MPa)	C	n	M	ϵ_0 (s ⁻¹)	T _m (K)
7930	193	0.3	310	1000	0.07	0.65	1.0	1.0	1673

It was estimated that there were over three million impacts in 10 min with SMAT in a 70-mm-diameter chamber. It was difficult to simulate all these impacts. Therefore, a specific area of a circle with 0.2 mm diameter was selected for further analysis. The number of ball impacts in this area, thus, reduced greatly to 27 impacts. In the experiments found in the literatures, the SMAT process was conducted on both sides of the target plate. Owing to this symmetry, only half of the thickness (0.5 mm) was considered in the analysis. The enhancement of the yield stresses was calculated by averaging the work hardening effect of this specific area with its depth.

5.2.3.2 Residual Compressive Stress

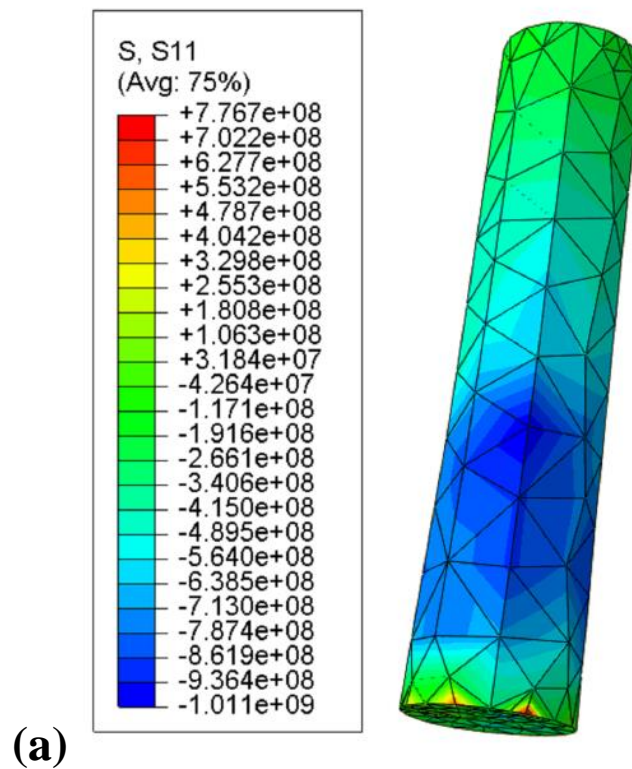
The oblique impact overlapped the impacted area among 27 impacts to have plasticity hardening. Figure 5.15(a) shows the contour plot of residual stresses after 27 impacts.

The residual stresses spread in whole nearby area around the impact locations and

decrease at the depth of the plate. Vertically, the impact energy propagates to the plate and the residual stress decreased sharply along the depth. The residual stresses range from 117 to 936 MPa along the depth in the specific column. The fluctuation of the residual stresses is due to the different impact velocities, the impact positions and the impact angles of each ball. This results on the residual stresses are in an agreement with the experimental findings by Balusamy et al (2013). Their measured residual stress ranged from 229 to 571 MPa with the SMAT of 304 SS using 2-, 5-, and 8-mm-diameter balls in the processing duration from 15 to 60 min. Though the ball size and the processing duration in the simulation are different from the experiment, the distribution of the residual stress in the simulation is similar to their experimental results.

Figure 5.15 (b) shows the in-plane residual stress (σ_{11}) at the origin along the depth of the target plate. The residual stress decreases first from the surface of the plate and reaches the minimum value at a depth of 0.1 to 0.5 mm. The elements at the material surface experience compressive stress, which then propagates to the deeper elements. The deformation of the elements occurs gradually towards the depth of the plate. Due to the propagation of the deformation, the elements, closed to the surface, recovers. The compressive stress or tensile stress occurs occasionally. The values of

the compressive and the tensile stress along the depth of the plate highly depends on the impact velocity, the impact position and the impact angle of ball. When the ball flies at a high velocity, the compressive stress is large. When the ball strikes near the origin, even the impact velocity is small, the compressive stress is also large.



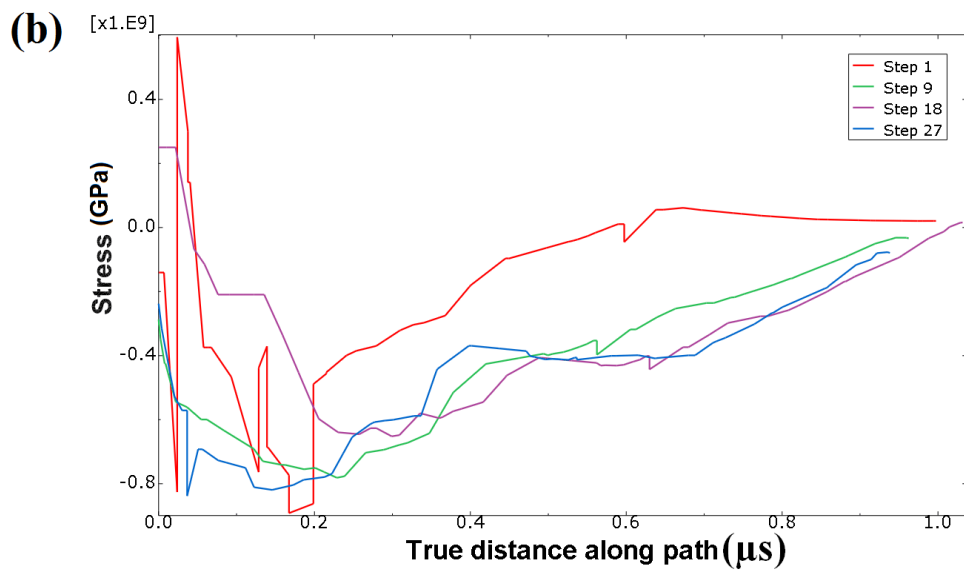


Figure 5.15 (a) Contour distribution of final residual stress and (b) Residual stress along the depth of plate at the origin after 27 ball impacts

5.2.3.3 Comparison on the Predicted Yield Stress

The predicted yield stress was based on the law of isotropic hardening. The yield stress increased due to the plastic strain and was governed by the first part of JC model in Equation (4.1), $\sigma_y = [A + B\varepsilon^n]$. The average yield stress of the specific cylinder is plotted in Figure 5.16. The simulated yield stress and the equivalent plastic strain increase gradually with the increase of the number of ball impacts. When there is no further change in the plastic strain, the yield stress achieves its maximum value. Chan et al. (2010), conducted an experiment under the similar condition. The yield stress

was measured at about 880 MPa. The simulated yield stress is over 730 MPa, which is close to their experimental result. The difference between the simulation and experimental results may be caused by the evolution of the microstructure (nanocrystallization and twinning), which was not involved in the JC model. The effect of the impacts, close to the selected area, may also contribute to the enhancement of yield stress, which was not considered in the simulation as well.

Another simulation, without considering the impact angle, was conducted to maximize the energy transmission in the impacts. The ball velocity was 10 m/s in normal direction of all the balls. The average yield stress results are plotted in Figure 5.17. The simulated yield stress is 790 MPa, which increases about 10% compared with the random impacts. The SMAT process on both sides also played an important role in the stress distribution. After considering all these factors, the simulation result predicted well with the experimental results found in the literature.

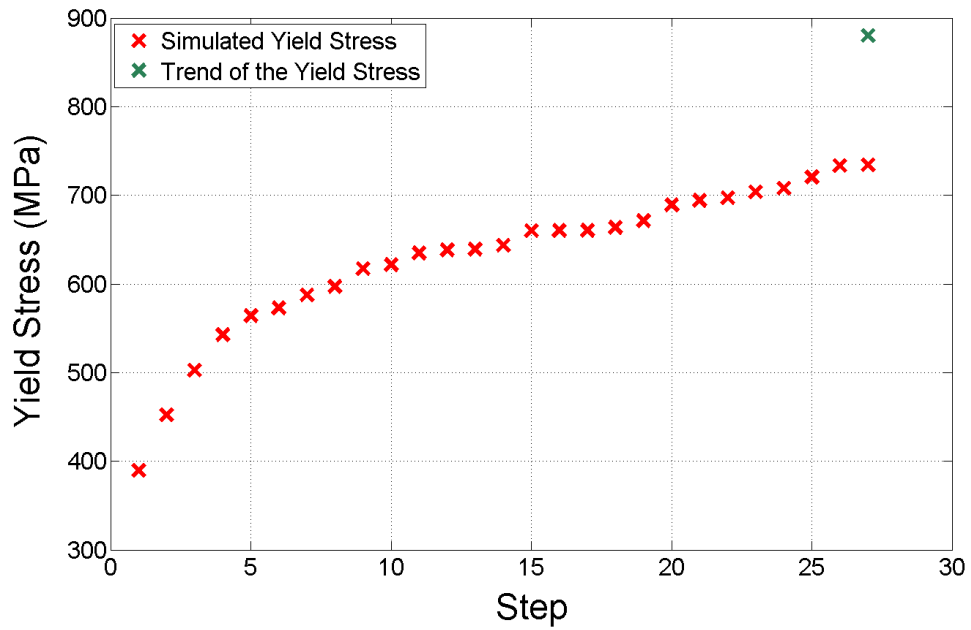


Figure 5.16 Averaging simulated yield stress on the specific area at various impact velocities, positions, and angles

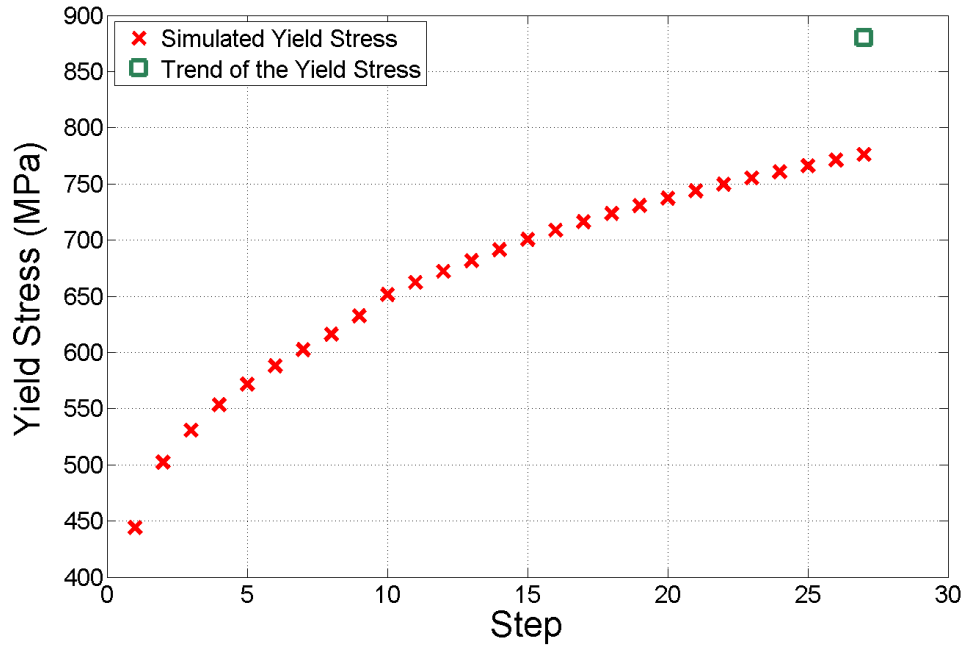


Figure 5.17 Averaging simulated yield stress with all the balls' velocity at 10 m/s

5.3 Summary

Finite element analysis was conducted to simulate the SMAT process by the embedded JC model in a commercial software, ABAQUS. The results were achieved (i) to determine the effects of the ball velocity and the impact angle through a single ball impact; and (ii) to predict the mechanical properties in a selected region in the SMAT process.

In the first case, when the ball velocity was faster, the effective area was wider and deeper with a larger stress value. The equivalent plastic strain rate was also greater at a higher ball velocity and remained unchanged after 0.4 μ s. It was also observed that the increase in the equivalent plastic strain rate resulted in a steady stress-strain relationship with the ball velocity. Other than the ball velocity, the impact angle was also studied. The vertical component of the ball velocity played an important role in the strain hardening process. The oblique and normal impacts with the same vertical velocities were matched generally when comparing with their stress-strain relationship and equivalent plastic strain rate. To eliminate the effect of impact angle, the longer processing duration was recommended to allow more balls struck at the same position. This assured the production of an isotropy and harder metal with the SMAT.

In the second case, multiple ball impacts were investigated through the simulation on the impact positions generated by a MATLAB simulation introduced in Chapter 3. The simulated result were further processed by the first part in JC equation, $\sigma_y = [A + B\varepsilon^n]$, to determine the yield stress. The result was compared to the experimental one found in the literature. The simulated yield stress at different and constant ball velocities (10 m/s) were lower than that found in the experiments. However, the trends of the yield stress in the simulation were agreed generally with the tensile test result found in the literature.

CHAPTER 6 - SIMULATION OF SMAT BY CONSTITUTIVE MODEL

6.1 Introduction

In SMAT, the random ball impacts in the vacuum chamber maintain the isotropic material properties of the treated metal by inducing nano-grains. General material laws can describe the macroscopic effects to the metal without considering of the micro-structure evolution. As presented in Chapter 4, a new constitutive model was developed for stress prediction in the context of micro-structure evolution and macro-structure effects. In this section, the new constitutive equation is applied in FEA to simulate the stress distribution on metal in SMAT.

As in Chapter 5, commercial FEA software, ABAQUS, was used to apply the new constitutive equation in the simulation. However, a subroutine program was written. To test the coding of the subroutine, an embedded JC model was applied to a single-element model and a single-ball impact model for comparison. After verification of subroutine, a simulation of multiple ball impacts was then developed with which the balls' impact positions and velocities were obtained in the MATLAB simulation.

6.2 Single-Element Test

Because ABAQUS can input a subroutine to custom-make the governing equation in the simulation, it is important to have a single-element test to ensure that the subroutine is compatible and correctly programmed. To verify the accuracy of the subroutine in ABAQUS, a single-element test was conducted at the beginning of the study using JC model as the material law. A single-element cubic was compressed in the y-direction and became a cuboid, as shown in Figure 6.1. Because ABAQUS/Explicit was used in the development of the user-subroutine in the modification of the JC equation, the embedded program and the explicit subroutine, VUMAT, simulations are compared and the results are shown in Figure 6.2.

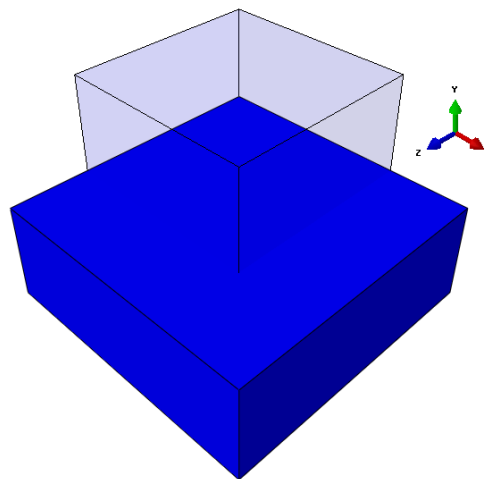


Figure 6.1 Configuration of a single-element test

As illustrated in Figure 6.2, the stress-strain curves of both simulations are similar and have the same pattern. After passing through the yield point, the element begins

to show plastic deformation. By the comparison, the VUMAT subroutine coding is fitted for further development on the modification of the JC model.

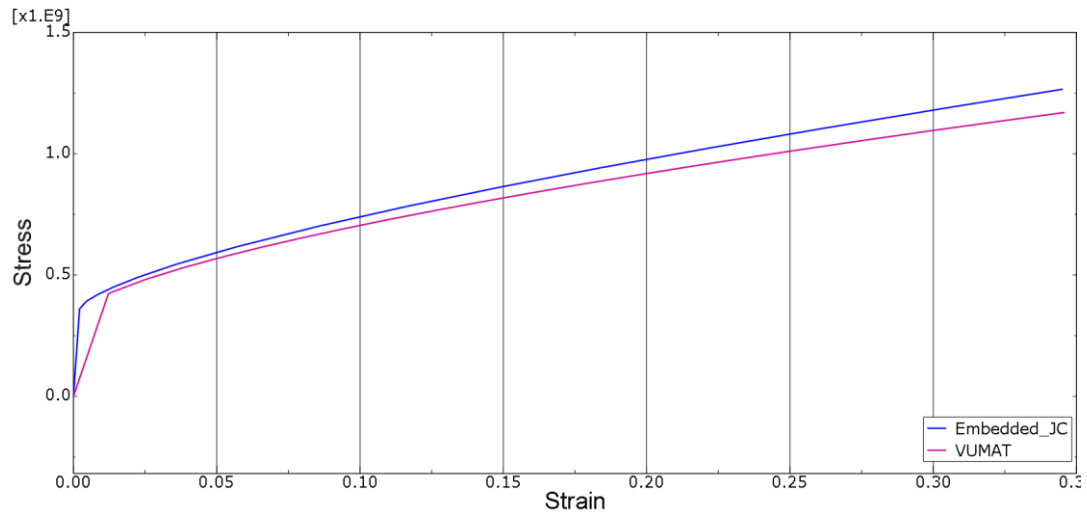


Figure 6.2 Comparison of Stress-Strain Curve in a single-element test

6.3 Single-Ball Impact Test

In SMAT, a number of balls fly in a vacuum chamber and strike the target metal numerous times. The ball impact is a dynamic motion for which dynamic simulation is required. To verify the dynamic simulation, a single-ball impact simulation was conducted to compare the coding of the subroutine VUMAT and the embedded JC model. In this simulation, a plate is fixed, and the ball strikes to the bottom surface of the plate at 10 m/s in a step. The plate and ball are assumed to be 304 SS and 316 SS, respectively. Figure 6.3 shows the contour plot of von Mises stress for subroutine

VUMAT. When a ball strikes the plate, the impact center experiences concentrated pressure and then spreads out concentrically.

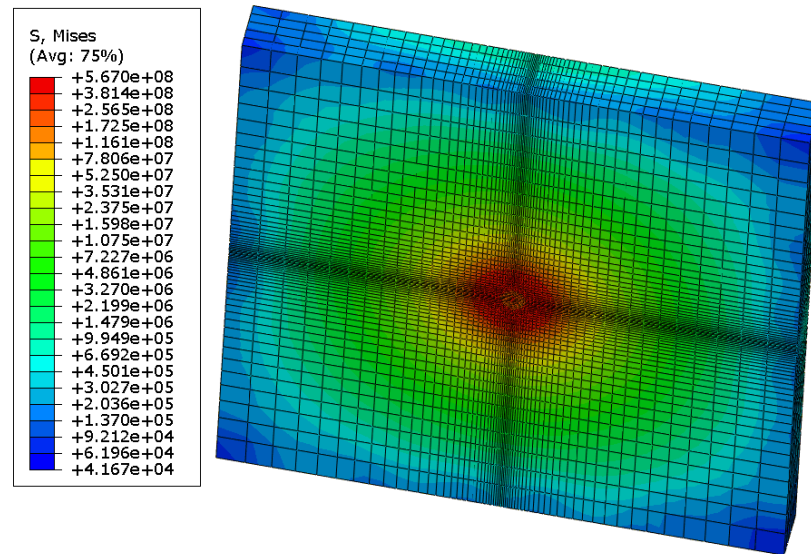


Figure 6.3 Contour plot of von Mises stress (VUMAT)

The simulation results, embedded model and VUMAT, are compared in Figure 6.4. Both curves are well-fitted when comparing their node 1215, the center node of the plate.

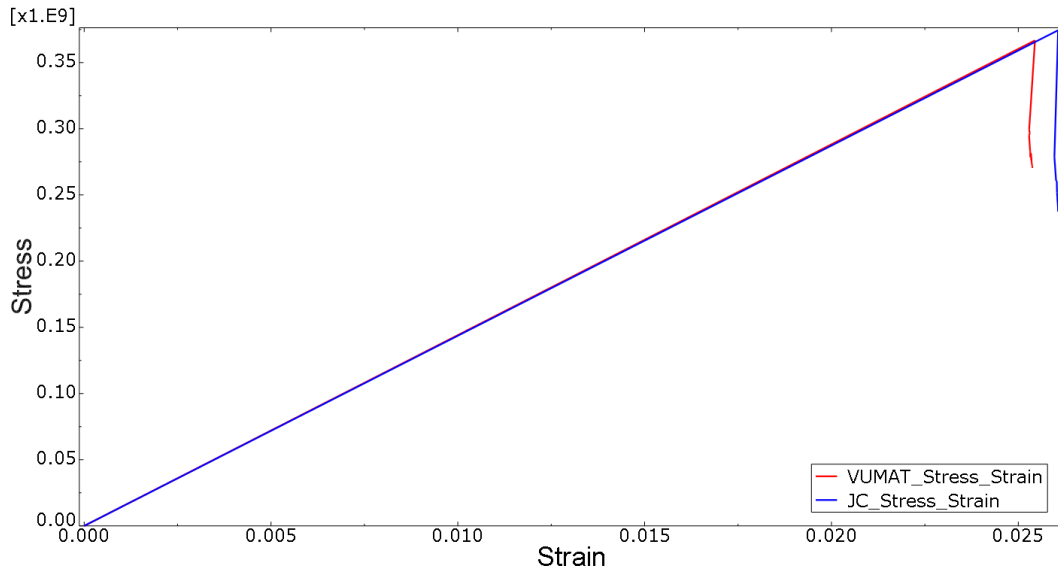


Figure 6.4 Comparison of Stress-Strain results simulated with the embedded and VUMAT JC model

Even a single ball impact triggers plastic deformation. As shown in Figure 6.5, the equivalent plastic strain obtained by two approaches are generally fitted. At 5 μ s, the impact point experienced plastic deformation and saturated for the rest of the time. There was no change in the equivalent plastic strain rate in the impact. In addition, the variation of stress with respect to time is almost the same with the subroutine and with the embedded JC model in Figure 6.6. The VUMAT subroutine generally simulates the SMAT process well. The new constitutive equation can then be applied by modifying the subroutine in ABAQUS.

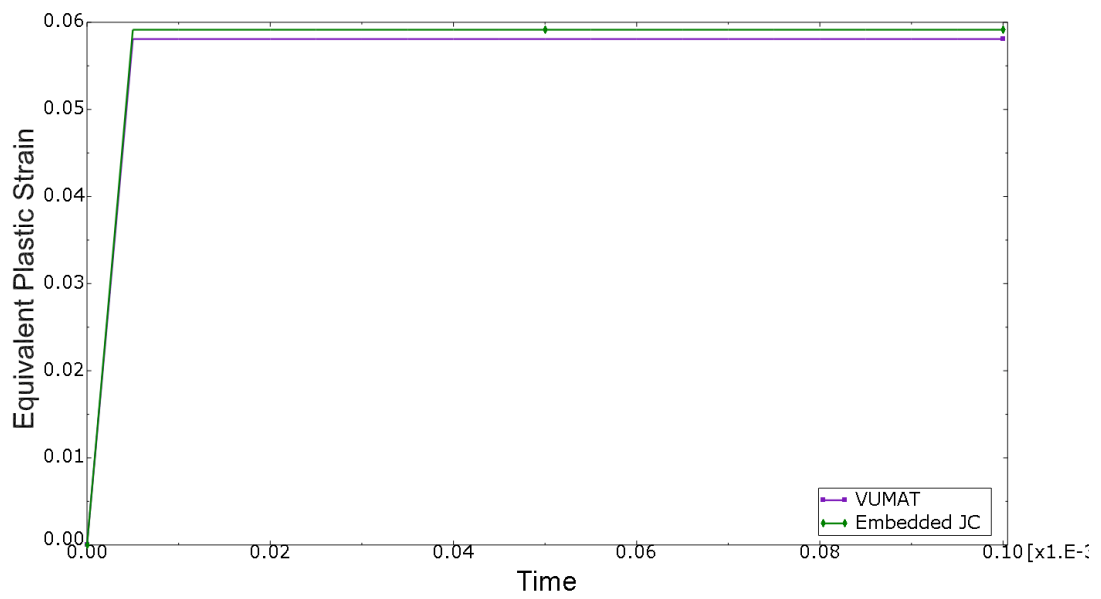


Figure 6.5 Comparison of equivalent plastic strain simulated with the embedded and VUMAT JC model

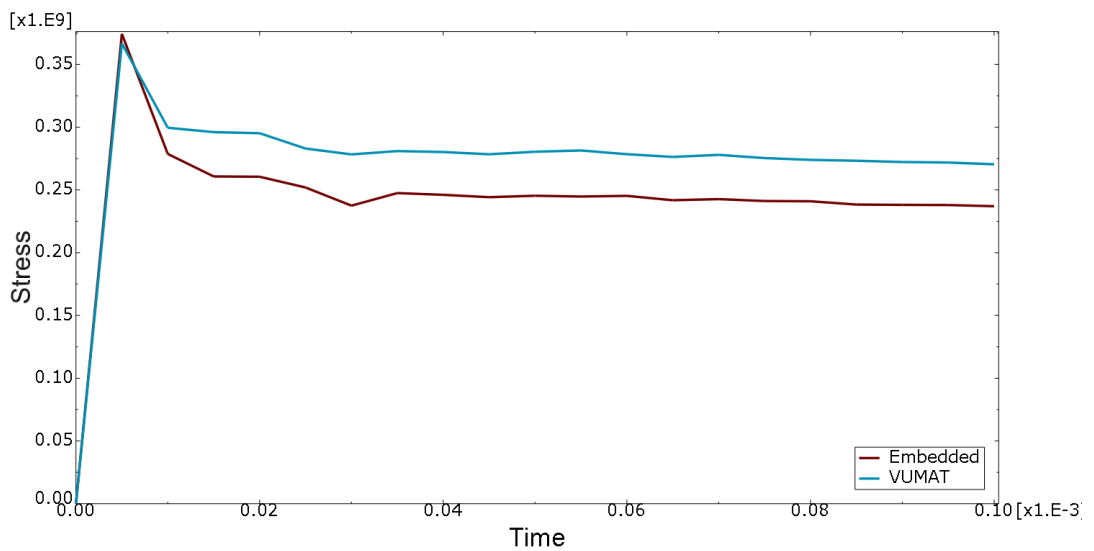


Figure 6.6 Comparison of stress simulated with an embedded and VUMAT JC model

6.4 Multiple Impacts in SMAT Simulated by Constitutive Equation

To simulate the mechanical properties after SMAT, multiple-impact simulation was conducted with the implementation of constitutive equation. The modified JC equation was applied in the ABAQUS simulation by a subroutine function, VUMAT. Two cases were investigated, with processing durations of 3 and 10 min. One hundred imaginary balls were positioned in a cylindrical chamber with a 70-mm diameter and 15-mm depth. It was assumed that the center of the plate will not be affected by the edge effect, so only the circular area was selected to be impacted by the balls. The balls' positions and impact velocities in this selected area were first determined via the MATLAB simulation. The simulation model for these two cases is shown in Figure 6.7. For validation, the mechanical properties of this selected area were determined and compared with the experimental results in studies that used the same conditions.

This simulation setting was the same as the FEA presented in Chapter 5.2.3 except that, the general JC model was replaced with the new constitutive equation. The material properties of the plate (AISI 304 SS) are listed in Table 5.2. Only the

material constant A was updated by the constitutive equation according to the strain rate, as presented in Chapter 4.

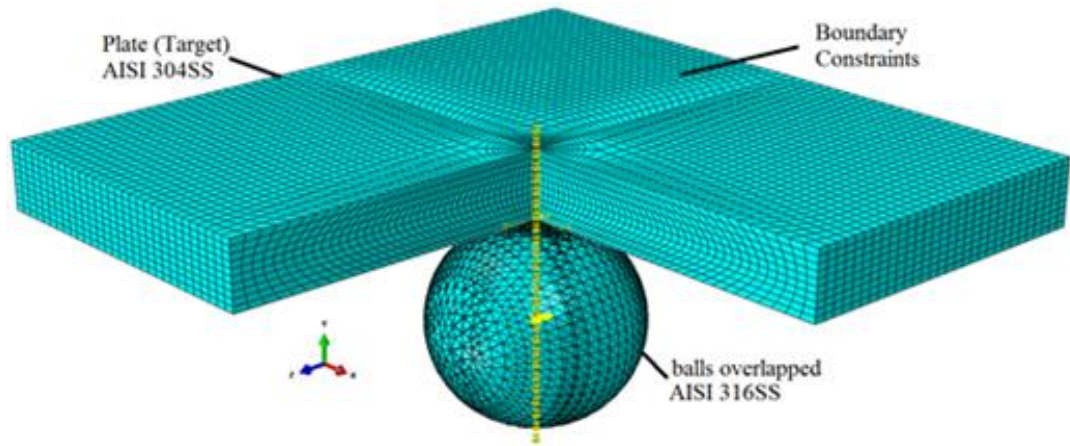


Figure 6.7 Setting of simulation model

6.4.1 Case 1: 3-Min Process

In this case, it was assumed that the SMAT process was conducted for 3 min. After simulation with by MATLAB, the impact position and velocity of each ball in the selected area are listed in Table 6.1.

Table 6.1 Impact positions and velocities of each ball for 3-min process

Ball no.	Impact Position (m)			Impact Velocity (m/s)		
	x	y	z	x	y	z
1	6.900E-05	0.0	3.900E-05	-0.306	1.519	-0.597
2	4.200E-05	0.0	8.700E-05	0.080	7.890	-0.188
3	-9.200E-05	0.0	6.000E-06	2.336	4.991	3.060
4	3.000E-06	0.0	8.200E-05	-0.198	2.541	0.096
5	4.600E-05	0.0	-4.200E-05	0.926	7.380	-1.028
6	-5.900E-05	0.0	-3.800E-05	-0.513	7.778	0.318

6.4.1.1 Case 1: Results and Discussions of the Stress Distribution

The stress distribution of an element set, the selected impact area, is shown in Figure 6.8. The maximum stress was 563.7 MPa at the bottom of the plate (the impact area), and the minimum stress was 42.91 MPa at the top surface. The stress propagated from the bottom surface to the top surface, possibly because the impact surface received a greater deformation than the top surface. As illustrated in Figure 6.9, the equivalent plastic strain decreased along the thickness of the plate. A sharp drop in the equivalent plastic strain was found from the 0.1- to 0.3-mm depth of the plate, as measured from the impact surface, which is consistent with the von Mises stress distribution. A higher stress level was concentrated on the impact surface underneath.

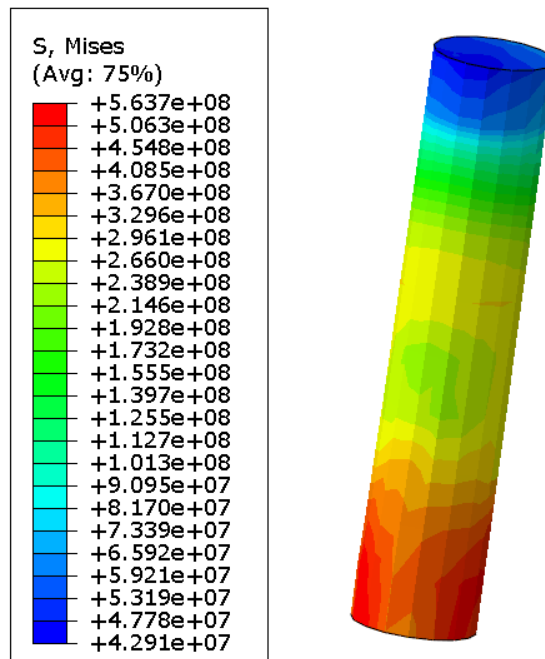
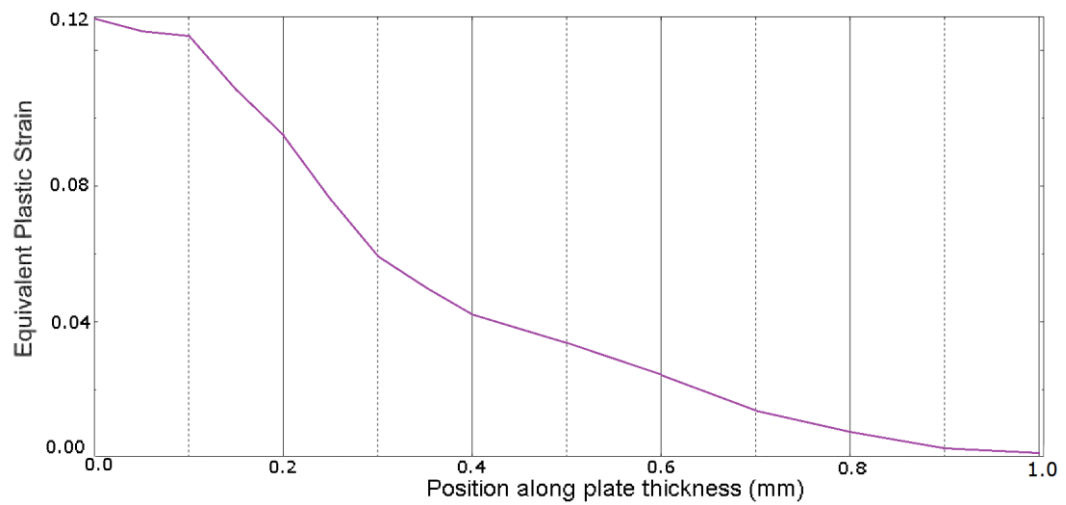


Figure 6.8 von Mises stress on the selected area for 3-min process**Figure 6.9 Equivalent plastic strain along the thickness of plate**

As reported by Chan et al. (2010), the yield true stress was obtained at about 800 MPa. To compare the experimental results, the simulated equivalent plastic strain and the static yield stress, σ_y , are used to determine the estimated yield stress ($A + B\epsilon^n$) after the SMAT. Figure 6.11, shows six steps for the ball impact. The estimated yield stress increased gradually until 1.16 GPa. The simulation result is higher than the results of the tensile conducted by Chan et al. (2010), 800 MPa.

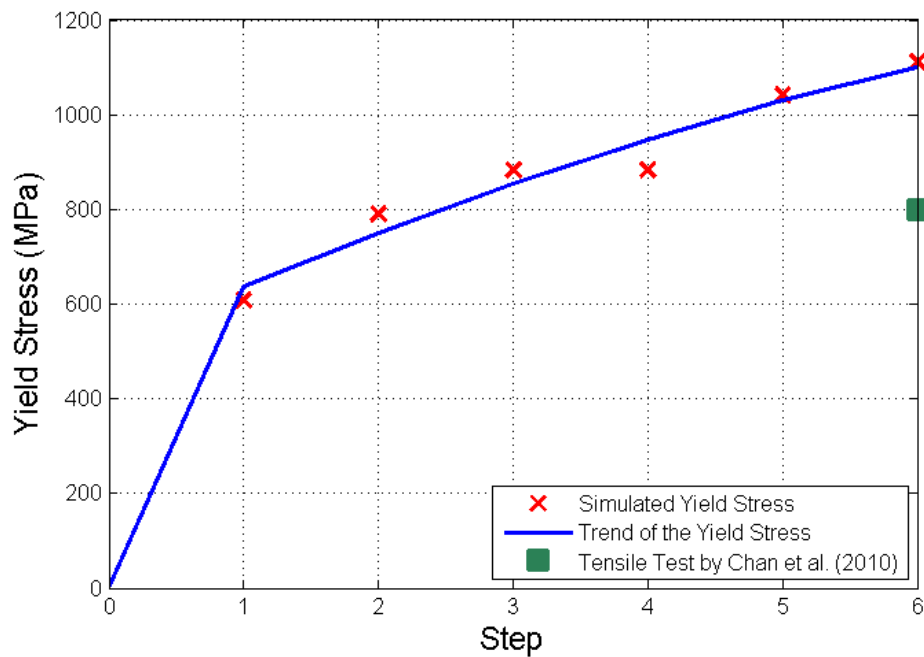


Figure 6.10 Estimated yield stress ($A + B\varepsilon^n$) calculated by equivalent plastic strain for 3-min process

The parameter A in the constitutive equation was changing due to the impact.

The final value of A after the SMAT was used to predict the tensile test result and then compared to the experimental result as reported by Chan et. al. (2010) in Figure 6.11.

The final parameter A was 723 MPa. The estimated result is agreed with the tensile test result in the experiment at the same SMAT condition.

Reviewing the impact velocity of each ball, the increase in the yield stress was caused by the high impact velocity. At step 2, the impact velocity in the normal direction was more than 7.89 m/s. The estimated yield stress then increased sharply as the high-impact velocity that caused greater plastic deformation, as illustrated in

Figure 6.12. The estimated yield stress further increased gently at steps 3 and 4. The corresponding equivalent plastic strains increased gradually, thus, the estimated yield stress tended to be saturated until greater impacts at steps 5 and 6. The high impact velocities, over 7 m/s, at these two steps caused the strain rate to increase sharply so that the estimated yield stress further increased and reached its maximum value.

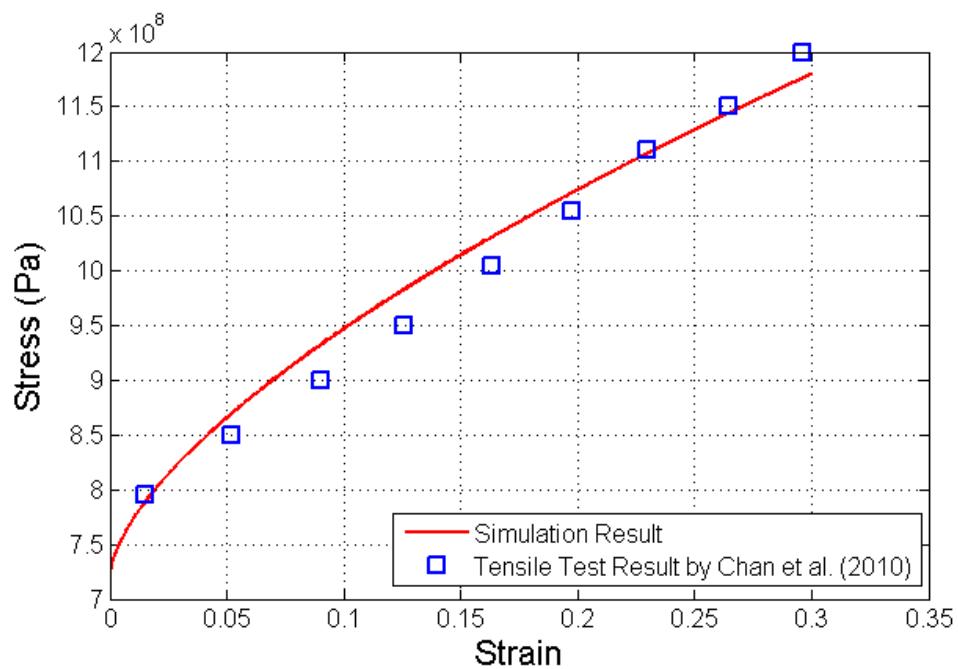


Figure 6.11 Estimated tensile stress-strain curve by A at 723 MPa for 3-min process

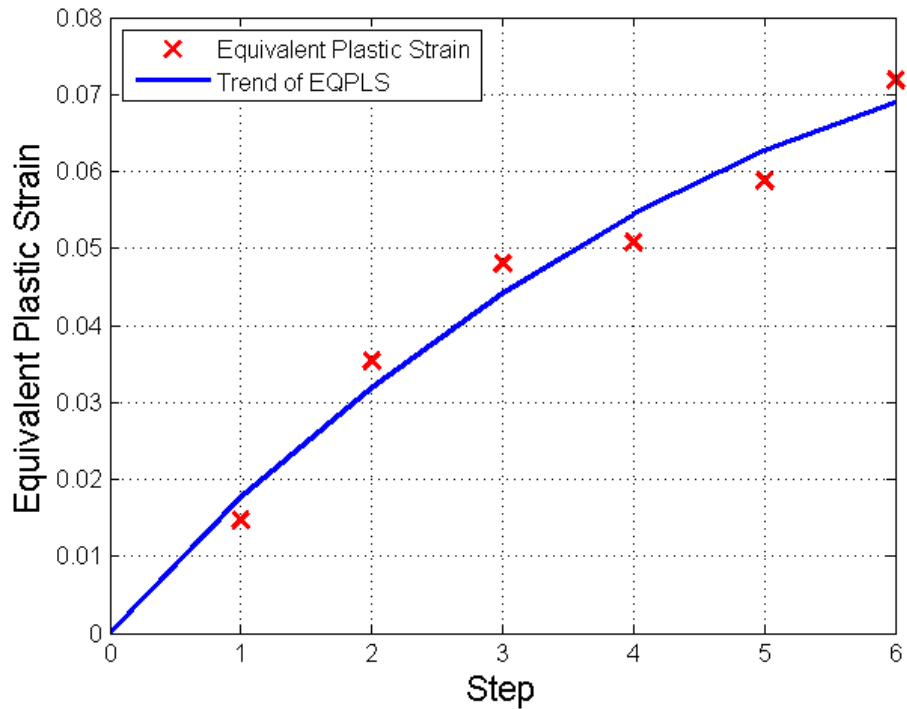


Figure 6.12 Equivalent plastic strain result for 3-min process

The equivalent plastic strain is plotted in Figure 6.13. From this contour plot, it can be seen that the maximum deformation has not yet occurred at the origin of the plate. The random impact in SMAT caused deviation of the impact positions and directions that enhanced the spread of the plastic deformation. The spread of the equivalent plastic strain was spherically toward the top surface of the plate. The energy, however, was not transferred sufficiently to the entire thickness of the plate.

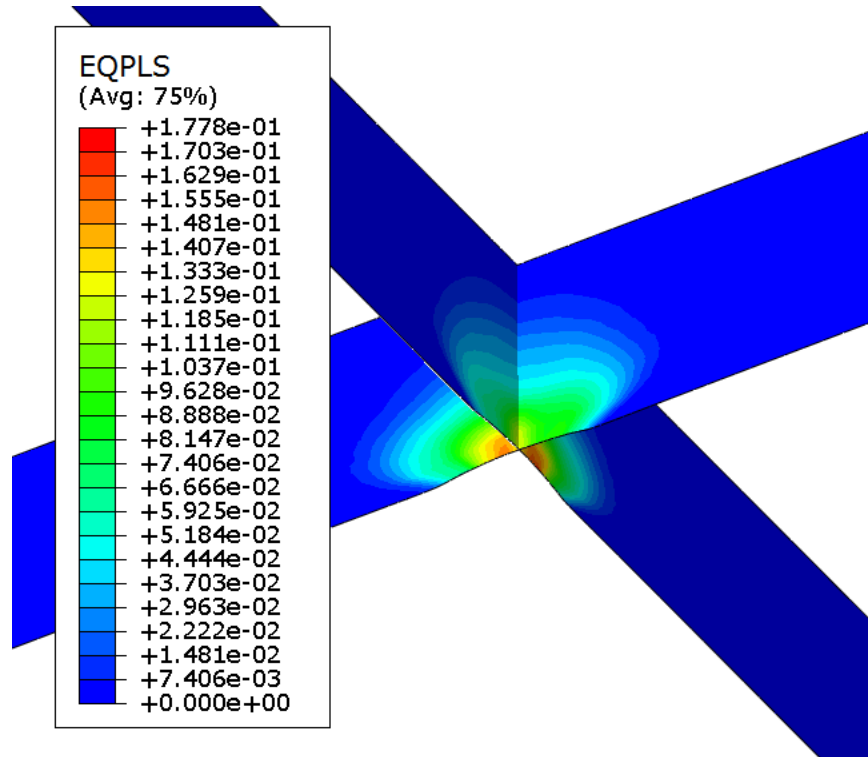


Figure 6.13 Contour plot of equivalent plastic strain for 3-min process

The average flow stress in the selected area is plotted in Figure 6.14. After six impacts to the plate, the flow stress was 1.2 GPa. The trend of the flow stress was the same as that of the estimated yield stress. Figure 6.15 shows that the average flow stress decreased along the depth of plate and saturated at 0.6 mm. The shorter processing duration led to fewer impacts on the selected area. Energy transmission was inefficient along the plate.

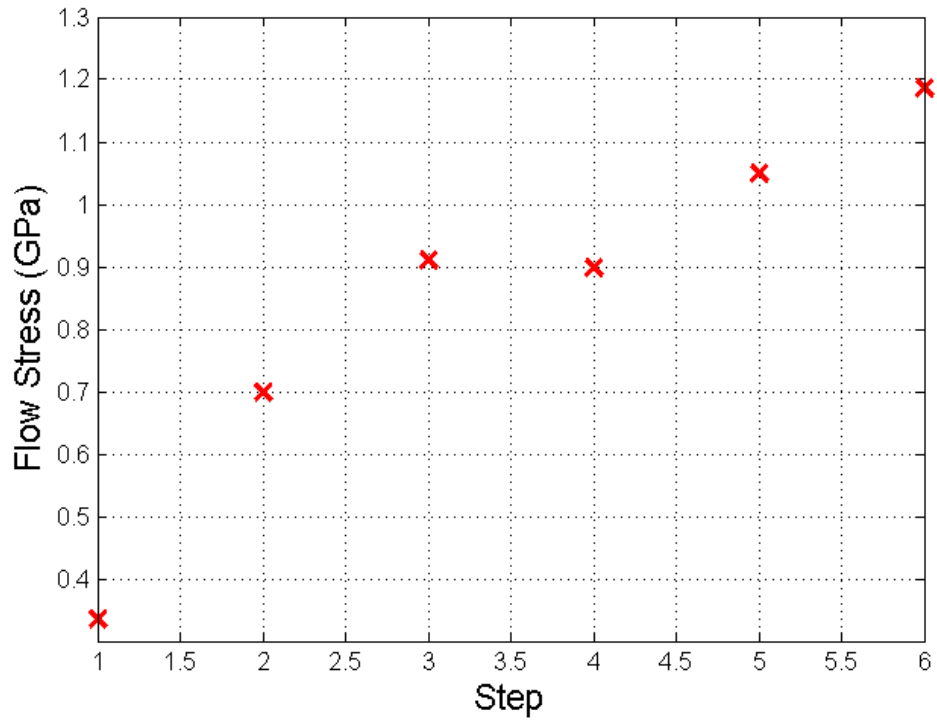


Figure 6.14 Average of flow Stress for 3-min SMAT

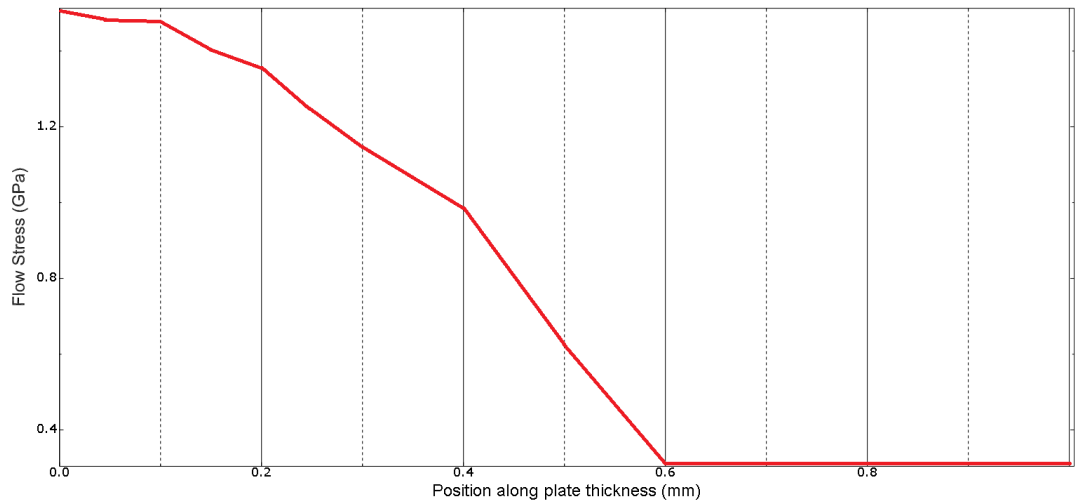


Figure 6.15 Average flow stress along the depth of plate for 3-min process

6.4.1.2 Case 2: Results and Discussions on the Microstructure**Evolution**

In SMAT, the contribution to the stress is not just the equivalent plastic strain. The evolution of the microstructure also affects the static yield stress. Once the grain size and twin spacing diminish, the static yield stress increases. The refinement of the grain is shown in Figure 6.16. The grain size decreased sharply until steps 3 and 4 and was further refined at steps 5 and 6. After six impacts, the average grain size was 54.8 nm. According to the constitutive equation, when the strain rate is less than $10^4/s$, the grain will be refined, otherwise, the mechanism of twin refinement will be triggered. Because the impact velocities at steps 3 and 4 are low, the strain rate may not be sufficient to trigger the twin refinement. The lack of energy does not cause any grain reduction. As shown in Figure 6.17, the dispersion of grain size was spherical; however, no further grain refinement occurred in half of the depth. At the top surface of the plate, the grain size was about 26.7 nm.

When compared with the findings in the literature, the grain size was approximately $10\ \mu\text{m}$ in the top $50\text{-}\mu\text{m}$ surface after 10 min of processing (Chan et al., 2010), which is much smaller than the simulated grain size here, possibly because of the short processing. In a 3-min SMAT, there are insufficient impacts to refine the

grain. When the processing duration is longer, there are more chances to have more impacts at the same location to achieve smaller grains.

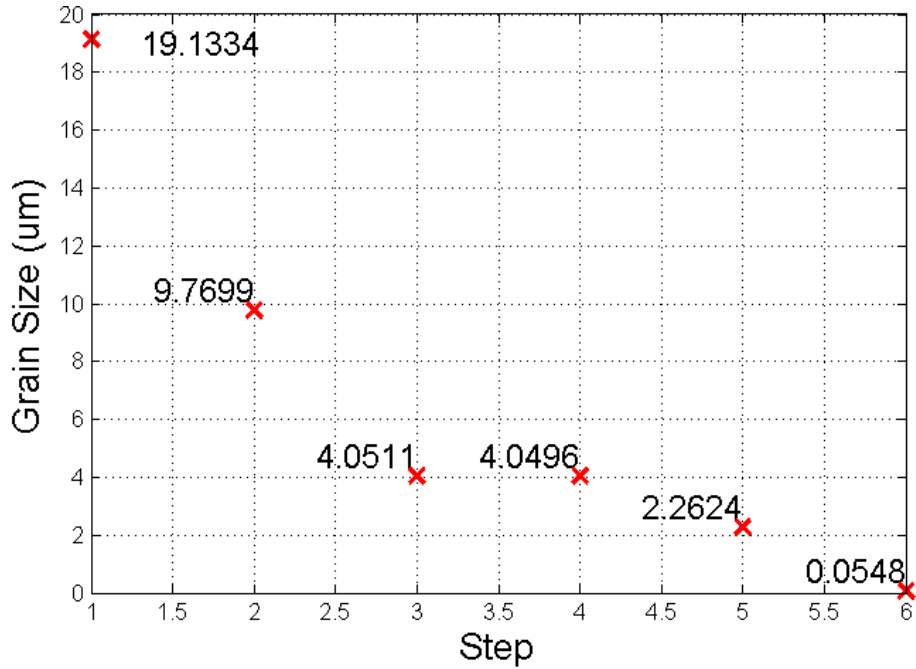


Figure 6.16 Average grain size for 3-min process

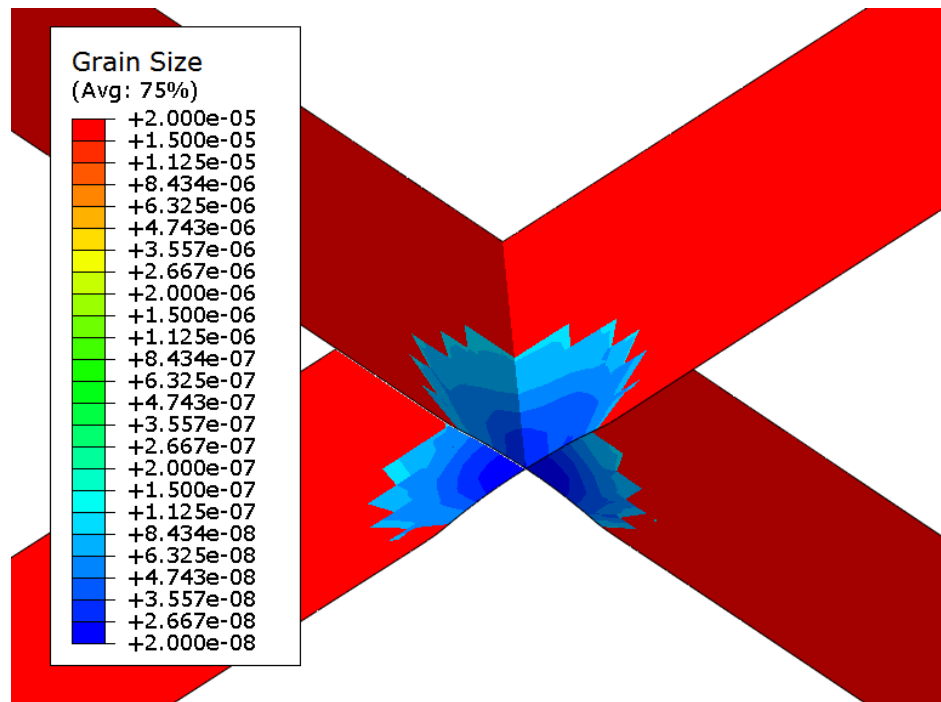


Figure 6.17 Contour plot of grain size for 3-min process

The reduction of twin spacing was also simulated and is shown in Figure 6.18.

The trend of twin refinement was similar to that of grain refinement. The average twin spacing sharply decreased in the first 3 steps and stopped diminishing. When the balls' impact velocity was sufficient, the average twin spacing resumes its reduction. Finally, the average twin spacing was 46.3 nm.

As shown in the contour plot of twin spacing in Figure 6.19, the dispersion of twin spacing was also spherical and stopped refinement at half the thickness.

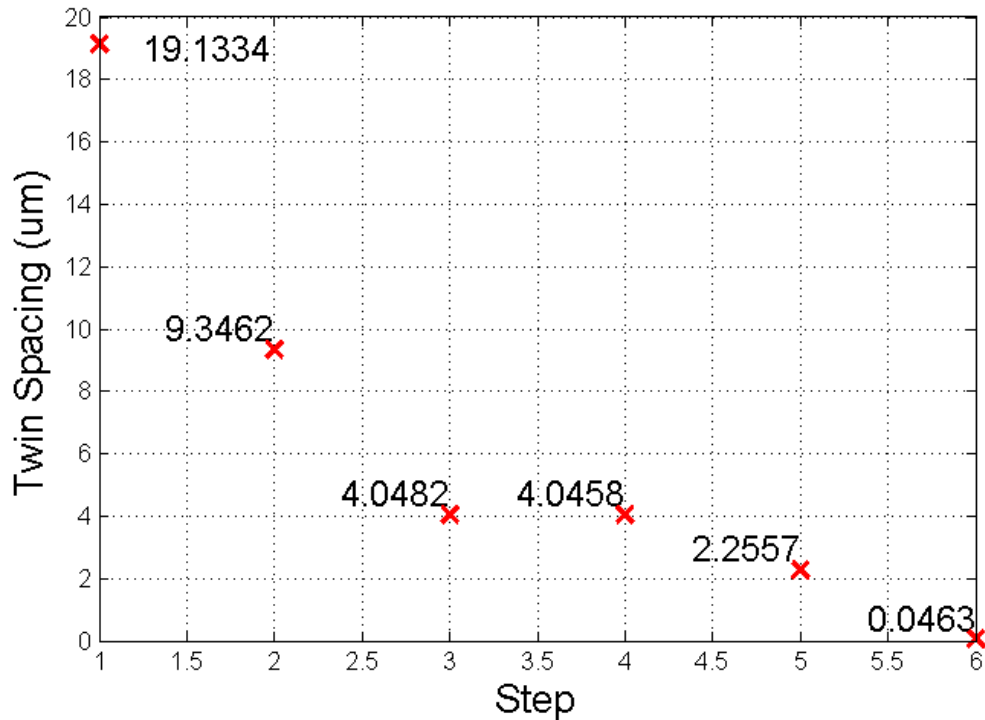


Figure 6.18 Average twin spacing for 3-min process

The average grain size and twin spacing were very close together in these steps. Recalling the determination of grain size and twin spacing in Section 4.2.4, the equivalent plastic strain acts as a crucial factor in the iteration of grain size and twin spacing. When the equivalent plastic strain is small, the refinement rate of the grain and twin spacing is close. In this case, the processing duration was only 3 min. There were few impacts per unit area, and the energy penetration to the plate was not sufficient for the equivalent plastic strain to retain a small value. The differences in the grain size and twin spacing are not obvious.

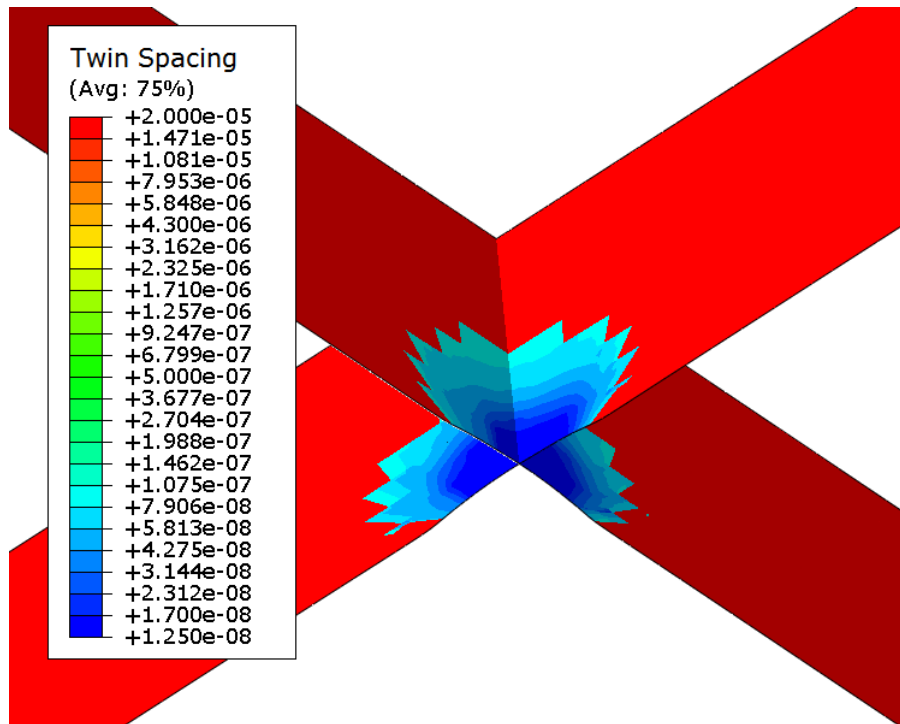


Figure 6.19 Contour plot of twin spacing for 3-min process

6.4.2 Case 2: 10-min Process

Concerning the s case, the SMAT is conducted for 10 min. Within 10 min, there are 27 impacts on the selected area. The corresponding impact positions and velocities for the 27 balls are listed in Table 6.2.

Table 6.2 Impact positions and velocities of each ball for 10-min process

Ball NO.	Impact Position (m)			Impact Velocity (m/s)		
	x	y	Z	x	y	z
1	8.800E-05	0	1.900E-05	0.053	4.280	-0.720
2	3.500E-05	0	-7.400E-05	-0.034	3.514	-0.082
3	8.700E-05	0	-4.200E-05	-0.072	7.759	1.385
4	2.900E-05	0	-6.200E-05	-0.037	7.817	0.054
5	-5.900E-05	0	3.200E-05	2.180	4.170	0.401
6	-2.300E-05	0	-7.900E-05	-0.192	5.425	0.329
7	-1.200E-05	0	-5.800E-05	-0.335	-3.779	0.562
8	-9.000E-06	0	2.000E-05	1.022	6.405	-1.690
9	1.000E-06	0	8.400E-05	-0.051	4.662	-0.176
10	1.400E-05	0	-1.300E-05	0.987	6.229	0.094
11	9.000E-05	0	5.000E-06	-0.039	6.026	-0.587
12	-6.000E-05	0	3.900E-05	-0.185	4.561	-0.705
13	7.500E-05	0	5.500E-05	0.091	3.307	-0.448
14	-2.000E-05	0	-8.000E-06	-1.498	5.918	-0.180
15	-7.400E-05	0	6.200E-05	0.149	2.202	0.258
16	-7.000E-05	0	1.200E-05	-0.868	3.330	0.739
17	7.000E-06	0	-7.000E-05	0.134	4.741	0.082
18	5.100E-05	0	6.700E-05	1.985	2.586	0.057
19	-2.700E-05	0	2.200E-05	-0.126	9.074	-0.159
20	-5.800E-05	0	5.900E-05	-0.102	7.577	-0.797
21	2.300E-05	0	-3.300E-05	0.658	4.004	1.380

CHAPTER 6 – SIMULATION OF SMAT BY CONSTITUTIVE MODEL

22	2.300E-05	0	-6.600E-05	0.790	6.589	0.738
23	4.100E-05	0	-4.800E-05	0.146	3.499	1.042
24	6.400E-05	0	6.000E-05	-0.361	8.230	-0.593
25	-2.700E-05	0	7.600E-05	0.265	6.148	0.248
26	-5.900E-05	0	7.300E-05	-0.341	4.282	-0.197
27	-4.400E-05	0	-5.500E-05	1.048	4.130	-0.463

6.4.2.1 Case 2: Results and Discussions on the Stress Distribution

The selected impact area is extracted, and the result of von Mises stress is shown in Figure 6.20. Maximum stress was found at the bottom of the plate, that is, the impact location, up to 1.66 GPa. Energy was transferred to the top surface gradually so that the stress decreased to 0.1 GPa.

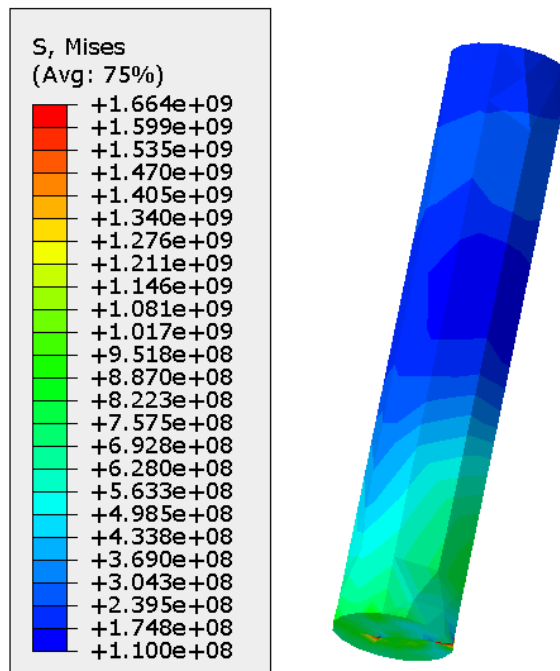


Figure 6.20 Contour plot of von Mises stress result on element set of selected area for
10-min process

In the experiment, when 304 SS underwent SMAT for 10 min with 100 stainless steel balls impacted, the yield stress obtained with the tensile test was nearly 1000 MPa, as shown in Figure 6.21 (Lu et al., 2011). In another study, the yield stress determined from the true stress-strain curve was 880 MPa for 304 SS after treatment for 10 min (Chan, et al., 2010). To compare the simulated result with the experimental result, the trends of the simulated yield stress were calculated at each step by averaging the stress ($A + B \epsilon^n$); Figure 6.23.

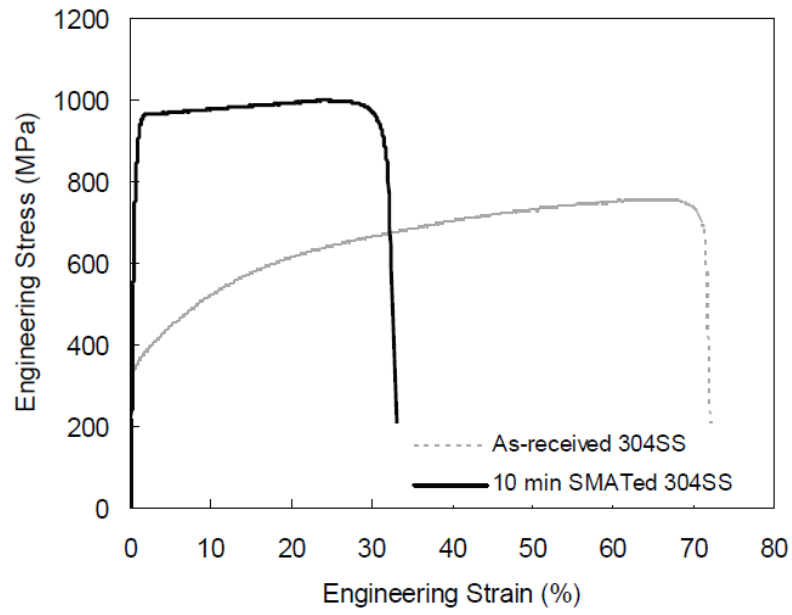


Figure 6.21 Engineering stress-strain curve as-received 304 SS and for 10-min process (Lu, et al., 2011)

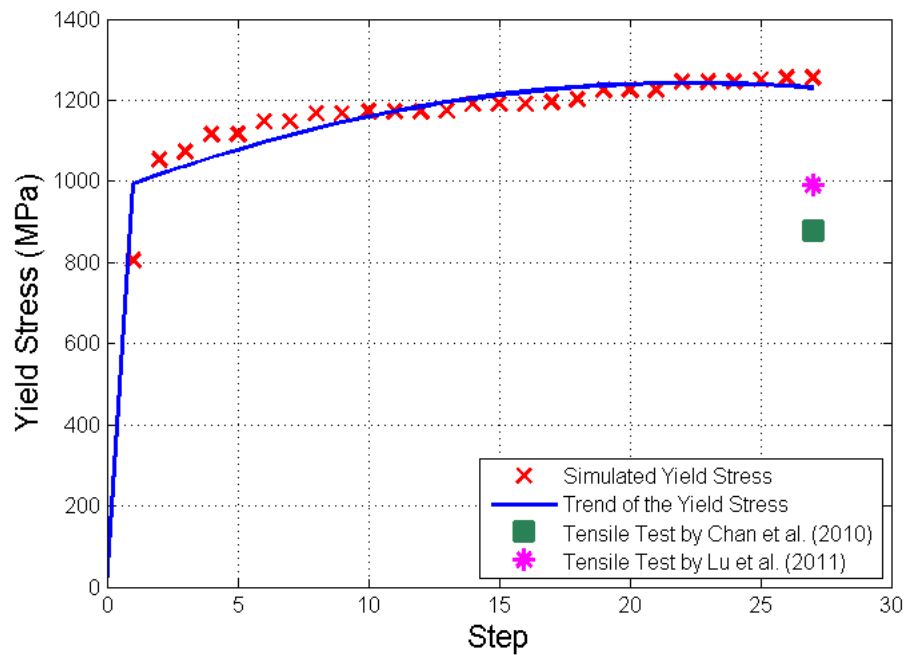


Figure 6.22 Comparison of simulated ($A + B \epsilon^n$) and experimental yield stress results for 10-min process

After 10-min process of SMAT, the varying yield stress, parameter A, was at 781 MPa and used to plot the tensile stress-strain curve in Figure 6.23. The estimated stress-strain curve was compared with the tensile test result reported in the literature for 10-min process. The estimated stress-strain curve is agreed well with the experimental one.

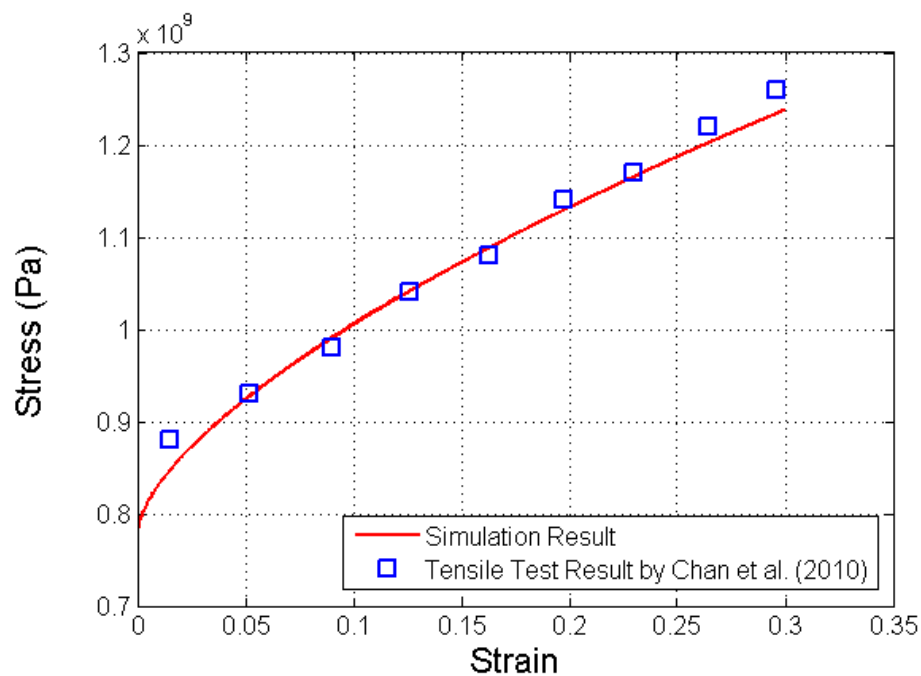


Figure 6.23 Estimated tensile stress-strain curve by A at 781 MPa for 10-min process

In the simulation, the yield stress increased gradually up to 1.23 GPa after 27 ball impacts at the selected area by strain hardening. As shown in Figure 6.24, the equivalent plastic strain in the y-direction (i.e., the plate thickness) increased gradually. The contour plot of the equivalent plastic strain in the final step in Figure 6.25 shows

that the strain hardening spread out from the impact location to the depth of the plate. The impact energy was sufficient to cause plastic deformation in each step, which contributes to the further increase of the yield surface.

The simulated value is higher than the yield stresses obtained in the literature. When compared to the experimental results obtained by Chan et al. (2010) and Lu et al. (2011), the true stress differs from the engineering stress under the same conditions, possibly due to imperfections in the material in the experiment. The metal may initially contain nano-scale defects or dislocations before the SMAT. However, in the simulation, it is assumed that the target plate, 304 SS, is perfect without any defect inside the grain, which is pure and perfect crystal. This may lead to overestimation of the yield stress in the simulation.

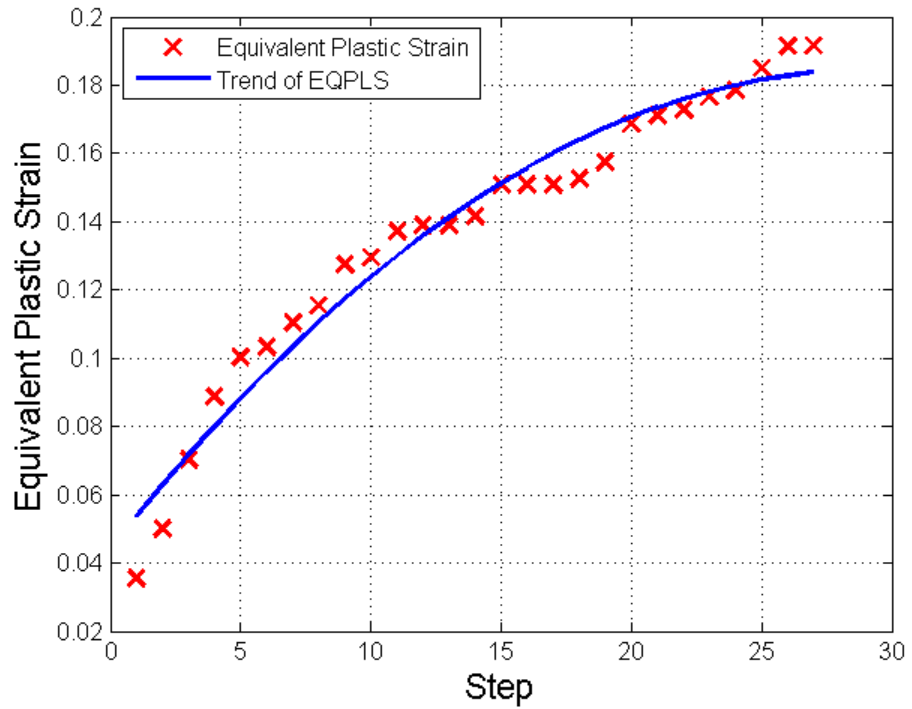


Figure 6.24 Equivalent plastic strain (EQPLS) plot in each impact for 10-min process

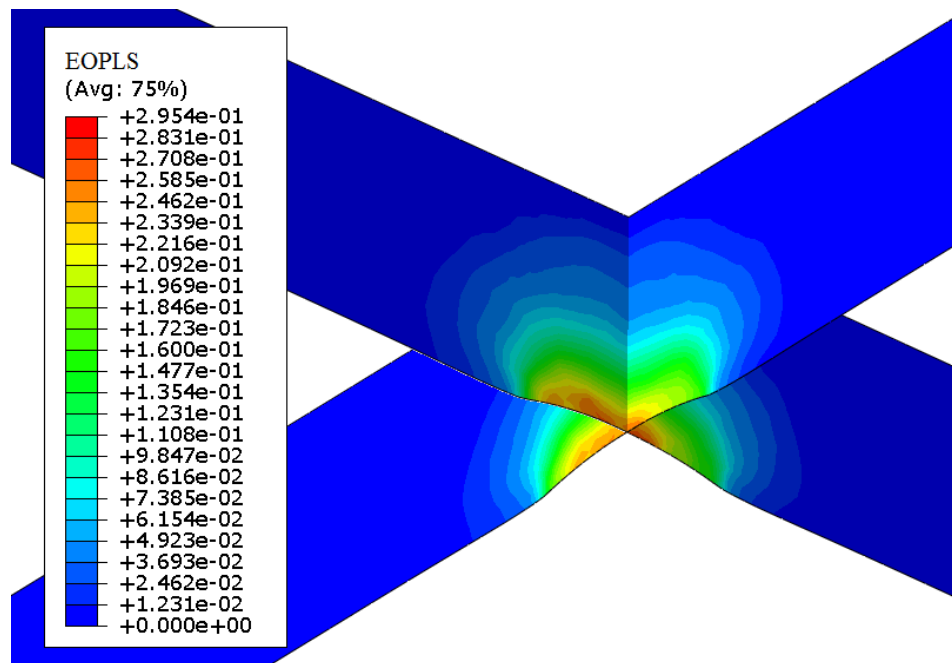


Figure 6.25 Contour plot on the equivalent plastic strain in last step for 10-min process

The average flow stress in the selected area is plotted in Figure 6.26 at each step.

The flow stress gradually increased at around 1.6 GPa. Similar to the yield stress, the flow stress also tended to saturate after 25 ball impacts. The trend in the flow stress was inversely proportional to the depth of the plate. As shown in Figure 6.27, the maximum flow stress was obtained at the impact surface at over 1.6 GPa and sharply decreased along the thickness of the plate. The flow stress decreased drastically as less energy was transferred at the depth of 0.7 mm so that the effect of SMAT is in significant beyond a depth of 0.7 mm.

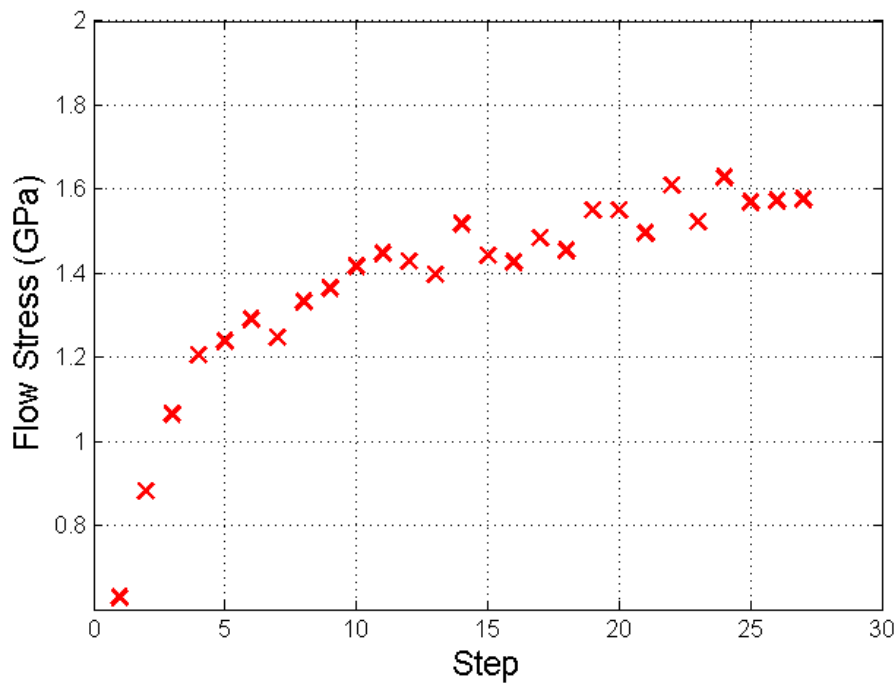


Figure 6.26 Average flow stress in each step for 10-min process

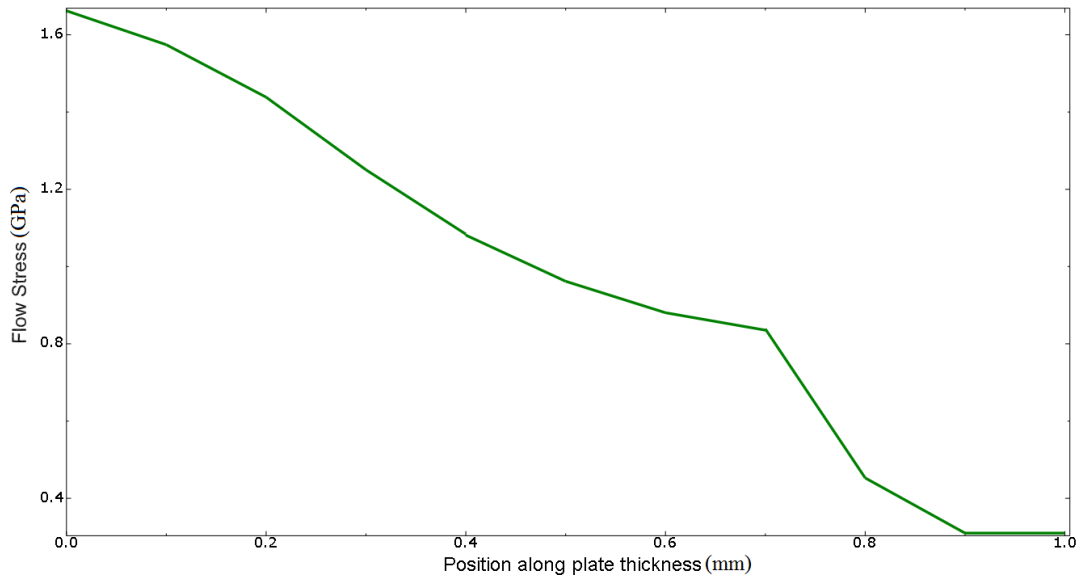


Figure 6.27 Average flow stress along the depth of plate for 10-min process

6.4.2.2 Case 2: Results and Discussion of Microstructure Evolution

One of the major contributions of the constitutive equation is to determine the effect of microstructure evolution. The average grain size is plotted in Figure 6.28,. The grain size was reduced up to 25 nm on average after 27 ball impacts. The contour plot shows that the minimum grain size was as fine as 20 nm at the impact location in Figure 6.29. The grain size was then gradually increased as the depth from the impact surface increased.

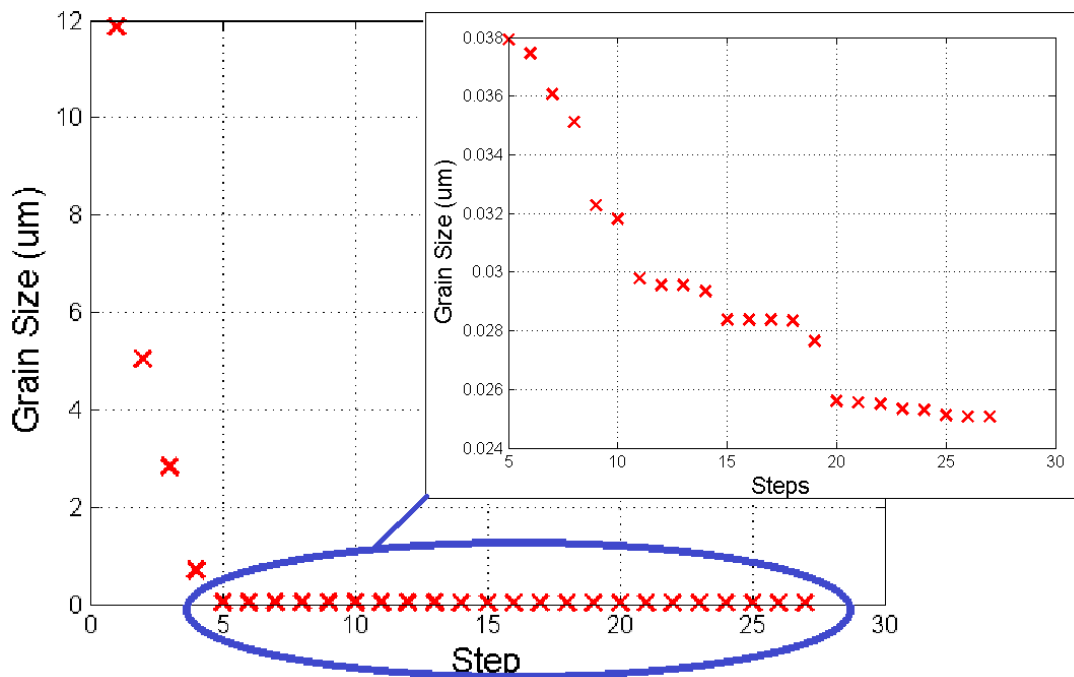


Figure 6.28 Grain size refinement at each impact for 10-min process

The contour plot of grain size in Figure 6.29 shows that the grain was refined at the impact location and spread out spherically. The grain size is 150 nm and then stopped refinement at a depth about 0.8 mm. In the region without plastic deformation, the grain size remains at 20 μm. Chen et al. (2011) observed that the processing duration was 15 min with 100 balls in their SMAT experiment. The average grain size at the top surface and the γ -austenite at a depth of 0.5 mm were 10 and 200 nm, respectively. Although the processing duration differed, the simulated grain size was close to the experimental observation.

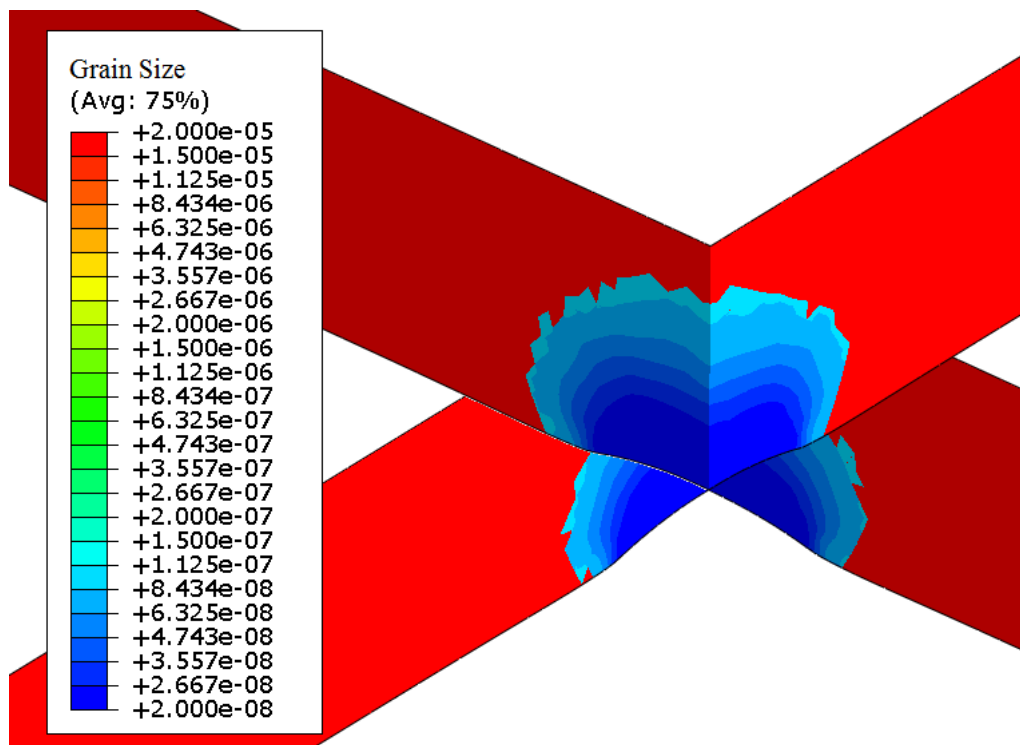


Figure 6.29 Contour plot of grain size after 27 ball impacts for 10-min process

In the simulation of the twin spacing, the average twin spacing greatly decreased in the first few steps in Figure 6.30. Further twin refinement occurred after five ball impacts up to 26 nm. The twin spacing decreased for further ball impacts and finally averaged 16 nm.

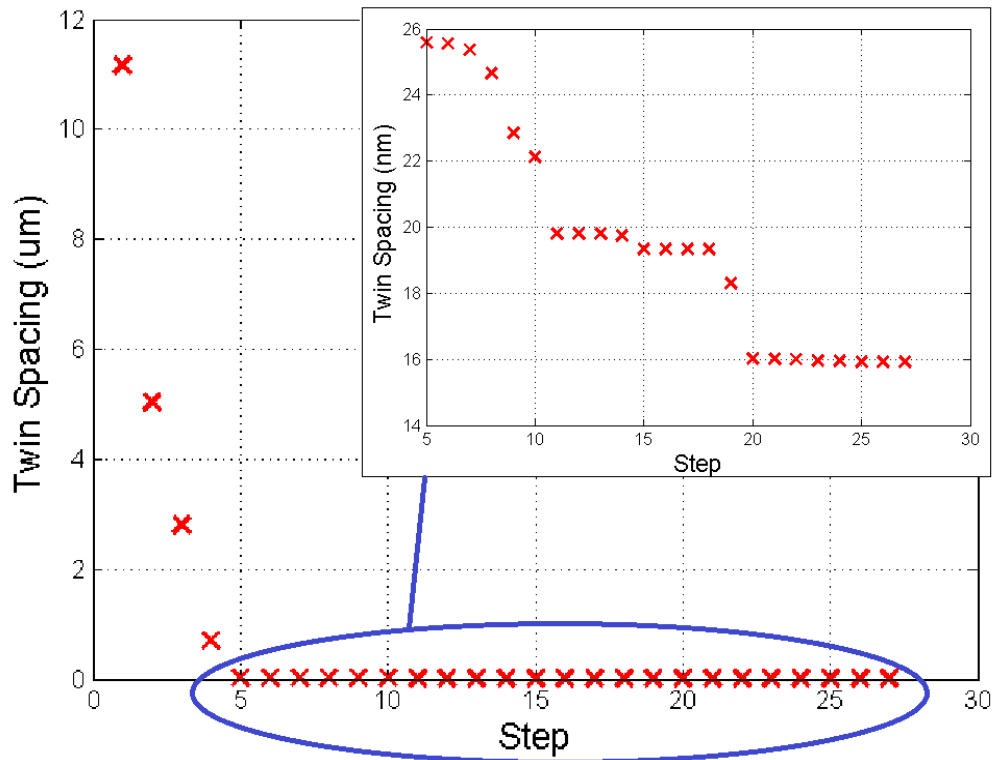


Figure 6.30 Twin spacing refinement in each impact for 10-min process

In Figure 6.31, the distribution of twin spacing is similar to that of grain size. When there was no plastic deformation, the twin refinement at 107 nm at a depth of around 0.8 mm. The minimum twin spacing was 12.5 nm at the impact surface. At a depth of 0.5 mm, the twin spacing is 58 nm. When compared with the experimental observations by Chen et al. (2011), the statistical measurements of twin thickness range from 2 to 50 nm, with an average of 20 nm at a depth of 0.5 mm. The simulated twin spacing is within the range of the experimental observation.

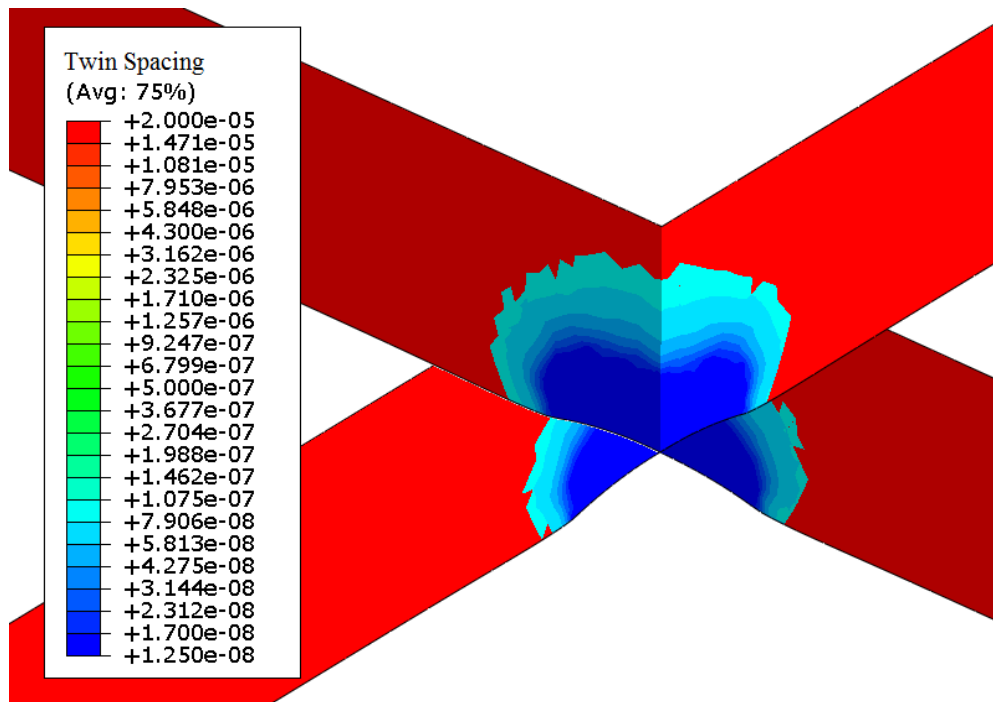


Figure 6.31 Contour plot of twin spacing in last step for 10-min process

6.4.3 Further Discussion of Cases 1 and 2

From the above results, it can be seen that longer processing duration can result in finer grain and higher stress. The longer processing duration implies more impacts in SMAT that will have more chance to achieve a higher ball velocity to the target plate.

In reviewing the ball impact velocity, the number of ball impacts in the 10-min process, with a velocity over 6 m/s, was greater than in the 3-min process. This will transmit more energy to the target plate and cause further plastic deformation. In the comparison of the equivalent plastic strain in Figure 6.32, the equivalent plastic strain

along the depth of the plate in case 2 is higher and more prolonged than in case 1. The equivalent plastic strain at the surface in case 2 is double that in case 1. The gradient of the equivalent plastic strain to the depth of the plate is steeper in case 2 and much gentler in case 1. This shows that after a longer processing duration, more impacts at high velocities can maintain a better equivalent plastic strain. It is difficult to cause plastic deformation in deeper layers. This, then, causes the sharp decrease in the gradient in both cases.

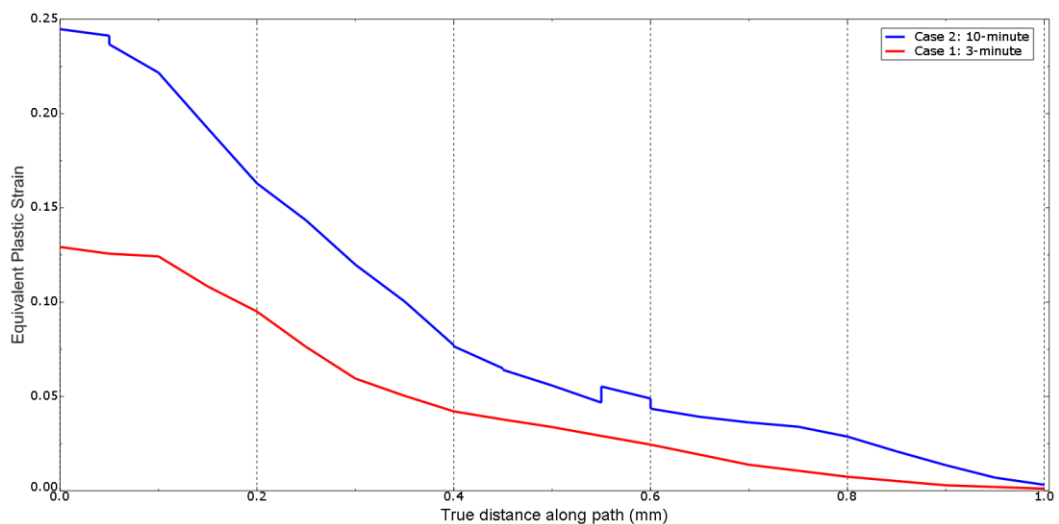


Figure 6.32 Comparison of equivalent plastic strain in cases 1 and 2 for 10-min process

Because the grain size and twin spacing are determined by the equivalent plastic strain, the refinements of the grain and twin spacing are initially serious. After several impacts, not many impacts will take place at the same location as in the 3-min process.

The refinement process is then terminated. However, more impacts occur during the 10-min process, thus the refinement process can carry on to produce more nano-grains in the same location. In case 1, the process may be too short to achieve a finer grain and high strength. The refinement process has not been finished but then stopped. In short, the refinement process occurs significantly and eventually saturated with the increase of the number of impacts.

These two cases illustrate that a longer processing duration can result in finer grains and twin spacing with high strength. In the study by Chan et al. (2010), a longer processing duration resulted in a higher yield stress, that is, 15-min > 10-min > 3-min, with 100 balls to conduct SMAT. The simulation result is consistent with their conclusion.

6.5 Summary

The finite-element simulation conducted implemented the new constitutive equation and the simulated impact positions and velocities of balls to predict mechanical properties after SMAT. With the same number of balls but different processing durations, the simulated yield stress was 1.1 GPa for the 3-min process and 1.23 GPa

for the 10-min process. In light of the experimental results, the results of 800 MPa for the 3-min process and 1 GPa for the 10-min process were overestimated.

In the simulation, the average grain size and twin spacing in the 3-min case were 54.8 and 46.3 nm, respectively, and in the 10-min process, the average grain size and twin spacing were about 150 and 58 nm, respectively, at a depth of 0.5 mm. In the 15-min experiment with 100 balls, the grain size was 200 nm and the twin spacing was between 2 and 50 nm. The simulation results are consistent with the experimental measurements. This finite-element model is valid for prediction of the results of the SMAT process with metal nano-twins.

It is clear that a longer processing duration will result in a higher yield stress and a finer grain size. However, the role of the processing duration in the enhancement of the mechanical properties after SMAT has not been shown experimentally. From the above simulation, it can be seen that a longer processing duration could result in a higher equivalent plastic strain that could further refine the grain and twin spacing with more high-energy impacts. It was also observed that the grain size, twin spacing, and stress began to refine and increase sharply within a 3-min process. A longer processing duration allows more impacts to occur until saturation. The average grain size and twin spacing are finer with the 10-min process than with the 3-min process,

where the refinement process has nearly reached saturation. A further increase in the processing duration will not enhance the mechanical properties and microstructure of the metal plate.

CHAPTER 7 - CONCLUSIONS AND RECOMMENDATIONS

7.1 Conclusions

This research firstly demonstrated a computational method to predict the ball impacts' positions and velocities in SMAT. The computational model of the dynamics of the balls was validated by experiments, in which the movements of the balls were captured by a high speed camera. The number of impacts calculated in the simulation agreed well with that measured in the experiment. Through this simulation model, the relationship between the impact conditions and processing parameters of SMAT were determined, which provides the quantitative information on the impacts of the balls.

After the development of a computational model for simulating the ball impacts in SMAT, on the basis of JC model, a new constitutive model was developed that considered both the microstructural evolution and macroscopic loading. The flow stress clearly related to, not only the strain, strain rate and homogenous temperature, but also the grain size and twin spacing in the refinement process. At the cut-off strain rate, 10^4 /s, the strain hardening process is led by the grain refinement alone, or together with the twin spacing diminishing. This new constitutive equation has also

been compared with the experimental result in the literature and the yield stress predicted is approximately 1.3 GPa, which compares well to the experimental value 1.2 GPa under the same conditions.

The whole idea of this research is to predict the mechanical properties following SMAT. The impact angle and velocity were firstly investigated to find the effect of a single ball. When the vertical component of the ball velocity is large, the influence on the target metal can be same as a normal impact with the same vertical velocity. To compensate for the low vertical velocity in the angular impact, a longer processing duration is recommended. To go a step further, the impact positions and velocities of the balls at a selected area were applied in the finite element model to simulate the residual stress level and the enhancement of mechanical properties in SMAT. The conventional JC model was implemented and the processing duration was assumed as 10 min with 100 balls in this simulation. The results generally agreed with those of the experiments with only slight underestimation (~15 %) of the yield stress. Another simulation was also conducted to investigate the importance of the impact velocity to the mechanical properties. The impact positions determined previously were still applied in the model where the impact velocities were all kept constant at 10 m/s. For this result, the average yield stress was still underestimated by 10 %. However, in most

of the cases, the ball impact velocity during the SMAT should not be as high as 10 m/s. The original JC model should be modified to handle the effects of the micro-structural evolution.

To improve the prediction in FEA, the new constitutive equation was implemented to the selected area in the model. The simulated yield stress was approximately 1.23 GPa, whereas the values found in the literature were about 1 GPa and 880 MPa for the engineering stress and true stress respectively. The overestimation was due to the assumption of perfect crystal forms in the simulation, whereas some defects may initially appear in the specimen in the experiment. Other than the yield stress, the grain size and twin spacing were also calculated as 150 and 58 nm respectively at a depth of 0.5 μm . In the experiment for 15-min with 100 balls of SMAT, the average grain size was 200 nm while the twin spacing was in between 2 and 50 nm at the same depth.

In conclusion, the simulation approach by the implementation of the new constitutive equation can predict the mechanical properties after the SMAT. The constitutive equation satisfactorily predicts the mechanical properties in metal plasticity, especially for twins induced metal. Recalling the objectives of this research:

1. to build a model and find out the relationship between the number of ball impacts

and processing duration of SMAT, and the number of balls;

2. to develop a constitutive model that represents the relationship between the flow stress and the grain size, twin spacing, strain, strain rate and temperature;
3. to develop a finite element model for simulating the SMAT process and estimating the grain size and twin spacing after the SMAT treatment.

All the objectives are achieved. Since there are many factors that affect the result after SMAT, the mechanical properties can then be estimated before conducting the experiments. Only the important sets of experiments need to be addressed in further investigations.

7.2 Recommendations and Further Work

7.2.1 Development of Large Scale Production

SMAT is a significant process in the production of nano-scaled metal. According to the experimental results found in the literature, SMAT was conducted in a small chamber where the height and diameter of the chamber are fixed at 15 and 70 mm respectively. The MATLAB simulations were conducted and compared with experiments. The frequency of ball-ball and ball-boundary collisions were

significantly affected by the chamber dimensions. However, in large scale production, the target metal plate will not be treated in a small chamber as it lowers the efficiency and effectiveness of the production. Due to the limitation of the experimentation study, further study and experiments on the SMAT need to be continued so that the dimensionless model can be developed for simulation and to determine the relationship between chamber dimension and the number of impacts. The computational model for the ball impacts can then be more comprehensive.

7.2.2 Modeling of Stacking Fault Energy and Martensite Transformation

In this research, stainless steel 304, a twins-induced metal, is the target metal. The FEA can calculate well the mechanical properties for twins-induced metal. However, for other non-twin metals, due to the absence of twin spacing, only the grain size and macrostructure factors are considered in this new constitutive equation. Further development of the constitutive equation should be continued together with other microstructure evolution parameters, such as stacking fault energy, martensite transformation etc. Taking into account the JC equation can expand the usage of the constitutive equation to these non-twins induced metals. Consideration of the

microstructure evolution and macrostructure change, thus, can be more comprehensive.

7.2.3 Development of General Equation on Various Impacting Factors

In the demonstration of the FEA, the stress distribution, grain size and twin spacing were all predicted. This gave a range of stress to the metal after SMAT before conducting further experiments and gave clues to the selection of different parameters for conducting the experiments. However, some parameters are not yet considered.

In the MATLAB simulation, factors, including number of balls, duration, ball velocity, height and radius of chamber, were investigated to determine the relationship to the number of impacts. However, some parameters have not been studied, such as the ball size, different ball material, etc. Further investigation on these parameters can then be used to develop a general formula to combine all parameters affecting the number of impacts in SMAT. A general formula can assist in the selection of all parameters before conducting experiments.

7.2.4 Application to other Several Plastic Deformation Process

Shot peening is another severe plastic deformation process that is similar to the SMAT.

In shot peening, the steel ball is flying at a high velocity and impacts on the target metal in a normal direction. The only difference is that the steel ball in shot peening need not be positioned in a chamber. The developed constitutive model and FEA, therefore, could be suitable for shot peening as well. The use of the constitutive equation is still applicable to the target metal with twins. Further validation and verification can be studied on the application of shot peening in the mechanical properties prediction.

BIBLIOGRAPHY

Aliofkhazraei, M. (2015). Nanocrystallization by Surface Mechanical Attrition. In H. Bagheri, M. Gheyhani, H. Masiha, M. Aliofkhazraei, & A. S. Rouhaghdam, *Handbook of Mechanical Nanostructuring* (Vol. II). Wiley-VCH Verlag GmbH & Co. KGaA.

Arifvianto, B., Suyitno, M., & Mahardika, M. (2012). Effects of surface mechanical attrition treatment (SMAT) on a rough surface of AISI 316L stainless steel. *Applied Surface Science*, 258, 4538 - 4543.

Azadmanjiri, J., Berndt, C. C., Kapoor, A., & Wen, C. (2015). Development of Surface Nano-Crystallization in Alloys by Surface Mechanical Attrition Treatment (SMAT). *Solid State and Materials Sciences*, 40, 164 - 181.

Azushima, A., Kopp, R., Korhonen, A., Yang, D., Micari, F., Lahoti, G., Yanagida, A. (2008). Severe Plastic Deformation (SPD) Processes for Metals. *CIRP Annals - Manufacturing Technology*, 57, 716 - 735.

Balusamy, T., Kumar, S., & Narayanan, T. S. (2010). Effect of surface nanocrystallization on the corrosion behaviour of AISI 309 stainless steel. *Corrosion Science*, 52, 3826 - 3834.

Balusamy, T., Sankara Narayanan, T., Ravichandran, K., Song Park, I., & Lee, M. (2013). Influence of surface mechanical attrition treatment (SMAT) on the corrosion behaviour of AISI 304 stainless steel. *Corrosion Science*, 74, 332 - 344.

Barnett, M. (2007a). Twinning and the ductility of magnesium alloys Part I: "Tension" twins. *Materials Science and Engineering A*, 464, 1 - 7.

Barnett, M. (2007b). Twinning and the ductility of magnesium alloys Part II: "Contraction" twins. *Materials Science and Engineering A*, 464, 8 - 16.

Bilde-Sørensen, J. B., & Schiøtz, J. (2003). Nanocrystals Get Twins. *Science*, 300, 1244 - 1245.

Bridgman, P. (1943). On Torsion Combined with Compression. *Journal of Applied Physics*, 14, 273.

Chan, H., Ruan, H., Chen, A., & Lu, J. (2010). Optimatization of the strain rate to achieve exceptional mechanical properties of 304 stainless steel using high speed ultrasonic surface mechanical attrition treatment. *Acta Materialia*, 58, 5086 - 5096.

Chemkhi, M., Retraint, D., Roos, A., Garnier, C., Waltz, L., Demangel, C., & Proust, G. (2013). The effectof surface mechanical attrition treatment on low temperature plasma nitriding of an austenitic stainless steel. *Surface and Coatings Technology*, 221, 191 - 195.

Chen, A., Li, D., Zhang, J., Song, H., & Lu, J. (2008). Make nanostructured metal exceptionally tough by introducing non-localized fracture behaviors. *Scripta Materialia*, 59, 579 - 582.

Chen, A., Ruan, H., Wang, J., Chan, H., Wang, Q., Li, Q., & Lu, J. (2011). The

influence of strain rate on the microstructure transition of 304 stainless steel. *Acta Materialia*, 59, 3697 - 3709.

Chen, A., Shi, S., Tian, H., Ruan, H., Li, X., Pan, D., & Lu, J. (2014). Effect of warm deformation on microstructure and mechanical properties of a layered and nanostructured 304 stainless steel. *Materials Science and Engineering A*, 595, 34 - 42.

Chen, A., Zhang, J., Lu, J., Lun, W., & Song, H. (2007). Necking propagated deformation behavior of layer-structured steel prepared by co-warm rolled surface nanocrystallized 304 stainless steel. *Materials Letters*, 61, 5191 - 5193.

Chen, M., Ma, E., Hemker, K., Sheng, H., Wang, Y., & Cheng, X. (2003). Deformation twinning in nanocrystalline aluminum. *Science*, 300, 1275 - 1277.

Chen, X., Lu, J., Lu, L., & Lu, K. (2005). Tensile properties of a nanocrystalline 316L austenitic stainless steel. *Scripta Materialia*, 52, 1039 - 1044.

Chen, W. (1994). *Constitutive equations for engineering materials* (Revised ed., Vol. 2). Amsterdam ; New York : Elsevier.

Cheong, B., Lin, J., & Ball, A. (2000). Modelling of the hardening characteristics for superplastic materials. *The Journal of Strain Analysis for Engineering Design*, 35, 149 - 157.

Cheong, B., Lin, J., & Ball, A. (2001). Modelling of hardening due to grain growth for a superplastic alloy. *Journal of Materials Processing Technology*, 119,

361 - 365.

Cheung, K., Silvanus, J., Shi, S., & Lu, J. (2011). Study on Mechanical Properties of 2024 Al Sheet Treated by SMAT. *Advanced Materials Research*, 410, 257-262.

Chokshi, A., Rosen, A., Karch, J., & Gleiter, H. (1989). On the validity of the hall-petch relationship in nanocrystalline materials. *Scripta Metallurgica*, 23(10), 1679 - 1983.

Chou, Y., & Pande, C. (1972). Effect of grain boundary dislocations on the slope of the Hall-Petch relation. *Metallurgical Transactions*, 3(2), 595 - 597.

Dao, M., Lu, L., Shen, Y., & Suresh, S. (2006). Strength, strain-rate sensitivity and ductility of copper with nanoscale twins. *Acta Materialia*, 54, 5421 - 5432.

Du, H., Wei, Y., Zhang, H., Lin, W., Hou, L., Liu, Z., & Liu, G. (2009). Effect of velocity of balls on the strain and stress of low carbon steel surface layer during SMAT. *International Journal of Modern Physics B*, 23(6&7), 1924 - 1930.

Ebrahimi, F., Bourne, G., Kelly, M., & Matthews, T. (1999). Mechanical properties of nanocrystalline nickel produced by electrodeposition. *Nanostructured Materials*, 11(3), 343 - 350.

Gallitelli, D., Reira, D., & Rouhaud, E. (2014). Comparison between conventional shot peening (SP) and surface mechanical attrition treatment (SMAT) on a Titanium alloy. *Advanced Materials Research*, 996, 964 - 968.

Gatey, A., Hosmani, S., Singh, R., & Suwas, S. (2013). Surface Engineering of

Stainless Steels: Role of Surface Mechanical Attrition Treatment (SMAT). *Advanced Materials Research*, 794, 238 - 247.

Grujicic, M., Pandurangan, B., Yen, C., & Cheeseman, B. (2012). Modifications in the AA5083 Johnson-Cook Material Model for Use in Friction Stir Welding Computational Analyses. *Journal of Materials Engineering and Performance*, 21, 2207 - 2217.

Greulich, F., & Murr, L., (1979). Effect of grain size, dislocation cell size and deformation twin spacing on the residual strengthening of shock-loaded nickel. *Materials Science and Engineering*, 39(1), 81 - 93.

Guo, J., Wang, K., & Lu, L. (2006). Tensile properties of Cu with deformation twins induced by SMAT. *Journal of Materials Science and Technology*, 22(6), 789 - 792.

Guo, X., Leung, A., Chen, A., Ruan, H., & Lu, J. (2010). Investigation of non-local cracking in layered stainless steel with nanostructured interface. *Scripta Materialia*, 63, 403 - 406.

Guo, X., Weng, G., & Soh, A. (2012). Ductility enhancement of layered stainless steel with nanograined interface layers. *Computational Materials Science*, 55, 350 - 355.

Hall, E. (1951). The deformation and ageing of mild steel: III Discussion of Results. *Proceedings of the Physical Society B*, 64(9), 747 - 753.

He, A., Xie, G., Zhang, H., & Wang, X. (2013). A Comparative Study on Johnson-Cook, Modified Johnson-Cook and Arrhenius-type Constitutive Models to Predict the High Temperature Flow Stress in 20CrMo Alloy Steel. *Materials and Design*, 52, 677 - 685.

Iwahashi, Y., Wang, J., Horita, Z., Nemoto, M., & Langdon, T. (1996). Principle of equal-channel angular pressing for the processing of ultra-fine grained materials. *Scripta Materialia*, 35(2), 143 - 146.

Jain, J., Zou, J., Sinclair, C., & Poole, W. (2011). Double tensile twinning in a Mg-8Al-0.5Zn alloy. *Journal of Microscopy*, 242(1), 26 - 36.

Johnson, G., & Cook, W. (1985). Fracture characteristics of three metals subjected to various strains, strain rates, temperatures and pressures. *Engineering Fractures Mechanics*, 21(1), 31 - 48.

Johnson, G., & Cook, W. (April, 1983). A constitutive model and data for metals subjected to large strains, high strain rates and high temperatures. *Proceedings: Seventh International Symposium on Ballistics* (pp. 19 - 21). The Hague, the Netherlands: Seventh International Symposium on Ballistics,.

Kashyap, B., & Tangri, K. (1990). On the Hall-Petch relationship in type 316L stainless steel at room temperature. *Scripta Metallurgica et Materialia*, 24(9), 1777 - 1782.

Kibey, S., Liu, J., Johnson, D., & Sehitoglu, H. (2007). Predicting twinning stress in fcc metals: Linking twin-energy pathways to twin nucleation. *Acta Materialia*,

55, 6843 - 6851.

Kim, D., & Kim, T. (2010). Mechanical behavior and microstructural evolution of commercially pure titanium in enhanced multi-pass equal channel angular pressing and cold extrusion. *Materials and Design*, 31, 54 - 60.

Kim, H., Estrin, Y., & Bush, M. (2000). Plastic deformation behaviour of fine-grained materials. *Acta materialia*, 48, 493 - 504.

Li, D.-z., Wei, Y.-h., Hou, L.-f., & Lin, W.-m. (2012). Microstructural Evolution of Surface Layer of TWIP Steel Deformed by Mechanical Attrition Treatment. *Journal of Iron and Steel Research*, 19(3), 38 - 46.

Li, J., & Soh, A. (2012). On elastic-viscoplastic modeling of nanotwinned metals based on coupled intra-twin and twin-boundary-mediated deformation mechanisms. *Philosophical Magazine Letters*, 92(12), 690 - 700.

Li, X., Wei, Y., Lu, L., Lu, K., & Gao, H. (2010). Dislocation nucleation governed softening and maximum strength in nano-twinned metals. *Nature*, 464, 877 - 880.

Li, W., Liu, P., Ma, F., & Rong, Y. (2009, June). Microstructural characterization of nanocrystalline nickel produced by surface mechanical attrition treatment. *Journal of Materials Science*, 44(11), 2925 - 2930.

Liang, R., & Khan, A. S. (1999). A critical review of experimental results and constitutive models for BCC and FCC metals over a wide range of strain rates and temperatures. *International Journal of Plasticity*, 15(9), 963 - 980.

Lu, J., Chan, H., Chen, A., & Kou, H. (2011). Mechanics of high strength and high ductility materials. *Procedia Engineering*, 10, pp. 2202 - 2207. Milano: Elsevier BV.

Lu, K., & Lu, J. (1999). Surface Nanocrystallization (SNC) of metallic materials- presentation of the concept behind a new approach. *Journal of Materials Science and Technology*, 15(3), 193 - 197.

Lu, K., & Lu, J. (2004). Nanostructured surface layer on metallic materials induced by surface mechanical attrition treatment. *Materials Science and Engineering A*, 375 - 377, 38 - 45.

Lu, L., Chen, X., Huang, X., & Lu, K. (2009). Revealing the Maximum Strength in Nanotwinned Copper. *Science*, 323, 607 - 610.

Lu, L., Shen, Y., Xhen, X., Qian, L., & Lu, K. (2004). Ultrahigh Strength and High Electrical Conductivity in Copper. *Science*, 304(5669), 422 - 426.

Luo, A.C.J., & R.P.S. Han. (1996). The Dynamics of a Bouncing Ball with a Sinusoidally Vibrating Table Revisited. *Nonlinear Dynamics*, 1996, 10, 1 - 18.

Majzoobi, G., Azizi, R., & Nia, A. A. (2005). A three-dimensional simulation of shot peening process using multiple shot impacts. *Journal of Materials Processing Technology*, 164-165, 1226 - 1234.

Marchenko, A., & Zhang, H., (2012). Effects of location of twin boundaries and grain size on plastic deformation of nanocrystalline copper. *Metallurgical and*

Materials Transactions A, 43(10), 3547 - 3555.

McFadden, S., Mishra, R., Valiev, R., Zhilyaev, A., & Mukherjee, A. (1999). Low-temperature superplasticity in nanostructured nickel and metal alloys. *Nature*, 398, 684 - 686.

Mecking, H., & Kocks, U. (1981). Kinetics of flow and strain-hardening. *Acta Metallurgica*, 29, 1865 - 1875.

Meo, M., & Vignjevic, R. (2003). Finite element analysis of residual stress induced by shot peening process. *Advances in Engineering Software*, 34, 569 - 575.

Meyers, M., Mishra, A., & Benson, D. (2006). Mechanical properties of nanocrystalline materials. *Progress in Materials Science*, 51, 427 - 556.

Michiuchi, M., Kokawa, H., Wang, Z., Sato, Y., & Sakai, K. (2006). Twin-induced grain boundary engineering for 316 austenitic stainless steel. *Acta Materialia*, 54, 5179 - 5184.

Nagasekhar, A., & Kim, H. (2008). Plastic deformation characteristics of cross-equal channel angular pressing. *Computational Materials Science*, 43, 1069 - 1073.

Neto, E. d., Peric, D., & Owen, D. (2008). *Computational Methods for Plasticity Theory and Applications*. United Kingdom: John Wiley & Sons Ltd.

Ni, S., Wang, Y., Liao, X., Langdon, T., & Zhu, Y. (2012). The effect of

dislocation density on the interactions between dislocations and twin boundaries in nanocrystalline materials. *Acta Materialia*, 60 (6-7), 3181 - 3189.

Pakiela, Z., Garbacz, H., Lewandowska, M., Druzycka-Wiecek, A., Suś-Ryszkowska, M., Zieliński, W., & Kurzydłowski, K. (2006). Structure and properties of nanomaterials produced by severe plastic deformation. *Nukleonika*. 51 (Suppl.1), pp. 19 - 25. Warsaw: Institute of Nuclear Chemistry and Technology.

Pande, C., Rath, B., & Imam, M., (2004). Effect of annealing twins on Hall-Petch relation in polycrystalline materials. *Materials Science and Engineering A*, 367, 171 - 175.

Petch, N. (1953). The cleavage strength of polycrystals. *Journal of the iron and steel institute*, 174, 25 - 28.

Phaniraj, M., Prasad, M., & Chokshi, A. (2007). Grain-size distribution effects in plastic flow and failure. *Materials Science and Engineering A*, 463(1-2), 231 - 237.

Pickens, J. (1981). Aluminium powder metallurgy technology for high-strength applications. *Journal of Materials Science*, 16(6), 1437 - 1457.

Prabhu, N. S., Joseyphus, J., Sankaranarayanan, T., Kumar, B. R., Mitra, A., & Panda, A. (2012). Residual Stress Analysis in Surface Mechanical Attrition Treated (SMAT) Iron and Steel Component Materials by Magnetic Barkhausen Emission Technique. *IEEE Transactions on Magnetics*, 48(12), 4713 - 4717.

Ruan, H., Chen, A., & Lu, J. (2010a). Characterization of plastically graded nanostructured material: Part I. The theories and the inverse algorithm of nanoindentation. *Mechanics of Materials*, 42, 559 - 569.

Ruan, H., Chen, A., Chan, H., & Lu, J. (2010b). Characterization of plastically graded nanostructured material: Part II. The experimental validation in surface nanostructured material. *Mechanics of Materials*, 42, 698 - 708.

Rule, W., & Jones, S. (1998). A Revised Form for the Johnson-Cook Strength Model. *International Journal of Impact Engineering*, 21(8), 609 - 624.

Sakaia, G., Katsuaki, N., Horita, Z., & Langdon, G. (2005). Developing high-pressure torsion for use with bulk samples. *Materials and Science Engineering A*, 406(1-2), 268 - 273.

Salehi, M., & Serajzadeh, S. (2012). Simulation of static recrystallization in non-isothermal annealing using a coupled cellular automata and finite element model. *Computational Materials Science*, 53, 145 - 152.

Schiøtz, J., Di Tolla, F. D., & Jacobsen, K. W. (1997). Softening of nanocrystalline metals at very small grain sizes. *Nature*, 391, 561-563.

Schino, A. D. & Kenny, J., (2003a). Grain refinement strengthening of a micro-crystalline high nitrogen austenitic stainless steel. *Materials Letters*, 57, 1830-1834.

Schino, A. D. & Kenny, J., (2003b). Grain size dependence of the fatigue behaviour of a ultrafine-grained AISI 304 stainless steel. *Materials Letters*,

57(21), 3182 - 3185.

Shen, X., Lian, J., Jiang, Z., & Jiang, Q. (2008). The optimal grain sized nanocrystalline ni with high strength and good ductility fabricated by a direct current electrodeposition. *Advanced Engineering Materials*, 10(6), 539 - 546.

Sheng, G. (2011). Investigation of Surface Self-Nanocrystallization in 0Cr18Ni9Ti Induced by Surface Mechanical Attrition Treatment. *ISRN Nanotechnology*, 2011(Article ID 583215), 1 - 9.

Sun, Y., Sun, J., Liu, M., & Chen, Q. (2007). Mechanical strength of carbon nanotube-nickel nanocomposites. *Nanotechnology*, 18(50), 505754.

Swygenhoven, H. V. (2002). Grain Boundaries and Dislocations. *Science*, 296, 66 - 67.

Takeuchi, S. (2001). The mechanism of the inverse Hall-Petch relation of nanocrystals. *Scripta Materialia*, 44(8-9), 1483 - 1487.

Tao, N., Wang, Z., Tong, W., Sui, M., Lu, J., & Lu, K. (2002). An investigation of surface nanocrystallization mechanism in Fe induced by surface mechanical attrition treatment. *Acta Materialia*, 50, 4603 - 4616.

Tao, N., Zhang, H., Lu, J., & Lu, K. (2003). Development of nanostructures in metallic materials with low stacking fault energies during surface mechanical attrition treatment (SMAT). *Materials Transactions*, 44(10), 1919 - 1925.

Taylor, G. (1934a). The mechanism of plastic deformation of crystals. Part I.

theoretical. *Proceedings of the Royal Society A*, 145, 363 - 387.

Taylor, G. (1934b). The mechanism of plastic deformation of crystals. Part II. comparison with observations. *Proceedings of the Royal Society A*, 145, 388 - 404.

Thamburaja, P., Pan, H., & Chau, F. (2009). The evolution of microstructure during twinning: Constitutive equations, finite-element simulations and experimental verification. *International Journal of Plasticity*, 25, 2141 - 2168.

Todaka, Y., Umemoto, M., & Tsuchiya, K. (2004). Comparison of nanocrystalline surface layer in steels formed by air blast and ultrasonic shot peening. *Materials Transactions*, 45(2), 376 - 379.

Tsai, W.Y., J.C. Huang, Y.J. Gao, Y.L. Chung, & G.R. Huang. (2015). Relationship between microstructure and properties for ultrasonic surface mechanical attrition treatment. *Scripta Materialia*, 103, 45 - 48.

Tsurekawa, S., Nakamichi, S., & Watanabe, T. (2006). Correlation of grain boundary connectivity with grain boundary character distribution in austenitic stainless steel. *Acta Materialia*, 54, 3617 - 3626.

Umbrello, D., M'Saoubi, R., & Outeiro, J. (2007). The influence of John-Cook material constants on finite element simulation of machining of AISI 316L. *International Journal of Machine Tools and Manufacture*, 47(3-4), 462 - 470.

Umemota, M., Todaka, Y., & Tsuchiya, K. (2003). Formation of nanocrystalline

structure in steels by air blast shot peening. *Materials Transactions*, 44(7), 1488 - 1493.

Valiev, R., & Langdon, T. (2006). Principles of equal-channel angular pressing as a processing tool for grain refinement. *Progress in Materials Science*, 51, 881 - 981.

Valiev, R., Estrin, Y., Horita, Z., Langdon, T., Zehetbauer, M., & Zhu, Y. (2006). Producing bulk ultrafine-grained materials by severe plastic deformation. *JOM*, 58(4), 33 - 39.

Valiev, R., Korznikov, A., & Mulyukov, R. (1993). Structure and properties of ultrafine-grained materials produced by severe plastic deformation. *Materials and Science Engineering A*, 168(2), 141 - 148.

Visser, W., Sun, Y., Gregory, O., Plume, G., Rousseau, C.-E., & Ghonem, H. (2011). Deformation characteristics of low carbon steel subjected to dynamic impact loading. *Materials Science and Engineering A*, 528, 7857 - 7866.

Wang, K., Shen, T., Quan, M., & Wei, W. (1993). Hall-Petch relationship in nanocrystalline titanium produced by ball-milling. *Journal of Materials Science Letters*, 12(23), 1818 - 1820.

Wang, K., Tao, N., Liu, G., Lu, J., & Lu, K. (2006). Plastic strain-induced grain refinement at the nanometer scale in copper. *Acta Materialia*, 54, 5281 - 5291.

Wang, X., & Shi, J. (2013). Validation of Johnson-Cool Plasticity and Damage

Model using Impact Experiment. *International Journal of Impact Engineering*, 60, 67 - 75.

Wang, Y., Chen, M., Zhou, F., & Ma, E. (2002, 10 31). High tensile ductility in a nanostructured metal. *Letters to Nature*, 419, 912 - 915.

Wei, Y. (2011). Scaling of maximum strength with grain size in nanotwinned fcc metals. *Physical Review B*, 83, 132104-1 - 4.

Wu, B., Zou, N., Tan, J.-s., Wang, J.-p., Pang, M., & Hu, D.-y. (2011). Numerical simulation on size effect of copper with nano-scale twins. *Transactions of Nonferrous Metals Society of China*, 21, 364 - 370.

Wu, H. (2005). *Continuum mechanics and plasticity*. Boca Raton: Chapman & Hall/CRC.

Wu, X., & Ma, E. (2006). Deformation twinning mechanisms in nanocrystalline Ni. *Applied Physics Letters*, 88, 061905 (3 pages).

Xiao, G., Tao, N., & Lu, K. (2008). Effects of strain, strain rate and temperature on deformation twinning in a Cu-Zn alloy. *Scripta Materialia*, 59, 975 - 978.

Xu, Q., & Liu, B. (2001). Modeling of As-Cast microstructure of Al alloy with a modified cellular automation method. *Materials Transactions*, 42(11), 2316 - 2321.

Yamakov, V., Wolf, D., Phillpot, S., & Gleiter, H. (2002). Deformation twinning in nanocrystalline Al by molecular-dynamics simulation. *Acta Materialia*, 50,

5005 - 5020.

Ye, X., Tse, Z. T., Tang, G., & Song, G. (2014). Effect of electroplastic rolling on deformability, mechanical property and microstructure evolution of Ti-6Al-4V alloy strip. *Materials Characterization*, 98, 147 - 161.

Ye, X., Tse, Z. T., Tang, G., Li, X., & Song, G. (2015). Effect of electropulsing treatment on microstructure and mechanical properties of cold-rolled pure titanium strips. *Journal of Materials Processing Technology*, 222, 27 - 32.

Yoon, S., Horita, Z., & Kim, H. (2008). Finite element analysis of plastic deformation behavior during high pressure torsion processing. *Journal of Materials Processing Technology*, 201, 32 - 36.

Yoshino, M., & Shirakashi, T. (1997). Flow-stress equation including effects of strain-rate and temperature history. *International Journal of Mechanical Sciences*, 39(12), 1345 - 1362.

Zhang, H., Hei, Z., Liu, G., Lu, J., & Lu, K. (2003). Formation of nanostructured surface layer on AISI 304 stainless steel by means of surface mechanical attrition treatment. *Acta Materialia*, 51, 1871 - 1881.

Zhang, S., Chen, H., & Lin, Q. (2004). Surface nanocrystallization of commercial pure titanium induced by SMAT and its properties. *Journal of Materials Science and Technology*, 20(6), 716 - 718.

Zhang, X. (2011). *Modeling of microstructure evolution induced by surface*

mechanical attrition treatment (SMAT) in AISI 316L stainless steel. Thesis, The Hong Kong Polytechnic University, Mechanical Engineering, Hong Kong.

Zhang, X., Lu, J., & Shi, S. (2011a). A computational study of plastic deformation in AISI 304 induced by surface mechanical attrition treatment. *Mechanics of Advanced Materials and Structures*, 18, 572 - 577.

Zhang, Z. Y., Yu, H. S., Chen, G., Yu, H., & Xu, C. Z. (2011b). Correlation between microstructure and tensile properties in powder metallurgy AZ91 alloys. *Materials Letter*, 65(17-18), 2686 - 2689.

Zhernakov, V., Budilov, I., Raab, G., Alexandrov, I., & Valiev, R. (2001). A numerical modelling and investigations of flow stress and grain refinement during equal-channel angular pressing. *Scripta Materialia*, 44, 1765 - 1769.

Zhilyaev, A. P., & Langdon, T. G. (2008). Using High-Pressure Torsion for Metal Processing: Fundamentals and Applications. *Progress in Materials Science*, 53(6), 893 - 979.

Zhilyaev, A., Nurislamova, G., Kim, B.-K., Baro', M., Szpunar, J., & Langdon, T. (2003). Experimental parameters influencing grain refinement and microstructural evolution during high-pressure torsion. *Acta Materialia*, 51, 753 - 765.

Zhu, K., Vassel, A., Brisset, F., Lu, K., & Lu, J. (2004). Nanostructure formation mechanism of α -titanium using SMAT. *Acta Materialia*, 52, 4101 - 4110.

Zhu, L., Ruan, H., Li, X., Dao, M., Gao, H., & Lu, J. (2011). Modeling grain size dependent optimal twin spacing for achieving ultimate high strength and related high ductility in nanotwinned metals. *Acta Materialia*, *59*, 5544 - 5557.

Zhu, L., Shi, S., Lu, K., & Lu, J. (2012). A statistical model for predicting the mechanical properties of nanostructured metals with bimodal grain size distribution. *Acta Materialia*, *60*, 5762 - 5772.